Methods for Seismic Wave Propagation on Local and Global Scales with Finite Differences

---

Methoden der seismischen Wellenausbreitung für lokale und globale Geometrien mit Finiten Differenzen

Inaugural-Dissertation
zur Erlangung des Doktorgrades
der Fakultät für Geowissenschaften
der Ludwig-Maximilians-Universität München

vorgelegt von
Gunnar Jahnke
am 17. September 2008

1. Berichterstatter: Prof. Dr. Heiner Igel
2. Berichterstatter: Prof. Dr. Michael Weber

Datum der mündlichen Prüfung: 19. März 2009

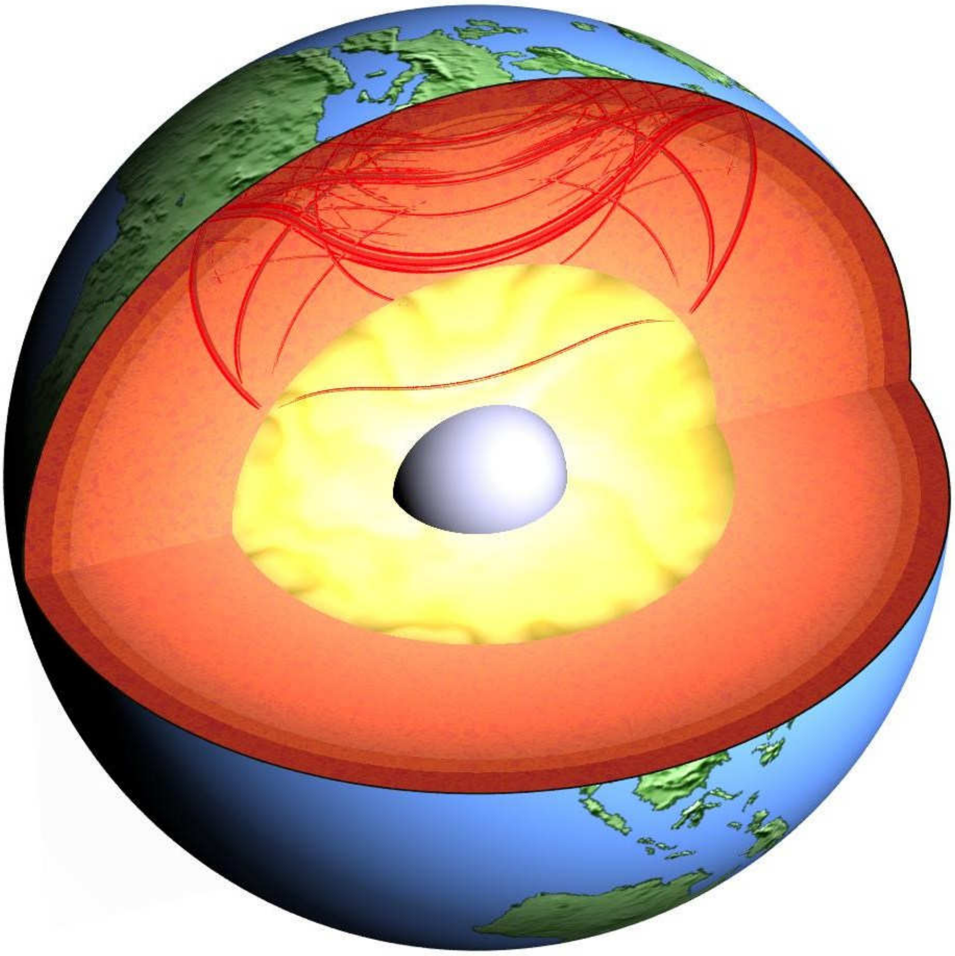

„Grau, theurer Freund, ist alle Theorie,
Und grün des Lebens goldner Baum.“

Johann Wolfgang von Goethe, Faust I

Zusammenfassung

Die vorliegende Arbeit behandelt zwei unterschiedliche Anwendungen aus dem Bereich der numerischen Seismologie: Das erste Thema umfasst die Entwicklung und Anwendung eines Programms zur Berechnung der *lokalen* Wellenausbreitung in seismischen Störungszonen (Fault Zones) mit spezieller Fokussierung auf *geführte Wellen* (Trapped Waves). Dieser Wellentyp wird an vielen Störungszonen beobachtet und aus seinen Eigenschaften können Informationen über die jeweilige Tiefenstruktur abgeleitet werden.

Das zweite Thema dieser Arbeit behandelt die Entwicklung und Anwendung zweier Verfahren zur Berechnung der *globalen* Wellenausbreitung, also der Ausbreitung seismischer Wellen durch die gesamte Erde einschließlich des äußeren und inneren Erdkerns. Die verwendeten Methoden ermöglichen es, kleinräumige Strukturen in großen Tiefen wie zum Beispiel die Streueigenschaften des Erdmantels oder die kleinskalige Geschwindigkeitsstruktur an der Kern-Mantelgrenze in knapp 2900 km Tiefe zu untersuchen.

Wellenausbreitung in seismischen Störungszonen

Seismische Störungszonen, wie zum Beispiel der San Andreas Fault in Kalifornien, zeigen auf beeindruckende Weise, wie die Gestalt der Erdoberfläche durch seismische Aktivität als Folge tektonischer Prozesse geprägt wird. Die genaue Kenntnis der *Tiefenstruktur* einer Störungszone hingegen bietet zusätzlich einen Einblick in die vergangene Seismizität, die die Struktur der jeweiligen Störung geprägt hat. Neben den tektonischen Eigenschaften einer Region lassen sich aus der Tiefenstruktur auch Voraussagen über Häufigkeit und zu erwartende Stärke zukünftiger Erdbeben ableiten. Da Erdbeben vorzugsweise in solchen Störungszonen auftreten, ist eine möglichst genaue Kenntnis der Geometrie einer Schwächezone wichtig, um Regionen mit erhöhtem Gefährdungspotenzial zu erkennen.

Für die Untersuchung der Tiefenstruktur einer Störungszone stehen in vielen Fällen ausschließlich Messungen von der Erdoberfläche zur Verfügung, etwa von seismischen Netzen, die in unmittelbarer Umgebung oder direkt auf einer Störung platziert wurden. Ereignet sich nun ein Erdbeben in einigen Kilometern Tiefe innerhalb der Störungszone, breitet sich ein Teil der angeregten seismischen Wellen durch die gesamte Störungszone bis zur Erdoberfläche aus, wo sie registriert werden. Die aufgezeichneten Signale werden somit entlang ihres gesamten Laufweges durch die Struktur der Störungszone beeinflusst, was die Ableitung der tiefenabhängigen Struktur aus den Messdaten erschwert.

Um trotzdem ein genaues seismisches Abbild einer Störungszone zu bekommen, analysiert man unterschiedliche Wellentypen im Seismogramm, wodurch ein Maximum an Strukturinformation abgeleitet werden kann. Einer dieser Wellentypen, der sich durch besondere Eigenschaften auszeichnet, ist die *geführte Welle* (Trapped Wave). Diese entsteht, wenn eine Störungszone einen ausgeprägten vertikal ausgedehnten Bereich drastisch reduzierter seismischer Ausbreitungsgeschwindigkeit (Low Velocity Layer) und nicht zu komplexer Geometrie besitzt, der als seismischer Wellenleiter wirkt. In einem solchen Wellenleiter kann sich eine geführte Welle ausbreiten, die als mit Abstand stärkstes Signal an der Erdoberfläche registriert wird, also deutlich stärkere Bodenbewegungen hervorruft als etwa die direkte Welle. Dieser Verstärkungseffekt hat unter anderem Konsequenzen für die Abschätzung der seismischen Gefährdung in der Nähe einer Störungszone, zum Beispiel wenn die Störungszone durch dicht besiedeltes Gebiet verläuft.
Geführte Wellen beinhalten aufgrund ihrer hohen Sensitivität bezüglich der Eigenschaften von Niedergeschwindigkeitszonen Strukturinformationen, die aus anderen Wellentypen nicht abgeleitet werden können. Daher leistet das Verständnis dieses Wellentyps einen wichtigen Beitrag für die Ableitung möglichst vollständiger Modelle von Störungszonen.

In *Kapitel 2* wird die Entwicklung und Anwendung des Programms *Fault3D* für die seismische Wellenausbreitung in realistischen dreidimensionale Modellen von Störungszonen mit vertikalem Wellenleiter beschrieben. Das Programm wurde für die Nutzung von Höchstleistungsrechnern mit verteilter Speicherarchitektur parallelisiert, um realistische Frequenzen und kleinräumige Strukturen abbilden zu können. Die korrekte Funktionsweise des Programms wurde durch Vergleich von berechneten numerischen Daten mit einer analytischen Lösung verifiziert.

Als Anwendung wurde eine Parameterstudie durchgeführt, in der systematisch der Einfluss von Geometrie und Geschwindigkeitsstruktur einer Störungszone mit vertikalem Wellenleiter auf das Seismogramm untersucht wurde. Des Weiteren wird gezeigt, unter welchen Umständen seismische Quellen, die außerhalb einer Störungszone liegen, geführte Wellen anregen können und welche Konsequenzen sich daraus für die Ableitung der Tiefenausdehnung einer Störungszone aus geführten Wellen ergeben. Die Ergebnisse dieser Studie helfen, den Einfluss der Tiefenstruktur von Störungszonen auf an der Oberfläche gemessene Signale geführter Wellen zu besser verstehen und haben bereits eine Reihe anderer Arbeiten zum Thema Störungszonen beeinflusst.

Ausbreitung von SH- und P-SV Wellen in Erdmantel und der ganzen Erde

Das allgemeine Verständnis der Struktur und Dynamik des tiefen Erdinneren basiert zu einem großen Teil auf den Ergebnissen der globalen Seismologie. Im Gegensatz zum ersten Teil dieser Arbeit haben diese Erkenntnisse keine unmittelbare Auswirkung auf unser tägliches Leben. Jedoch liefert die Kenntnis des inneren Aufbaus der Erde wichtige Erkenntnisse für die geophysikalische Grundlagenforschung bis hin zum Verständnis der Entstehungsgeschichte der Erde und unseres Planetensystems.

Die Modellierung der *globalen* seismischen Wellenausbreitung unterscheidet sich von der *lokalen* Modellierungen in zwei wesentlichen Punkten: (1) die wesentlich größere Ausdehnung globaler Modelle, welche die gesamte Erde oder zumindest große Teile des Erdinnern beinhalten, und (2) der Eigenschaft seismischer Wellen, sich im globalen Maßstab hauptsächlich in der Ebene auszubreiten, die durch den Großkreis zwischen Quelle und Empfänger aufgespannt wird. Beide Punkte legen nahe, zur Verringerung des Rechenaufwands eine Symmetriebedingung einzuführen. In dieser Arbeit wird durch die Formulierung von Wellengleichung und Modell in einem sphärisch-achsensymmetrischen Koordinatensystem der – im globalen Maßstab im Allgemeinen geringe – Anteil von Variationen der seismischen Parameter und von Wellenfeldanteilen orthogonal zur Großkreisebene vernachlässigt. Diese Beschränkung führt zu einer enormen Einsparung an Rechenressourcen, da das zu berechnende seismische Wellenfeld nur noch zwei Dimensionen aufspannt.
Eine Folge der Achsensymmetrie ist die Aufspaltung des seismischen Wellenfeldes in einen SH- und einen P-SV Anteil. Beide Wellenfeldanteile sind voneinander entkoppelt und breiten sich in unterschiedlichen Regionen des Erdinneren aus. Zur Berechnung des SH- und des P-SV Wellenfeldes wurden daher in dieser Arbeit zwei separate Programme *SHaxi* und *PSVaxi* entwickelt.

Kapitel 3 behandelt die Berechnung des globalen SH Wellenfeldes für achsensymmetrische Geometrien mit dem im Rahmen dieser Arbeit entwickelten Programm *SHaxi*. Das SH Wellenfeld besteht aus horizontal polarisierten Scherwellen, die sich in guter Näherung ausschließlich im Erdmantel, also zwischen Erdoberfläche und Kern-Mantelgrenze ausbreiten. Somit muss nur der Erdmantel als Modellraum abgebildet werden, was die Diskretisierung des Modells und die Implementierung der Wellengleichung deutlich vereinfacht. Um eine Anwendung auf modernen Parallelcomputern mit verteilter Speicherarchitektur zu ermöglichen, wurde der Modellraum durch vertikale Schnitte in gleichgroße Segmente geteilt, die von den einzelnen Elementen (Knoten) eines Parallelrechners getrennt bearbeitet werden können. Das Wellenfeld in den Randbereichen dieser Segmente muss dabei nach jedem Zeitschritt explizit zwischen benachbarten Knoten ausgetauscht werden, um die Ausbreitung durch das gesamte Modell zu ermöglichen.

Ein wesentlicher Aspekt des Kapitels ist die Verifikation des Verfahrens unter besonderer Berücksichtigung der implementierten Ringquelle. Durch einen Vergleich mit analytisch berechneten Seismogrammen werden die Eigenschaften der implementierten achsensymmetrischen Ringquelle diskutiert und es wird gezeigt, dass das Programm korrekte Seismogramme berechnet, die mit einer realistischen Double-Couple Quelle vergleichbar sind. Abschließend werden bisherige Anwendungen des Programms gezeigt: (1) die Modellierung von Streuung im gesamten Erdmantel und (2) die Untersuchung von kleinskaliger Topographie der D“ Schicht im untersten Erdmantel.

Kapitel 4 behandelt das Gegenstück des im vorherigen Kapitel behandelten Verfahrens: Das Programm *PSVaxi* zur Berechnung des globalen P-SV Wellenfeldes für achsensymmetrische Geometrien. Im Gegensatz zum SH Wellenfeld breitet sich das P-SV Wellenfeld nicht nur im Erdmantel sondern auch im äußeren und inneren Erdkern aus. Dies erforderte eine Erweiterung des Modellraums bis praktisch zum Erdmittelpunkt, die sich mit dem im SH Fall verwendeten gleichförmigen Gitter aufgrund von grundsätzlichen Stabilitätsproblemen des verwendeten Finite Differenzen Verfahrens nicht durchführen lässt.

Um diesen zusätzlichen Modellraum zu erschließen wurde eine Mehrgebietsmethode (*Multi-Domain Method*) implementiert. Diese füllt zusätzliche Tiefenbereiche mit neuen, jeweils gleichförmigen Gittern (*Domains*) aus, deren Gitterabstände an den jeweiligen Tiefenbereich angepasst sind, was für die notwendige Stabilität des Verfahrens sorgt. Zusätzlich zur tiefenabhängigen Aufteilung des Modellraumes in gleichförmige Gitter wurde eine Parallelisierung vorgenommen, um das Programm auf Parallelcomputern nutzen zu können. Dazu wurde der Modellraum durch horizontale Schnitte in einzelne Segmente zerlegt, die – analog zu den vertikalen Schnitten bei der *SHaxi* Parallelisierung – von den einzelnen Knoten eines Parallelrechners bearbeitet werden können. Die Kombination von Mehrgebietsmethode und Segmentierung führt zu einem recht aufwendigen Algorithmus, erlaubt jedoch die Berechnung des hochfrequenten globalen Wellenfeldes durch die ganze Erde auf Parallelrechnern mit vergleichsweise geringem Rechenaufwand.

Erste Anwendungen des *PSVaxi* Programms werden am Ende des Kapitels diskutiert: (1) eine exemplarische Modellierung der Wellenausbreitung in einer angenommenen D“ Schicht mit Topographie (2) eine Studie des Einflusses von Niedergeschwindigkeitszonen mit Topographie auf seismische Phasen, die durch den untersten Mantel und den äußeren Kern verlaufen und (3) eine Arbeit, die die Streueigenschaften des Mantels aus an der Kern-Mantelgrenze diffraktieren Wellen ableitet.

Danksagung

Zuerst möchte ich Prof. Heiner Igel für die Betreuung meiner Dissertation, sein stets offenes Ohr für Fragen und besonders für seine Geduld während der letzten Jahre, in denen sich die Fertigstellung meiner Arbeit durch meinen Gang nach Hannover verzögert hat, herzlich danken.

Während meiner Zeit im Institut für Geophysik in München durfte ich das Entstehen und Aufblühen von Heiners Arbeitsgruppe miterleben. Bei deren heutiger Größe und inhaltlicher Bandbreite ist es schwer vorstellbar, dass alles im Mai 1999 mit drei Personen, zwei PCs, einer Linux-CD und vielen offenen technischen und wissenschaftlichen Fragen begonnen hat.

Ich möchte außerdem der ersten Diplomandengeneration bestehend aus Martin Käser, Tarje Nissen-Meyer, Michael Ewald, Johannes Ripperger, Max Strasser und Falko Bethmann sowie natürlich auch Gilbert Brietzke und meiner Zimmerkollegin Melanie Reichhardt für den fachlichen und sozialen Austausch danken.

Toni Kraft und Christian Verard möchte ich für ihre Freundschaft, die vielen Gespräche, zünftige Abende im Steinheil und viele gemeinsame schöne Aktionen in unserer Freizeit danken, Ihr hab meine Zeit in München sehr bereichert.

Besonders im vergangenen Jahr habe ich viel Motivation aus der Zusammenarbeit mit Alain Cochard und Michael Thorne geschöpft. Alain hat durch beharrliches Hinterfragen scheinbar banaler Dinge wesentlich zum Verständnis des SHaxi Verfahrens beigetragen. Mike ist in mehrfacher Hinsicht ein außergewöhnlicher Wissenschaftler: Fachlich gehört er zu den wenigen Seismologen, die den Spagat zwischen numerischer und angewandter Seismologie exzellent meistern. Durch seine eindrucksvollen Anwendungen der in dieser Arbeit entwickelten SHaxi und PSVaxi Programme auf aktuelle Fragestellungen hat er deren Nutzen für die angewandte globale Seismologie bewiesen.

Danken möchte ich auch Prof. Michael Weber, der sich bereitwillig als Gutachter meiner Arbeit angeboten hat. Dies freut mich besonders, da ich dank Michaels Seismologievorlesungen in Göttingen erst auf dieses spannende Fach aufmerksam geworden bin. Später hat Michael es als Betreuer meiner Diplomarbeit geschafft, mir einen soliden Einblick in die Seismologie zu vermitteln, wovon ich seitdem sehr profitiert habe.

Meine Freundin Miriam hat mir währen der gesamten Doktorandenzeit tapfer zur Seite gestanden. Besonders im den letzten Jahr, in dem diese Arbeit immer wieder mit unserer Freizeitgestaltung konkurriert hat, war das nicht immer leicht. Ich freue mich mit Dir auf die kommende Zeit.

Liebe Eltern, Eure emotionale und finanzielle Unterstützung während meines Studiums und der Doktorandenzeit kann ich kaum genügend würdigen. Ich möchte Euch dafür danken, dass Ihr mir diesen Weg ermöglicht habt, was für mich keine Selbstverständlichkeit ist. Danke dass Ihr für mich da seid.

TABLE OF CONTENTS

LIST OF FIGURES .... **XII**

PREFACE........ **XV**

1 GENERAL INTRODUCTION **1**

2 WAVE PROPAGATION IN 3D FAULT ZONE STRUCTURES **5**

2.1 ABSTRACT 6
2.2 INTRODUCTION 7
2.3 NUMERICAL METHOD 8
2.4 VERIFICATION 8
2.5 RESULTS OF FAULT ZONE SIMULATIONS 10
2.5.1 Source location 10
2.5.2 Discontinuous faults 13
2.5.3 Varying fault width 16
2.5.4 Small scale inhomogeneities 18
2.5.5 Low-velocity layer and vertical velocity gradient 20
2.5.6 The Shallow-Fault model 21
2.5.7 Sources outside shallow faults 23
2.5.8 The Split-Fault models 25
2.6 DISCUSSION 28
2.6.1 Weak effects 28
2.6.2 Moderate effects 28
2.6.3 Strong effects 29
2.6.4 The Shallow-Fault model 30
2.6.5 The Split-fault model 31
2.6.6 Comparison with other studies 31
2.7 CONCLUSIONS 33

3 GLOBAL AXI-SYMMETRIC SH-WAVE PROPAGATION **35**

3.1 ABSTRACT 37
3.2 INTRODUCTION 37
3.3 THE AXI-SYMMETRIC FINITE-DIFFERENCE SCHEME 39
3.3.1 Formulation of the wave equation 39
3.3.2 Properties of the SH ring source 41
3.3.3 Boundary conditions 43
3.3.4 Parallelization 44
3.3.5 Computational costs 45
3.4 COMPARISON WITH THE ANALYTICAL SOLUTION 45
3.5 APPLICATION: SCATTERING FROM THE WHOLE MANTLE 49
3.5.1 Influence of axi-symmetry on the scattered wavefield 49
3.5.2 Simulations of whole mantle scattering 51
3.6 DISCUSSION AND CONCLUSIONS 54
3.7 STUDIES USING THE SHAXI CODE 55
3.7.1 Phase transitions in D” region beneath the central Pacific 55
3.7.2 Upper mantle discontinuities beneath the Hawaiian hotspot 55
3.8 LATERAL VARIATIONS OF THE D” REGION BENEATH THE COCOS PLATE 56

4 GLOBAL AXI-SYMMETRIC P-SV WAVE PROPAGATION **57**
4.1 INTRODUCTION 59
4.2 FORMULATION OF THE P-SV WAVE EQUATION 60
4.3 STAGGERED GRID SCHEME 61
4.4 MULTI DOMAIN DECOMPOSITION 64
4.5 PARALLELIZATION 65
4.6 OUTLOOK ON VERIFICATION 68
4.7 APPLICATIONS 68
4.7.1 D” layer with small scale topography 68
4.7.2 Ultra-low velocity zone with Topography in the D” region 71
4.7.3 Pdiff coda from whole mantle scattering 73
5 GENERAL DISCUSSION AND CONCLUSION **75**
5.1 TRAPPED WAVE MODELLING 77
5.1.1 Impact on recent studies 77
5.1.2 Trapped waves in shallow faults 77
5.1.3 Influence of 2D and 3D model variations 78
5.1.4 Model generation 79
5.1.5 Other studies 79
5.1.6 Outlook on trapped wave modelling 79
5.2 GLOBAL SH AND P-SV WAVE PROPAGATION 80
BIBLIOGRAPHY **83**
APPENDIX **93**
A.1 SOURCE CODE OVERVIEW 93
A.2 SUPPLEMENTARY CD ROM 93
A.2.1 Fault3D 94
A.2.1.1 Fault3D directory structure 94
A.2.1.2 Table of Contents of the Fault3D User Guide 95
A.2.2 SHaxi 96
A.2.2.1 Shaxi directory structure 96
A.2.2.2 Table of Contents of the SHaxi User Guide 96
A.2.3 PSVaxi 98
A.2.3.1 PSVaxi directory structure 98
A.2.3.2 Table of Contents of the PSVaxi User Guide 99

LIST OF FIGURES

Figure 2.1: *Model setup for the comparison with an analytical solution.* *9*
Figure 2.2: *Seismograms of the analytical and the numerical solution.* *10*
Figure 2.3: *Model of a basic fault with different source locations.* *11*
Figure 2.4: *Seismograms and maximum amplitude distributions for the models with different source locations.* *12*
Figure 2.5: *Selected seismograms, amplitude spectra and envelopes for the models with different source locations.* *13*
Figure 2.6: *Fault models with different amounts of lateral disruption.* *13*
Figure 2.7: *Seismograms and maximum amplitude distributions for the models with lateral disruption* *14*
Figure 2.8: *Selected seismograms, amplitude spectra and envelopes for the fault models with lateral disruption.* *14*
Figure 2.9: *Snapshots of wave propagation for a selected fault model with lateral disruption.* *15*
Figure 2.10: *Fault models with bottlenecks of different vertical extensions.* *16*
Figure 2.11: *Seismograms and maximum amplitude distributions for the bottleneck fault models* *16*
Figure 2.12: *Seismograms, amplitude spectra and envelopes for the bottleneck fault models* *17*
Figure 2.13: *Snapshots of wave propagation for a bottleneck fault model* *18*
Figure 2.14: *Model, seismograms and maximum amplitude distributions for a fault with small-scale inhomogeneities.* *19*
Figure 2.15: *Selected seismograms, amplitude spectra and envelopes for the fault with small-scale inhomogeneities and a homogeneous reference model..* *19*
Figure 2.16: *Models, seismograms and maximum amplitude distributions for two models with a fault widening towards the surface and a low velocity layer on top* *20*
Figure 2.17: *Selected seismograms, amplitude spectra and envelopes for the two models with a fault widening towards the surface and a low velocity layer on top* *21*
Figure 2.18: *Models of a shallow fault with laterally varying source positions* *22*
Figure 2.19: *Seismograms for the shallow fault models* *23*
Figure 2.20: *Source volumes for three different amplification factors for the shallow fault model.* *24*
Figure 2.21: *Model of a split-fault which is split at the surface but connected at depth* *25*
Figure 2.22: *Seismogram sections of multiple profiles across the split-fault with centered source position.* *26*

Figure 2.23*: Model, seismograms and maximum amplitude distributions for the split-fault and the laterally shifted source.* *27*

Figure 3.1: *Spherical coordinate system used for the the formulation of the wave equation in the SHaxi program* *39*

Figure 3.2: *The staggered grid scheme used in the SHaxi algorithm.* *40*

Figure 3.3: *Illustration of the ring source used in the SHaxi algorithm.* *41*

Figure 3.4: *Top-left part of the SHaxi grid with free surface and axi symmetry conditions* *43*

Figure 3.5: *Schematic illustration of the domain decomposition used for the parallelization of the SHaxi algorithm.* *44*

Figure 3.6: *Source-receiver setup, seismograms, maximum amplitude distribution and energy misfit of SHaxi versus numerical solution for the circular array.* *46*

Figure 3.7: *Source-receiver setup, seismograms, maximum amplitude distribution and energy misfit of SHaxi versus numerical solution for the linear array.* *48*

Figure 3.8: *Model of the mantle based on of PREM with additional random velocity variations.* *52*

Figure 3.9: *Snapshot of SH wave propagation for the perturbed PREM model compared with the original PREM model* *53*

Figure 3.10: *Seismograms for the perturbed PREM model and the original PREM model* *53*

Figure 4.1: *Cutout of the staggered grids used in the PSVaxi program including the boundary of two domains* *61*

Figure 4.2: *Cutout of the u_θ-grid together with the location of the interpolated u_θ-grid* *62*

Figure 4.3: *Cutout of the u_r-grid together with the interpolated u_r-grid* *63*

Figure 4.4: *Illustration of the multi domain decomposition scheme used in the PSVaxi program.* *64*

Figure 4.5: *Parallelization scheme of the PSVaxi program concerning the distribution of depth intervals on the individual nodes for all possible numbers of nodes.* *67*

Figure 4.6 *PSVaxi parallelization scheme for the case of four nodes.* *67*

Figure 4.7: *Models and ray paths of selected phases for two models based on PREM with an additional D" layer..* *69*

Figure 4.8: *Seismogram section with labelling of selected phases for the two D" models* *70*

Figure 4.9: *Cutout of the seismogram section for the two D" models around the Pdiff and pPdiff arrival.* *71*

Figure 4.10: *Seismogram comparison of synthetics calculated with the reflectivity method and PSVaxi for PREM with an additional low-velocity layer on top to the CMB*......................*72*

Figure 04.11*: Envelope stacks for five different scattering regimes compared with data*..*73*

Preface

This thesis is based on three publications which cover the development of methods for numerical calculation of the seismic wave field and their application to local and global problems:

Chapter 2 resembles closely the publication *Three-dimensional calculations of fault zone guided waves in various irregular structures* (Jahnke, Igel and Ben-Zion, 2002). In addition, it contains my contributions to the publication *Numerical simulation of fault zone trapped waves: accuracy and 3-D effects* (Igel, Jahnke and Ben-Zion, 2002).
These contributions are (1) the verification of the applied finite-difference modelling method, (2) simulations of two fault models: the shallow fault model and the y-shaped fault model, and (3) wave propagation snapshots for the bottleneck fault model and the laterally disrupted fault model. The related Figures were published in Igel, Jahnke, Ben-Zion (2002), whereas the corresponding discussion is original to this dissertation.
Section 2.5.7 “Sources outside shallow faults“ contains a Figure from the publication *Guided waves from sources outside faults: an indication for shallow fault zone structure?* (Fohrmann, Igel, Jahnke and Ben-Zion, 2004), the corresponding discussion is original to this dissertation.

Chapter 3 resembles the publication *Global SH-wave propagation using a parallel axi-symmetric spherical finite-difference scheme* (Jahnke, Thorne, Cochard and Igel, 2008). This publication originally contains a section with an application of the method to whole mantle scattering. This application is substantially a contribution of coauthor Michael S. Thorne and thus is not included here in original form. Instead, selected Figures of this section are shown and individually discussed in section 3.5.

Chapter 4 summarises the development and first applications of a code for P-SV wave propagation in global axi-symmetric geometries.

Chapter 1:

General Introduction

Our knowledge of the inner Earth's structure gained by multidisciplinary studies is to a large extent based on seismological results. The reason for this success of seismology in geosciences is caused by the large amount of information about the Earth's structure which is encoded in seismograms: Seismic waves travelling through the whole Earth carry information about its structural properties at depth towards the surface were they can be recorded. One big challenge in the field of seismology is therefore the development of methods for decoding the signatures of seismic data in order to reveal the originating structure at depth.

In the early days of theoretical seismology at the beginning of the previous century, only a fraction of the information contained in seismograms could be interpreted, such as travel time, polarity and amplitude of seismic signals. Due to the lack of appropriate analysing methods which existed for analogous recordings, the major part of the data had to be ignored. This restriction influenced the Earth models which could be revealed based on the available information. While the radial structure of the Earth could be derived with surprisingly high precision, such as the depth dependent seismic velocities, the extension of crust, outer and the inner core and of the mid mantle discontinuities, this was not the case for lateral variations in the Earth.

This changed with the development of digital recording techniques of seismograms and digital signal processing methods in the late 50s: The storage of seismic data as digital time series and the availability of early computers allowed the invention of completely new types of instruments and analysing methods. Broad band seismometers were developed which were not limited any more to predefined frequency ranges, since digital filtering for signal enhancement and noise removal could now be performed in a separate step as part of the data processing. Such instruments are sensitive for ground displacement over a very large frequency range, ranging from the Eigen-modes of the Earth in the order of hours up to frequencies of body waves of close earthquakes in the order of several tens of Hertz. Data processing methods such as stacking and correlation techniques enabled new ways for signal enhancement and, last not least, made seismic arrays possible with their radar-like detection capabilities.

Besides these new methods for data analysis, also first *inversion* techniques for performing the back-calculation of the originating seismic structure at depth from digital data, and also first *forward modelling* methods for the calculation of synthetic seismograms based on numerical wave propagation methods through simplified Earth models were developed. It turned out, that the complexity of calculations for Earth models which reflect realistic scale lengths and frequencies is immense and often well beyond existing computational resources, if no simplifications are applied to the calculation. Such simplifications are, for example, allowing for radial, layered or 2D model structure only, the restriction to lower frequencies than those visible in seismic data to be modelled, or investigation of smoothed models or models not incorporating small scale structure.

In recent times, thanks to the ongoing increase of computer power and of the efficiency of newly developed numerical methods, also the complexity of Earth models which can be calculated steadily increased. Therefore, forward modelling techniques became a growing importance for seismic data interpretation. At present, a variety of numerical methods for the calculation of synthetic seismograms exist, each being designed for a certain class of applications. Studies which derive actual Earth models from recorded seismic data largely benefit from these numerical methods as tools for more comprehensive data interpretation, for instance allowing to resolve complex seismic 3D structure and interpreting the results in context with tectonic and geodynamic issues.

The finite difference method used in this study is a classical approach for modelling the seismic wave field. Although newer, more sophisticated methods exist, finite difference methods can still compete due to their generality and flexibility and persistently prove to be valuable tools for solving actual problems, as will be shown.

In this thesis, the finite difference method was applied to three substantial different problems of seismic modelling: (1) local 3D wave propagation in fault zone structures, (2) global SH-wave propagation in the Earth's mantle, and (3) global P-SV wave propagation through the whole Earth. By developing particular finite difference schemes for each of the fields the individual structures of interest and their interaction with the seismic wave field can be calculated in an efficient way: For the fault zone modelling a 3D Cartesian approach was chosen, enabling to study arbitrary source mechanisms and structures in models of finite size where the curvature of the Earth can be neglected.

For the global SH and P-SV modelling algorithms a spherical axi-symmetric approach was used. This allows to calculate significantly higher model resolution and higher frequencies compared to full 3D methods by taking advantage of the fact that, for large propagation distances, the major portion of global seismic energy propagates in the great circle plane between source and receiver. All applied schemes were designed for the use on present high performance parallel computer systems which provide the required performance to cope with realistic frequencies and model resolutions.

A crucial point for a numerical algorithm is that it has been validated to provide correct seismograms. For the Cartesian 3D code and the axi-symmetric SH code this was shown by comparison with analytical solutions. For the P-SV code a full verification is still missing. However, a complete verification of the method is not beyond reach and the method has already been valuable for data analyses. Thus it is included in this thesis and the source is made available for further use.

Chapter 2:

Wave propagation in 3D fault zone structures

This chapter is mainly based on the publications *Three-dimensional calculations of fault zone guided waves in various irregular structures* (Jahnke, Igel and Ben-Zion, Geophys. J. Int. 2002) and *Numerical simulation of fault zone trapped waves: accuracy and 3-D effects* (Igel, Jahnke und Ben-Zion, Pure Appl. Geophys. 2002).
In addition, results are discussed from the publication *Guided Waves from Sources Outside Faults: An Indication for Shallow Fault Zone Structure?* (Fohrmann, Igel, Jahnke, Ben-Zion, Pure Appl. Geophys. 2004) about trapped wave generation by sources outside shallow faults.

2.1 Abstract

The detailed structure of a fault zone (FZ) plays an important role in problems related to fault mechanics, dynamic rupture, wave propagation and seismic hazard. FZs are thought to consist of a 10-100 m wide region of decreased seismic velocity. The small spatial scales involved make such structures difficult to image with ray-theoretical methods such as tomography.
However, when seismic sources are located at or near such low-velocity structure, energy is trapped inside the FZ, leading to dispersive wave trains that carry information on the FZ structure. These waves can travel many kilometres inside the fault before reaching the surface and are therefore strongly altered by its properties.
Candidate trapped waves have been observed above several active faults. Inversion algorithms exist that can model these observations in terms of planar fault zone structures. However, at present it is not clear how reliable these estimates are, as the effects of (even small) 3-D variations on trapped waves are not well understood.
The goal of this study is to distinguish 3-D structures that do and don't significantly affect FZ waves. To achieve this, we perform numerical calculations of various FZ geometries and analyze the waveforms, spectra and envelopes of the synthetic seismograms.
The main results are that (1) moderate changes of the shape of FZ or (2) small-scale heterogeneities or (3) depth-dependent properties do not strongly affect the observed FZ waves. In contrast, strong effects are to be expected from (4) breaks in the continuity of FZ structure (e.g. offsets), which may at some point allow imaging such features at depth.

2.2 Introduction

During recent years, data with evidence of FZ-guided head and trapped waves have been recorded in the vicinity of several earthquake faults. FZ head waves propagate along material interfaces in the FZ structure, while trapped waves propagate within low velocity FZ layers.

Detailed descriptions of theoretical properties of these waves in ideal 2D homogeneous seismic wave guides can be found in Ben-Zion and Aki (1990) and Ben-Zion (1998). Early observations of FZ guided waves were reported by Fukao et al. (1983), Leary et al. (1987), Li and Leary (1990), Ben-Zion and Malin (1991) and Ben-Zion et al. (1992). Li et al. (1994a,b; 1998) and Peng et al. (2000) analyzed candidate trapped waves generated by aftershocks along segments of the rupture zone of the 1992 M7.3 Landers, California, earthquake. Hough et al. (1994) obtained images of several small fault segments in the aftershock area of the 1992 M6.1 Joshua Tree earthquake based on modelling of candidate head waves. A summary of additional observations of FZ guided waves can be found in Ben-Zion and Sammis (2001).

The results from these works suggest that FZ structures at depth may have coherent layers of damaged rock, with low seismic velocity and high attenuation, which are tens to hundreds of m wide. A layer of damaged FZ rock with aligned cracks can also produce significant shear wave anisotropy. The boundary of the FZ layers may be abrupt or gradual with a smooth transition zone characterized by intermediate seismic properties.

To understand properties of seismic FZ waves and conceptual issues of representation theorem associated with sources at material interfaces, 2D analytical solutions for plane-layered structures were developed (Ben-Zion, 1989, 1990, 1999; Ben-Zion and Aki, 1990). These solutions are now employed efficiently as kernels in inversions of observed data using grid search and genetic algorithm techniques (Michael and Ben-Zion, 1998).

However, the 2D analytical solutions can not be used to study properties of guided waves in more realistic 3D structures. Calculations of wave propagation through irregular structures were performed using ray-theoretical techniques (Cormier and Spudich, 1984; Cormier and Beroza, 1987) and numerical methods (Leary et al., 1991, 1993; Igel et al., 1991, 1997; Li et al., 1994b; Li and Vidale, 1996; Huang et al., 1995).

Most of these investigations were carried out using either 2-D or acoustic approximations. A systematic examination of deviations from planar FZ structure, complete 3-D elastic effects, and a discussion on the implications for imaging schemes (e.g. Michael and Ben-Zion, 1998; Ben-Zion, 1998) is still missing.

The present paper aims at filling this gap by performing a parameter space study with various likely 3D FZ structures. Some of the geometries presented here can be seen as an extension to 2D modelling done by Li and Vidale (1996). The numerical method used in this study, a high-order finite-difference method, is introduced and comparisons of analytical and numerical solutions for strike-slip sources at material interfaces are presented. Also provided are several examples of 3D wave effects associated with heterogeneous FZ structures.

The main goals of our 3D parameter space study are to clarify (1) under what conditions the imaging of FZ structures can be done using analytical methods (planar FZ structures); and (2) which deviations from simple FZ structures may be detectable with 3-D methods. The focus is on FZ trapped waves. Prominent generation of FZ head waves requires an overall property contrast across the fault, whose structural causes are not considered in detail here.

The results indicate that structural discontinuities larger than the FZ width and source distance from the fault are significant perturbations that can destroy the generation and propagation efficiency of guided waves. On the other hand, vertical gradient of properties and heterogeneity with correlation length smaller than the FZ width would not inhibit guided wave propagation, nor be constrained by observations of guided waves. Various other cases fall on intermediate ground and have modest effects on the FZ waves.

2.3 Numerical Method

To solve the 3D elastic wave equation we use a fourth-order staggered-grid finite-difference (FD) method with an operator length of four grid points (Virieux 1984, 1986). The models used in this study are defined on a 3D Cartesian staggered grid with an overall mesh size on the order of 200^3 grid points. The grid spacing of our models is between 10 m and 30 m and the corresponding minimum wave lengths considered in our simulations are ~ 200 m to 600 m.

The source used in all simulations is a double couple with non-zero moment tensor components $M_{xy} = M_{yx} = M_0$. It is equivalent to horizontal slip on a vertical plane, which is strike-slip faulting, the most common source mechanism in transform fault zones. The source time function is the first derivative of a Gaussian function with a mean frequency ranging from 4.5 Hz to 13.5 Hz.

2.4 Verification

In order to assure that the used method is capable of calculating accurate seismograms for the fault zone models to be investigated a comparison with existing analytic solutions (Ben-Zion, 1990, 1999) for the case of two homogeneous elastic halfspaces and a source situated directly at the interface of the two media was performed. This setup has two important features in common with the fault zone generated trapped waves: (1) the source is located directly at a sharp material interface, and (2) waves which were generated by the material interface have a strong influence on the seismograms.

It is not evident that the used staggered-grid method is capable of coping with such models. The spatial staggering of the different seismic parameters causes both the effective source location and the position of any material interface to be diffuse. Due to the high sensibility of the seismograms on slight variations of such setups one may expect that the method fails and that significant differences between analytical and numerical seismograms. However, it will be shown that the algorithm provides accurate seismograms for sources positioned directly at sharp discontinuities.

The geometry of the chosen model of two half spaces with an analytical solution is shown in Figure 2.1. A point source is situated 1000 m below and 1000 m horizontally apart from a linear receiver array. The model does not contain a free surface; no analytical solution exists for such a case. Thus, both the source and the receiver array are embedded in the media. Each halfspace has elastic seismic properties which are given in terms of the Lamé Parameters and the density. The source is a double-couple source located directly at the material interface with the only non-zero moment tensor component $M_{xy} = M_{yx} = M_0$. The used displacement source time function is a ramp of 0.1 s duration.

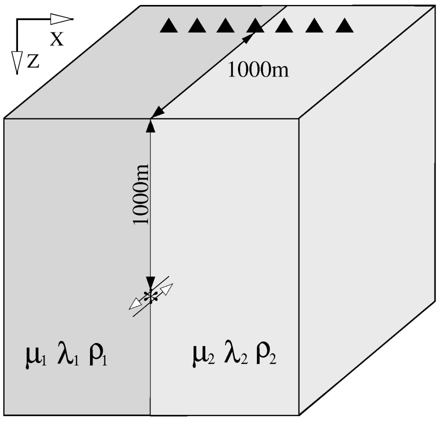

***Figure 2.1**: Model setup for the comparison with analytical solutions. The model consists of two half spaces with different seismic properties. The source is situated at the boundary of the half spaces and head waves are generated in addition to the direct P and S wave. The source is a strike-slip double-couple and the source time function is a ramp of 0.1 s duration.*

In Figure 2.2 the three components the resulting analytical and numerical seismograms for the receiver situated directly at the material discontinuity are shown. The unfiltered finite-difference seismograms (left) already show the wave form features of the analytical solution, for example the signature of the source time function which is a ramp of 0.1 s duration for both P and S waves are clearly visible.

The high-frequency oscillations for the unfiltered numerical traces are a typical finite-difference effect which vanishes after appropriate filtering. On the right of the figure low-pass filtered traces of the analytical and the numerical solution with a dominant frequency of 6.7 Hz are shown. The root-mean square error of the numerical solution is less than 3%, which shows that the numerical method is capable of calculating accurate seismograms.

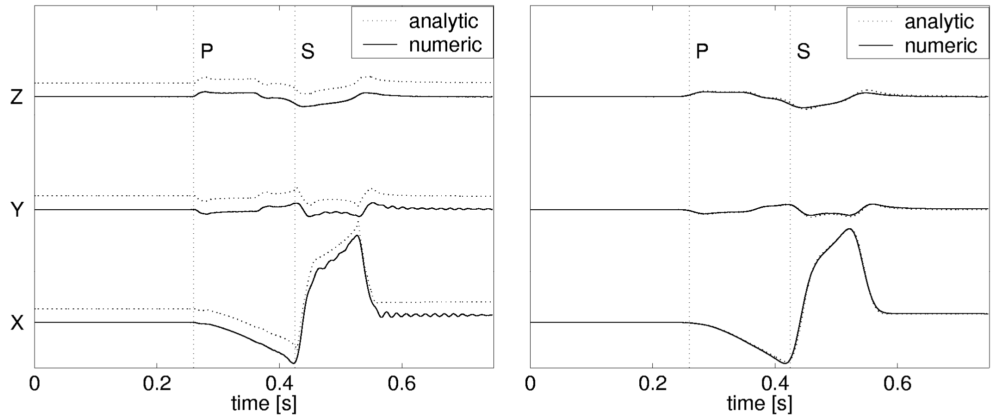

Figure 2.2 *Left: Unfiltered seismograms of the analytical (dotted) and the numerical (solid) solution for the receiver located at the boundary of the two half spaces. For a better view the analytical solution is shifted slightly upwards. The theoretical arrival times of P and S waves are marked by vertical lines. Right: Filtered traces of the analytical (dotted) and the numerical (solid) solution with a dominant frequency of 6.7 Hz.*

2.5 Results of fault zone simulations

In the following we investigate the effects of fault zones with 3D geometry and property distribution on the generation of fault zone guided waves. The sequence of 3D models has been chosen in order to incrementally develop intuition on 3D effects.

We begin by introducing (1) a basic 2D FZ structure as a reference solution. Then we investigate (2) the effects of source location with respect to the FZ; (3) discontinuous FZ structures; (4) moderate changes to the shape of the FZ boundaries (narrowing and widening); (5) small-scale heterogeneities inside the FZ; (6) low-velocity surface layer at the top and depth-dependent velocities in the host rock; (7) a shallow FZ model; and finally (8) FZ structures discontinuous at the surface but connected at depth. Unless otherwise mentioned, all models have the properties listed in Table 2.1. All seismogram plots show the y-component of velocity.

2.5.1 Source location

The first model examines the sensitivity of the wave field to the hypocenter location with respect to a basic 2D coherent FZ structure. This model-type can be calculated analytically. However, as we refer to these models when discussing 3D perturbations, it is an important starting point. The model consists of a homogeneous FZ layer in a half space. For a complete description of the model geometry see Figure 2.3 and Table 2.1. For this setup, trapped wave energy is largest for the source located directly at the FZ boundary (Figure 2.4).

	vp [km/s]	vs[km/s]	rho [g/cm^3]
Host rock	5.00	3.50	2.35
FZ models			
Gradient model: (at surface)	3.50	2.17	1.64
Inhom. Model:	3.50-5.00	2.17-3.10	1.6-2.35
Other models:	3.50	2.17	1.64
Source type :	Double couple, M_{xy}=M_{yx}=M_0		
Source time function:	Ricker wavelet		

Models:	Gradient model	Inhom. Model	Other models
Mean frequency:	4.5 Hz	13.5 Hz	4.5 Hz
Source depth:	12500 m	2000 m	6000 m
FZ width:	210 m	200 m	270 m
Grid spacing:	30 m	10 m	30 m
Receiver spacing:	100 m	20 m	100 m
Array aperture:	2000 m	560 m	2000 m

Table 2.1: *General properties of the simulations done in this study. The host rock of all models except the gradient model has identical seismic properties. In the gradient model, the seismic FZ parameters are lowered by 25% with respect to the surrounding halfspace at the same depth. The contrast of the model with small scale inhomogeneities varies from 0% to 30%. The contrast of all remaining models is 30%.*

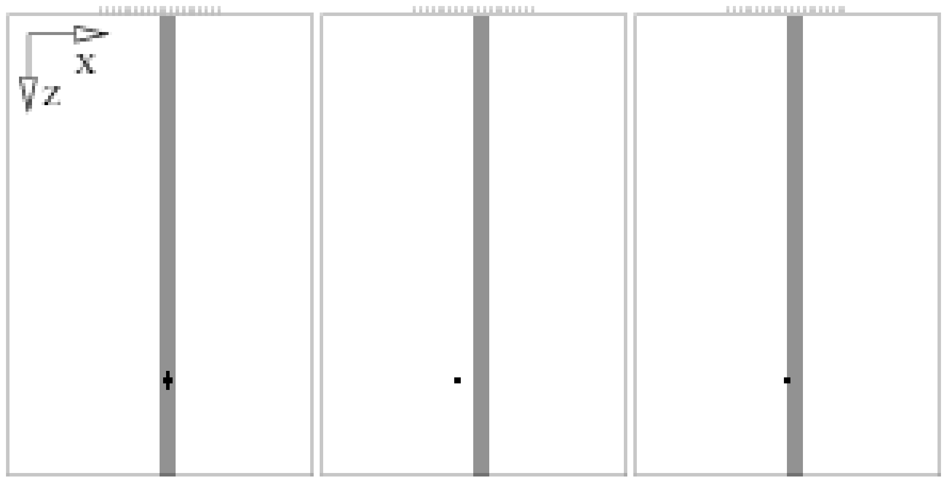

Figure 2.3: *Model of a basic fault and different source locations. Left: source position outside the fault, middle: source at the FZ boundary, right: source centered in the fault. The source depth is 6 km. The width of the FZ is 270 m. The receivers are positioned along a line crossing the fault, marked by vertical dashes on top. The size of the model is 5 km in x and y direction and 7.5 km in z direction.*

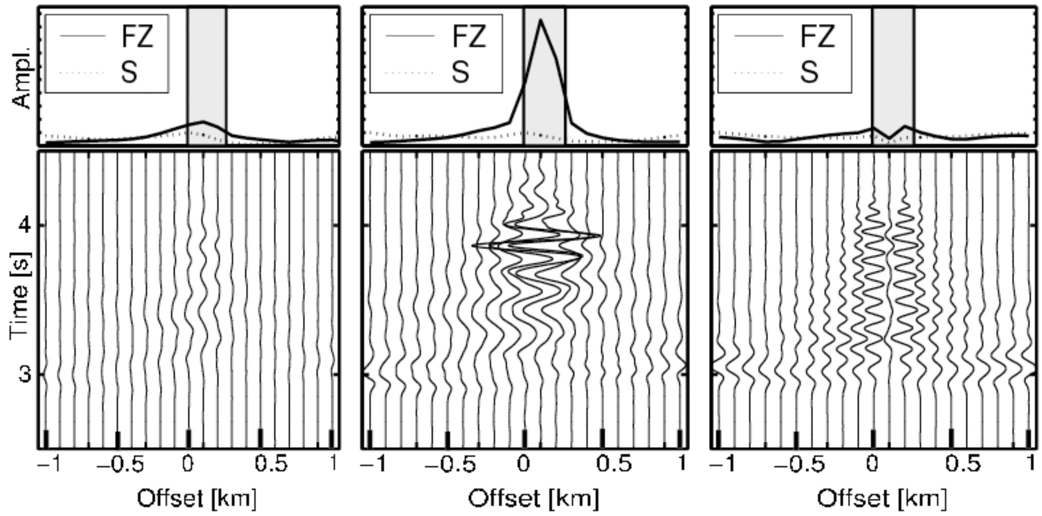

Figure 2.4: *Seismograms for the models shown in Figure 2.3. The y-component of velocity seismograms are drawn to scale. Left: source outside the fault, middle: source at the FZ boundary, right: source centered in the fault. The grey rectangle denotes the stations above the fault. The maximum amplitude of each trace for both the direct (dotted line, marked with S) and the trapped wave (solid line, marked with FZ) are displayed on top of the seismograms.*

The maximum amplitude of the trapped waves is 10 times larger than the maximum direct S-wave amplitude. For a source centered in the FZ, weaker trapped waves occur due to destructive interference for reasons of symmetry. The source located one FZ width outside the structure leads to an amplitude distribution along the receiver line which is similar to the amplitude distribution of the direct S-wave. In this case the amplitudes of the FZ waves are at most twice the S-wave amplitude.

Strong effects can also be seen in the wave forms, amplitude spectra and the envelopes of the traces (Figure 2.5): for the source at the FZ boundary the FZ wave energy is most concentrated, the wave trains for the other models arrive more dispersed.

The frequency spectrum for the source located outside the fault contains lower frequencies compared to the source at the FZ boundary, whereas the spectrum of the centered source is shifted to higher frequencies. A more extensive examination of the effect of source location with respect to the fault is given by Ben-Zion (1998). Unless stated otherwise, in the following 3D simulations the source location will be at the FZ boundary.

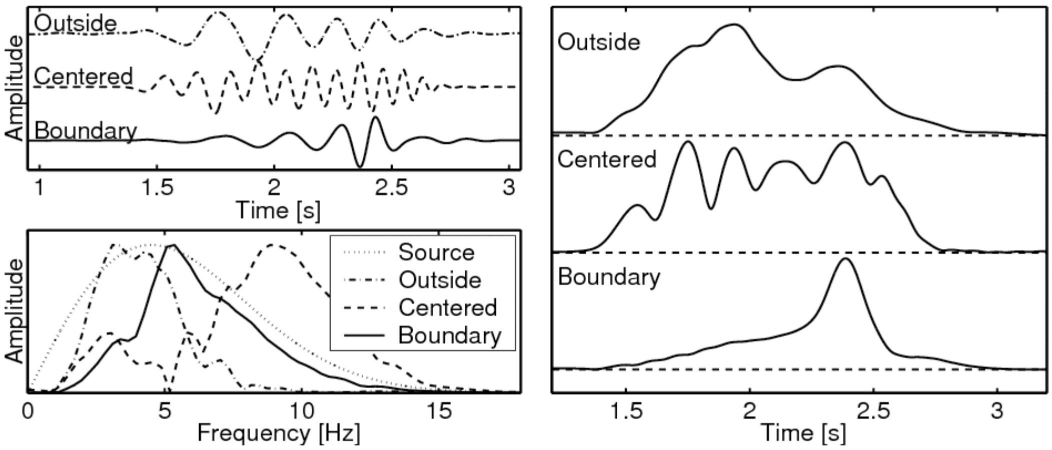

Figure 2.5 *Left column: trace with the maximum FZ wave amplitude (top) and the corresponding amplitude spectrum for the models with different source locations (bottom). Solid: source at FZ boundary, dashed: source centered in the fault, dash-dotted: source outside. Dotted: spectrum of the source time function. Right column: corresponding envelopes of the traces. All graphs shown here are normalized. The relative amplitudes of the waves in the different cases are shown in Figure 2.4.*

2.5.2 Discontinuous faults

To answer the question how continuous a fault must be to guide FZ waves, three models with different amounts of structural offset are examined (see Figure 2.6).

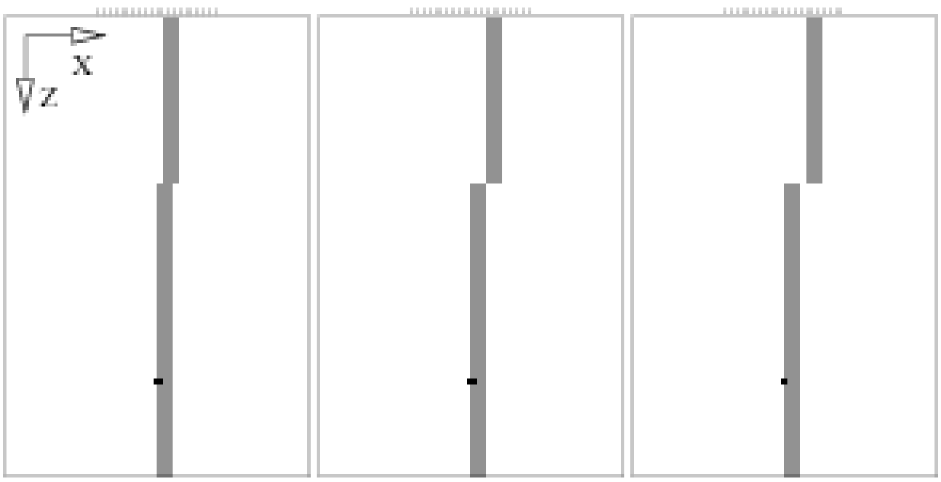

Figure 2.6: *Fault models with different amounts of lateral disruption. Left: shift of 1/2 FZ width, middle: shift of 1 FZ width, right: shift of 3/2 FZ width. The size of the model corresponds to the models in Figure 2.3.*

The model properties are described in Table 2.1. While the model setup is such that the waves travel vertically across the FZ discontinuity, this geometry may also be relevant for faults with a horizontal offset, a commonly observed feature at the surface. In case of a lateral shift of 1/2 FZ width, the amplitude distribution is similar to that of the basic fault model (Figure 2.7) and a strong distinct peak in the amplitude distribution of the FZ waves appears.

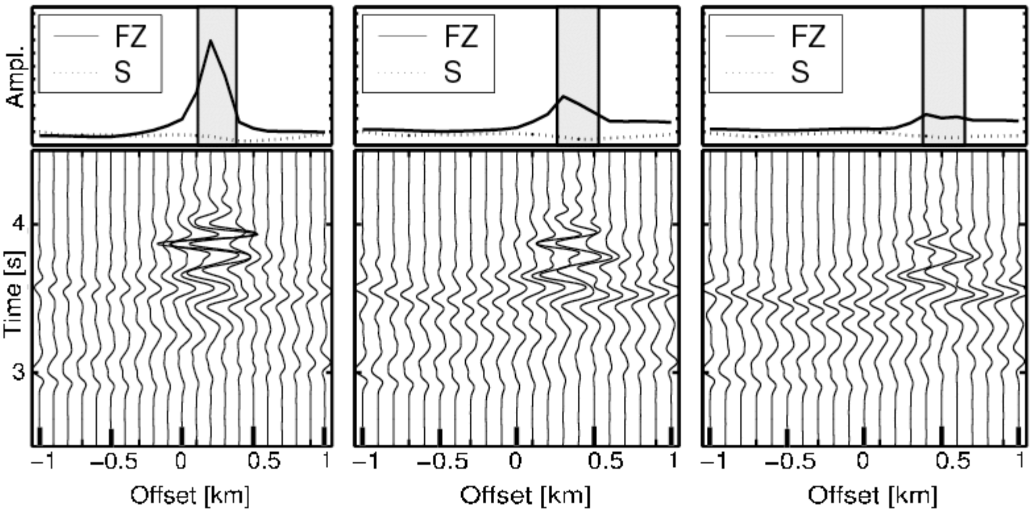

Figure 2.7: *Seismograms and maximum amplitudes for the models shown in Figure 2.6. Left: shift of ½ FZ width, middle: shift of 1 FZ width, right: shift of 3/2 FZ width.*

The spatial width of this peak is almost the same as in the basic fault model, but the amplitude is lowered from a 10-fold amplification for the basic model to an 8-fold increase. For a shift of one FZ width, the maximum FZ wave amplitude increase is 4-fold. In addition, the width of the region with higher amplitudes is broadened compared to the previous models to 3/2 FZ width.

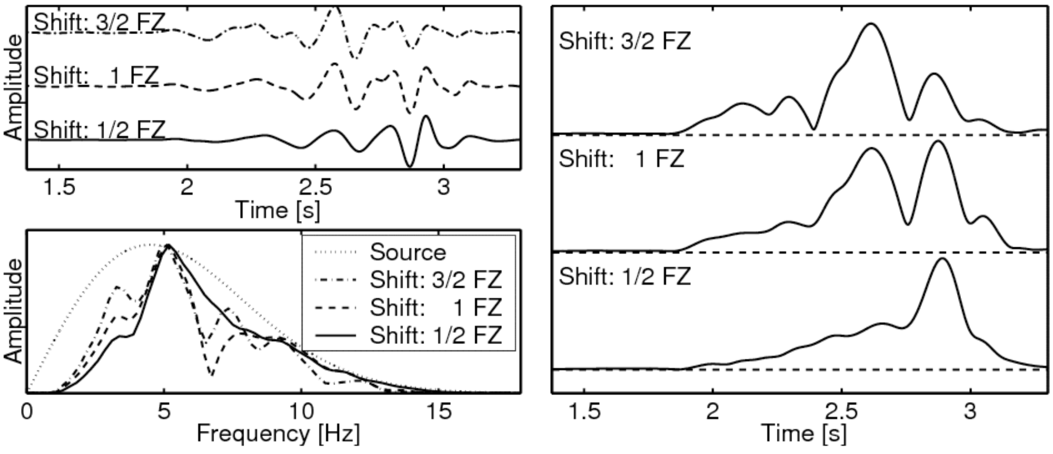

Figure 2.8: *Seismograms, amplitude spectra and envelopes for the fault models with lateral disruption. Solid: shift of 1/2 FZ widths, dashed: shift of 1 FZ width, dash-dotted: shift of 3/2 FZ widths. Dotted: spectrum of the source time function.*

The model with a lateral shift of 3/2 FZ width shows only a 2.5-fold FZ wave amplitude increase and the region with higher amplitudes extends over 2.5 FZ widths. The wave forms and traces in Figure 2.8 show longer FZ wave trains with lower amplitudes for increasing fault offsets, indicative of increasing diffusion of the FZ waves for increasing structural discontinuity. The spectra of all models are similar.

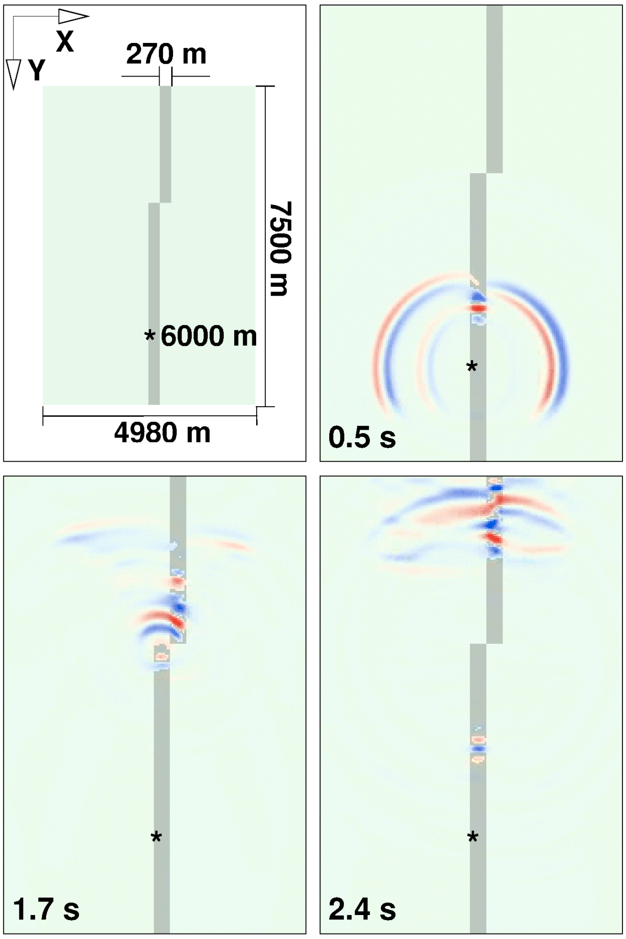

Figure 2.9: Snapshots of wave propagation in the fault model with lateral disruption. Red and blue colors denote positive and negative velocities of y component (SH type motion), respectively. The source at the fault zone boundary is indicated by a star. After 0.5 s the trapped wave train already emerged in the continuous lower section of the fault. Additionally, body S waves propagate in the host rock. After 1.7 s the trapped wave train passes the discontinuity and looses energy by radiation into the left quarterspace. After 2.4 s the weakened but still prominent fault zone wave train is about to reach the surface.

2.5.3 Varying fault width

The next set of models is used to investigate the influence of varying FZ shape on the trapped waves. Figure 2.10 shows 3 structures with a narrow part of variable size in the vertical direction, acting as a bottleneck for the propagating FZ waves.

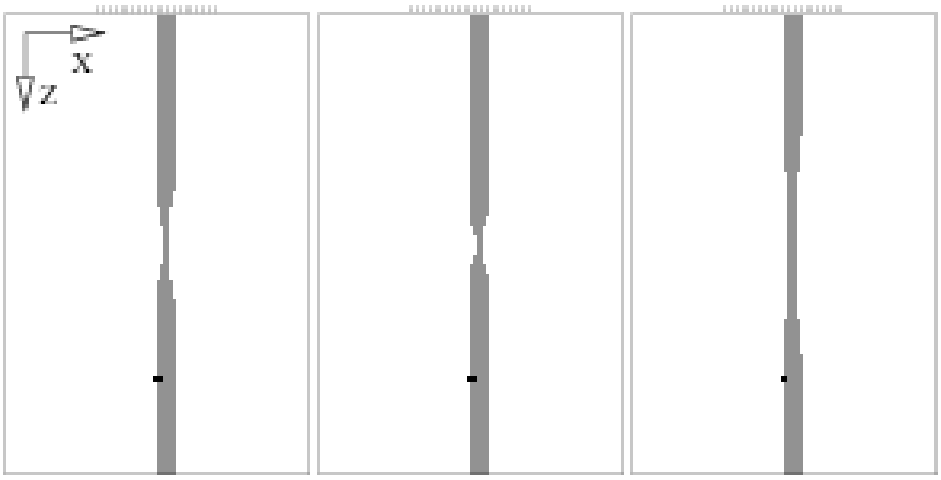

Figure 2.10: *Models of a bottleneck with different extension in depth. Left: extension of 13 1/3 FZ widths, middle: extension of 6 2/3 FZ widths, right: extension of 3 1/3 FZ widths. The size of the model corresponds to the models in Figure 2.3.*

Additional model properties are described in Table 2.1. In all models the narrowest part is 40% of the maximum FZ width while the depth extension of the bottleneck varies from model A (largest extension) to model C (smallest extension). The maximum FZ width is 270 m.

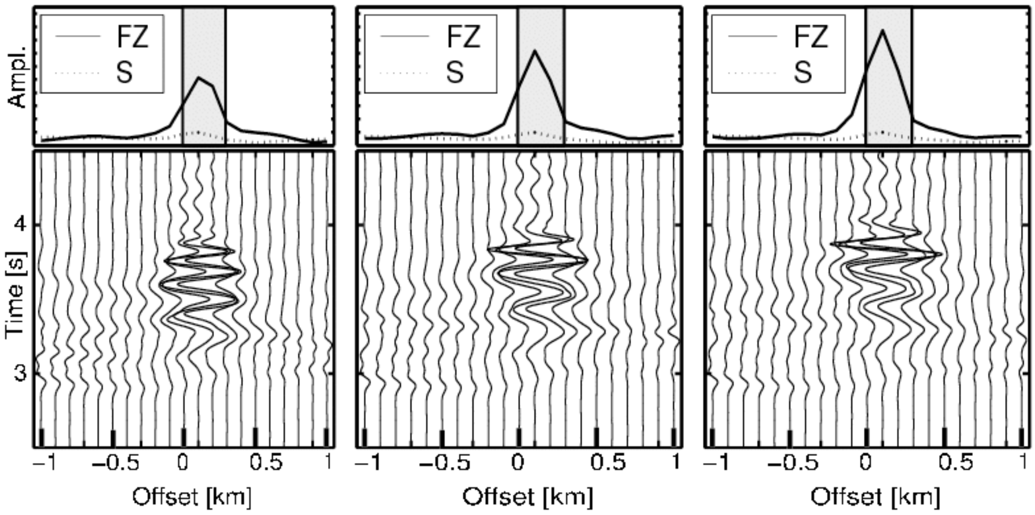

Figure 2.11: *Seismograms for the models shown in Figure 2.10. Left: extension of 13 1/3 FZ widths, middle: extension of 6 2/3 FZ widths, right: extension of 3 1/3 FZ widths.*

In model A, with a large and narrow bottleneck extension of 13 1/3 FZ widths, the guided waves in the seismograms arrive slightly earlier than the FZ waves of the basic fault model (Figure 2.11). For the first arrivals, this difference is only 0.1 s but the effect is somewhat larger for the strongest amplitude phases and the FZ waves for the bottleneck model arrive 0.2-0.25 seconds prior to the waves in the basic case. The maximum amplitude of the guided waves is 5-fold and thus half as big as in the basic FZ case.

For model B with a bottleneck extension of 6 2/3 FZ widths the trend of an earlier arriving FZ wave compared to the basic case still persists. Due to the smaller extension of the narrow FZ part these effects are reduced to 0.1 seconds. The maximum FZ-amplitude is 7 times the S-wave amplitude.

Model C with the smallest bottleneck extension of 3 1/3 FZ width shows almost the same travel times and maximum FZ amplitudes as the basic fault model. The spectra of the three models show no significant difference, but the envelopes show an increasing length of the wave train for larger bottleneck extensions (Figure 2.12)

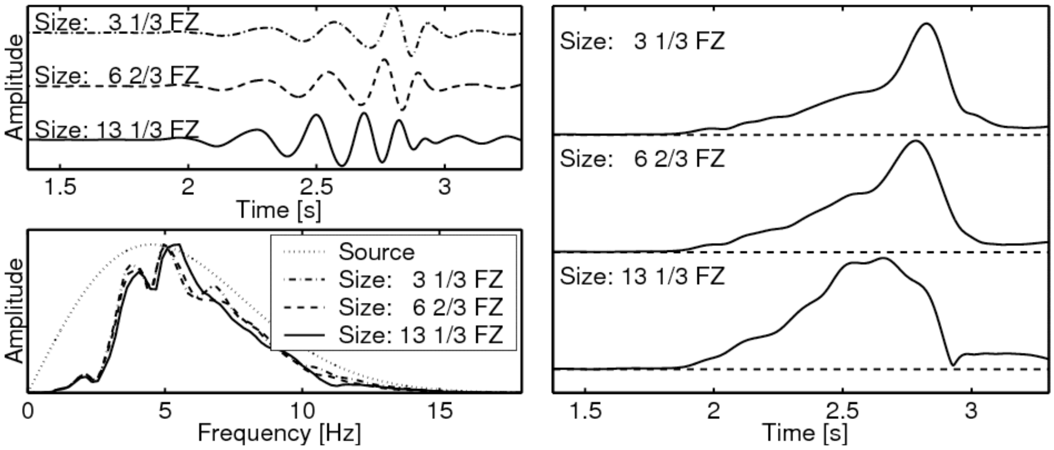

Figure 2.12: *Seismograms, amplitude spectra and envelopes for the fault models with a bottleneck with different extension in depth. Solid: extension of 13 1/3 FZ widths, dashed: 6 2/3 FZ widths, dash-dotted: 3 1/3 FZ widths. Dotted: spectrum of the source time function.*

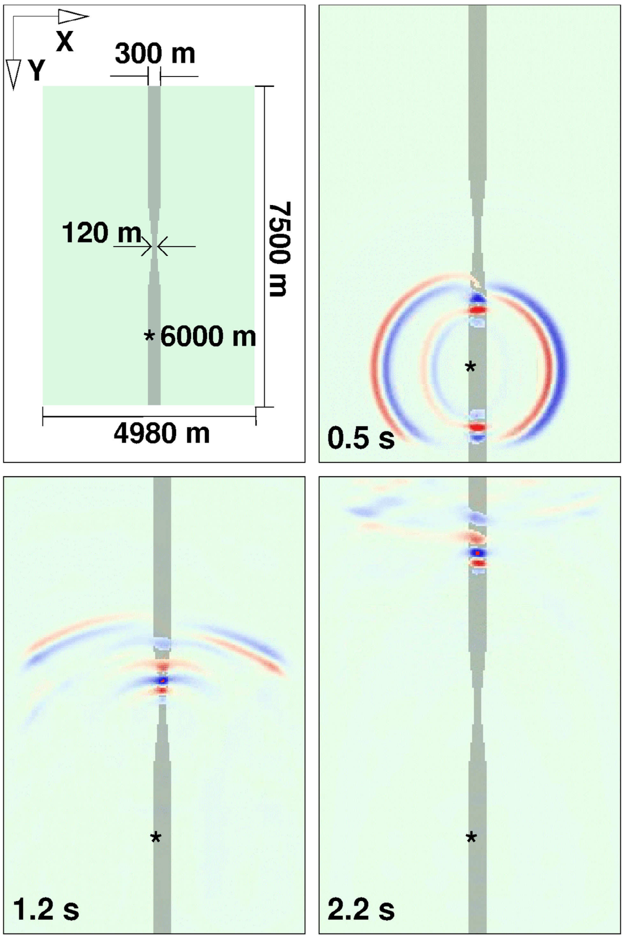

***Figure 2.13** shows the setup and snapshots of wave propagation for a bottleneck model with bottleneck extension of 6 2/3 FZ widths. Color coded is the y component of velocity. The source is indicated by a star. After 0.5 s the wave field is about to enter the thin part of the fault. After 1.2 s the trapped wave train travels through the thin section and radiates an increased amount of energy into the surrounding quarter spaces. After 2.2 s the slightly diminished but still prominent fault zone wave train is about to reach the surface.*

2.5.4 Small scale inhomogeneities

In the models described so far, the material properties in the FZ were constant. In this section we investigate the influence of varying seismic properties at small scales in a simple FZ geometry. To be able to add small 3D perturbations to a thin FZ layer, a denser grid with a spacing of 10 m and a FZ width of 200 m were chosen. Since the smaller grid spacing allows the computation of higher frequencies, the mean frequency source time function set to 13.5 Hz. The model properties are described in Table 2.1.

The inhomogeneous FZ region was produced by calculating a random number for each grid point belonging to the FZ and applying a spatial sliding window averaging 5x5x5 neighbouring points. This process yields a heterogeneous model with a correlation length of ~30 m. The smoothed random values were mapped to the desired velocity distribution in the fault. Figure 2.14 (left) shows a cross section through the FZ with a grey scale proportional to the seismic velocity.

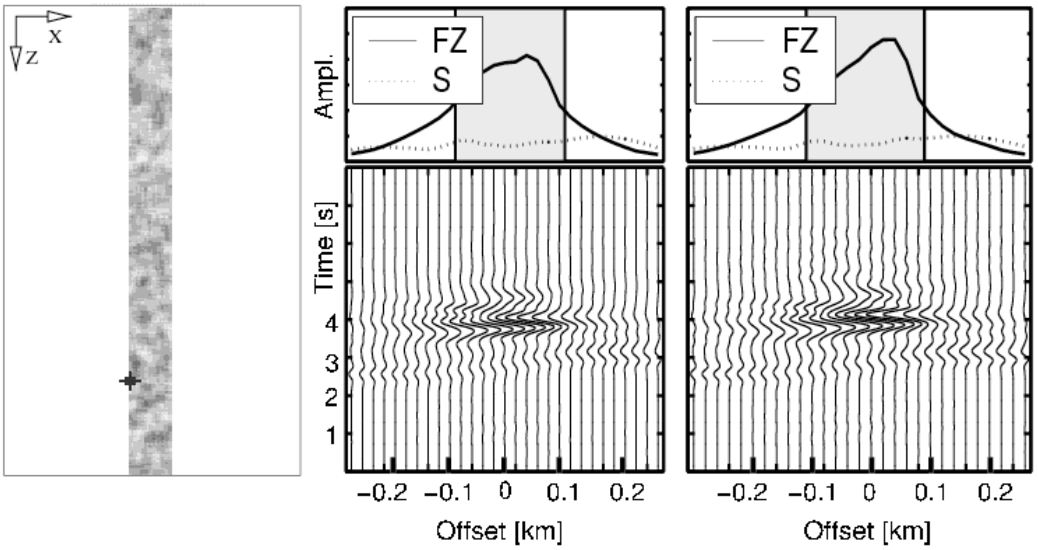

Figure 2.14: *Left: model with small-scale inhomogeneities, the FZ properties vary from -30% to 0% with respect to the surrounding quarterspaces. Middle: seismograms for a reference model with uniform seismic FZ properties which corresponds to the average of the inhomogeneous model. Right: seismograms for a fault with small-scale inhomogeneities.*

The properties inside the FZ vary from -30% (dark shade) to 0% (bright shade) with respect to the surrounding half space. Figure 2.14 (center and right) gives seismograms of this model and of a corresponding FZ structure with seismic properties given by to the average properties of the inhomogeneous model.

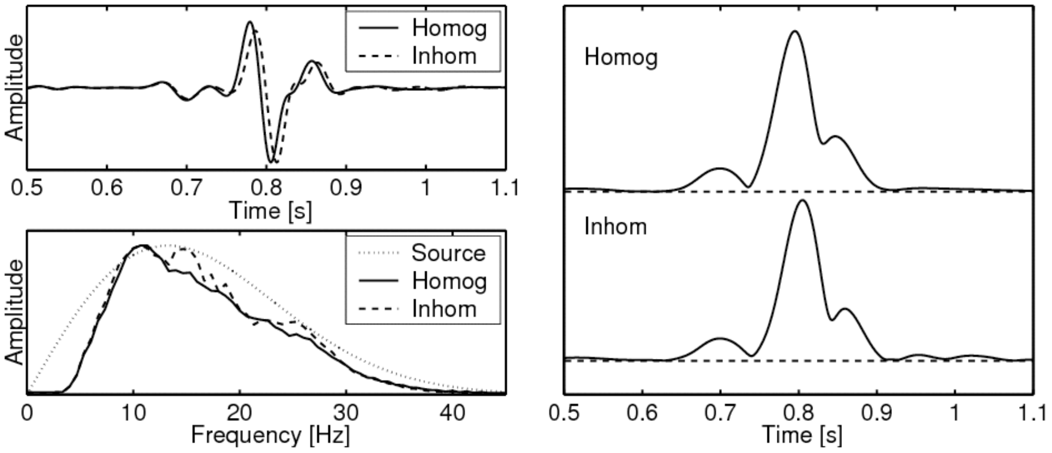

***Figure 2.15**: Seismograms, amplitude spectra and envelopes for the fault with small-scale inhomogeneities and a homogeneous reference model. Solid: Reference model which the average seismic properties of the inhomogeneous model, dashed: Model with small-scale inhomogeneities, dotted: spectrum of the source time function. Right column: corresponding envelopes of the traces.*

The seismograms and distributions of FZ wave amplitude are similar in both cases. The FZ wave trains, spectra and traces envelopes (Figure 2.15) also show no significant differences.

2.5.5 Low-velocity layer and vertical velocity gradient

Some FZ are expected to widen towards the surface due to decreasing confining pressure and to be covered with a low-velocity layer due to sedimentation. Models A and B (Figure 2.16, left) explore this configuration.

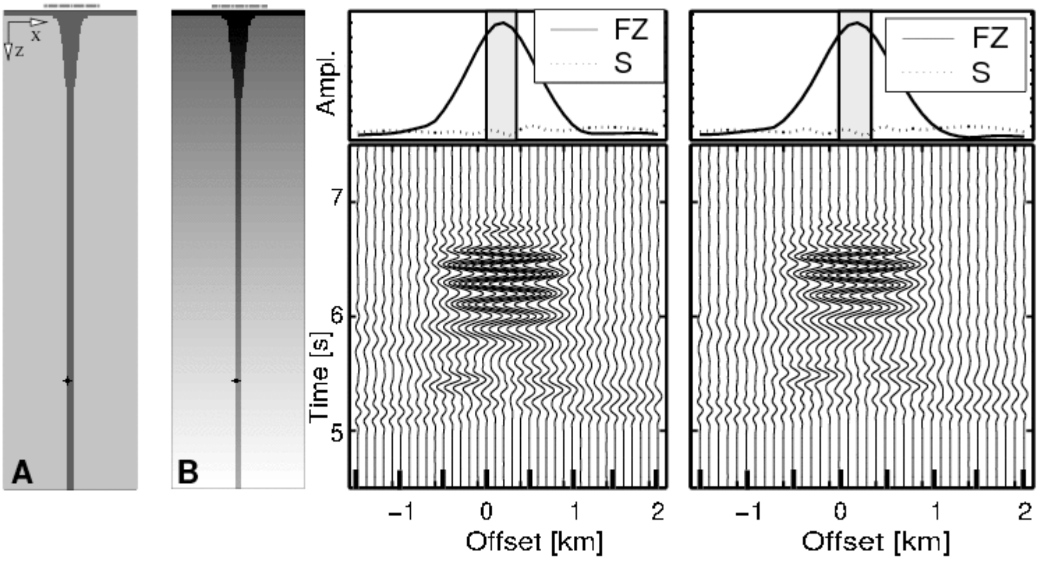

Figure 2.16: *Left: models with a fault widening towards the surface and a low velocity layer on top. The width at depth is 210 m the shallow width is 1170 m. The thickness of the low velocity layer on top is 150 m. Model A: constant seismic properties at depth. Model B: velocities and density increase with depth. Middle: seismograms for Model A. Right: seismograms for model B.*

A 2D modelling of such a structure can be found in Li and Vidale, 1996. The FZ width at the lower part of the model is 210 m and the source is located at 12.5 km depth. In both models, the same fault geometry is used and in both cases the velocities and the density of the fault is lowered by 25% with respect to the background.

Model A has uniform properties at depth, but in model B the velocities and the density increase with depth similar to Figure 6 of Ben-Zion et al. (1992) based on travel time tomography for the Parkfield section of the San Andreas fault. At the bottom of model B the density and the velocities are 20% higher than at the surface. A full description of the model parameters is given in Figure 2.16 and Table 2.1.

In both models, the path length of the trapped waves travelling through the fault is 60 FZ widths and thus relatively long compared to the previous models. In the absence of attenuation, the number of oscillations and hence overall duration of the FZ waves are proportional (for a fixed FZ width) to the length of the path inside the fault (Igel et al., 1997). High attenuation in the FZ, not accounted for here, will act as a low pass filter tending to reduce the complexity and duration of the FZ wave train with increasing path length along the fault (Ben-Zion, 1998).

In Model A with uniform properties at depth the distribution of the amplitudes is approximately Gaussian with a half length of 3 FZ widths (Figure 2.16, center). The size of the maximum FZ wave amplitude is 8 times the S-wave amplitude.
The seismograms in model B with increasing properties at depth are similar to the effects in the previous case (Figure 2.16, right). The spectra and envelopes of traces show no significant differences and the only effect visible being a phase shift in the FZ wave forms (Figure 2.17). Thus, fairly severe variations of material properties with depth are insignificant variables for the generation and properties of FZ guided waves.

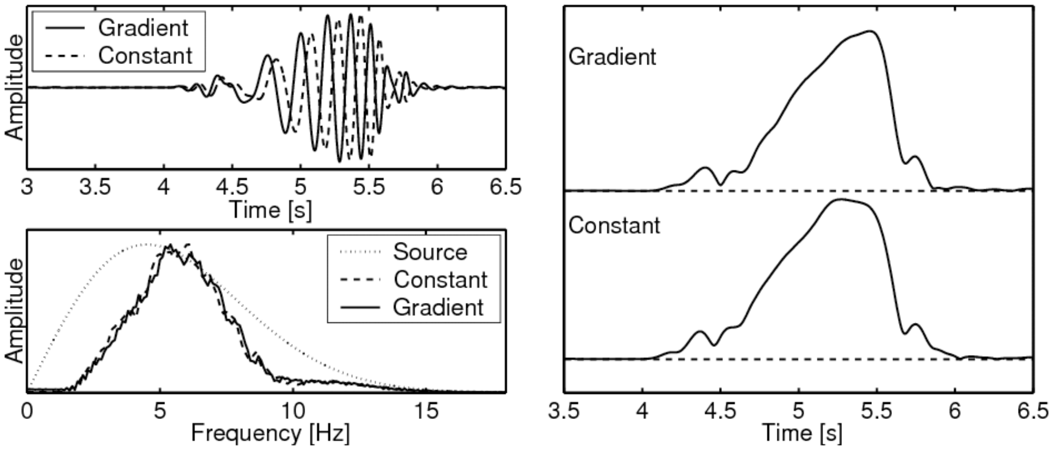

Figure 2.17: *Left column: trace with the maximum FZ wave amplitude (top) and the corresponding amplitude spectrum for a fault widening towards the surface and a low velocity layer on top. Solid: model with increasing velocities and density with depth (gradient model), dashed: model with constant properties (constant model), dotted: spectrum of the source time function. Right column: corresponding envelopes of the traces.*

2.5.6 The Shallow-Fault model

A structure which is discussed for an increasing number of fault systems is a low-velocity zone with a relatively shallow depth extension. For *deep* fault zone structures sources outside the fault can not generate significant trapped waves inside the fault zone.
The focus of this section is to investigate whether this is the case also for *shallow* fault structure. The results have implications on questions in seismic hazard analysis: for example, whether trapped wave recordings from deep earthquakes are an indication for deep fault zone structure or not, and if the source volume which is capable of generating trapped waves for shallow faults is larger than the corresponding source volume for deep fault zones.

The three models shown in Figure 2.18 are designed to give a first insight to this question, focussing on the influence of a lateral variation of the source position which is located in the host rock, well below the shallow fault. The source is located directly below the fault (Model A), laterally shifted resulting in a vertical incidence angle towards the bottom of the fault of approximately 30° (Model B), and shifted towards a vertical incidence angle of 45° (Model C).

For all models, the source depth is 6000 m and the width of the fault zone is 270 m. The shallow low-velocity fault zone extends to a depth of 4000 m. The grid spacing is 30 m and the receiver spacing is 100 m. The dominant wavelength of the S waves within the fault zone of approximately 500 m. The corresponding y-component velocity seismograms for a Gaussian source time function with dominant frequency of 4 Hz are shown in Figure 2.19. The receivers 11-13 are located directly on top of the fault.

Model A (left) shows no prominent trapped wave arrivals. This is caused by the strike-slip radiation pattern of the source which has a nodal plane in the x-y plane directly at the centerline of the fault.

For model B (center) the traces show significant trapped waves, generated by the radiated body wave which enters the low-velocity channel through the bottom side of the fault.

The seismograms for model C (right) also show trapped waves with a similar amplitude compared to model B, despite the longer distance which the body wave travels between source and the faults' bottom. Models B and C show that sources well outside and below a shallow fault are capable of generating significant trapped wave arrivals in the seismograms.

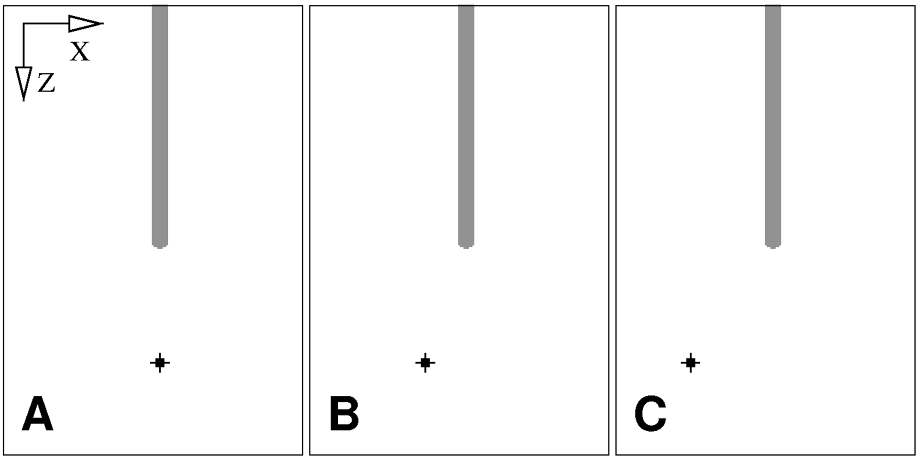

Figure 2.18: *Three models with source positions (A) vertically below, (B) with an incidence angle of 30°, and (C) with an incidence angle of 45° towards the fault zone's bottom end.*

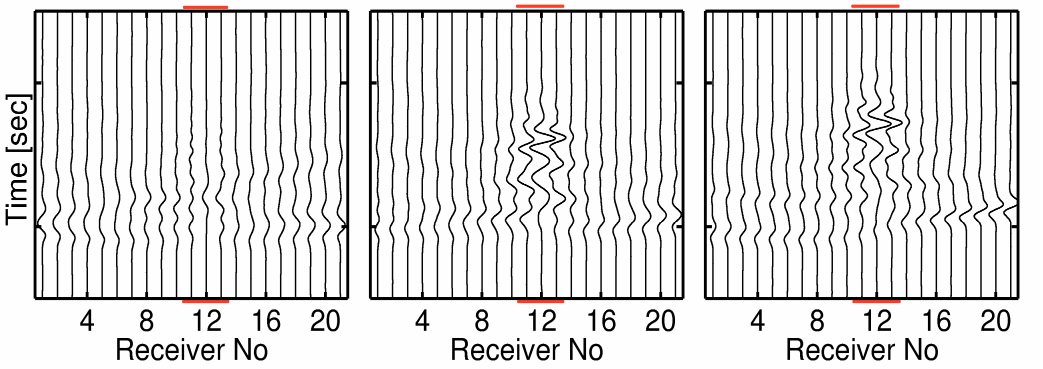

Figure 2.19: *y-component of velocity (drawn to scale) recorded at a receiver array crossing the fault for models A, B, and C. The receivers 11-13 are situated directly on top of the low velocity zone which is marked by the red lines. Prominent trapped waves occur for only models B and C where the source is located below and shifted laterally away from the fault zone.*

2.5.7 Sources outside shallow faults

The first insights in the shallow fault model shown in the previous section initiated an extensive study to quantify the size and the shape of the source volume which is capable of generating strong trapped waves. The results are published in *Guided waves from sources outside faults: an indication for shallow fault zone structure?* (Fohrmann, Igel, Jahnke, Ben-Zion, 2004). Since this work provides important insights about trapped wave generation, this study is discussed here and one Figure from Fohrmann et al. (2004) is included for illustration.
In order to quantify the source volume which is capable of generating significant trapped wave energy at the surface, a dense regular grid of sources is defined (Figure 2.20, top left). A detailed description of the used model can be found in Fohrmann et al. (2004). For each source location a complete simulation was performed, which altogether required significantly higher computational resources compared to previous simulations of this chapter. For each simulation, the energy ratio of the recorded trapped wave signal versus the direct S wave signal was calculated for a selected receiver situated directly on top of the fault zone.

The resulting 3D dataset of energy ratios was visualized using interpolated iso-surfaces for ratios of 2 (Figure 2.20, top right), 5 (bottom left) and 10 (bottom right). In general, the resulting source volumes are surprisingly large and in all cases they comprise regions which are at several kilometers distance from the fault zone. Another remarkable feature of the iso-surfaces is that they are open to greater depths, indicating that there is no maximum source depth for generating a given energy amplification ratio.

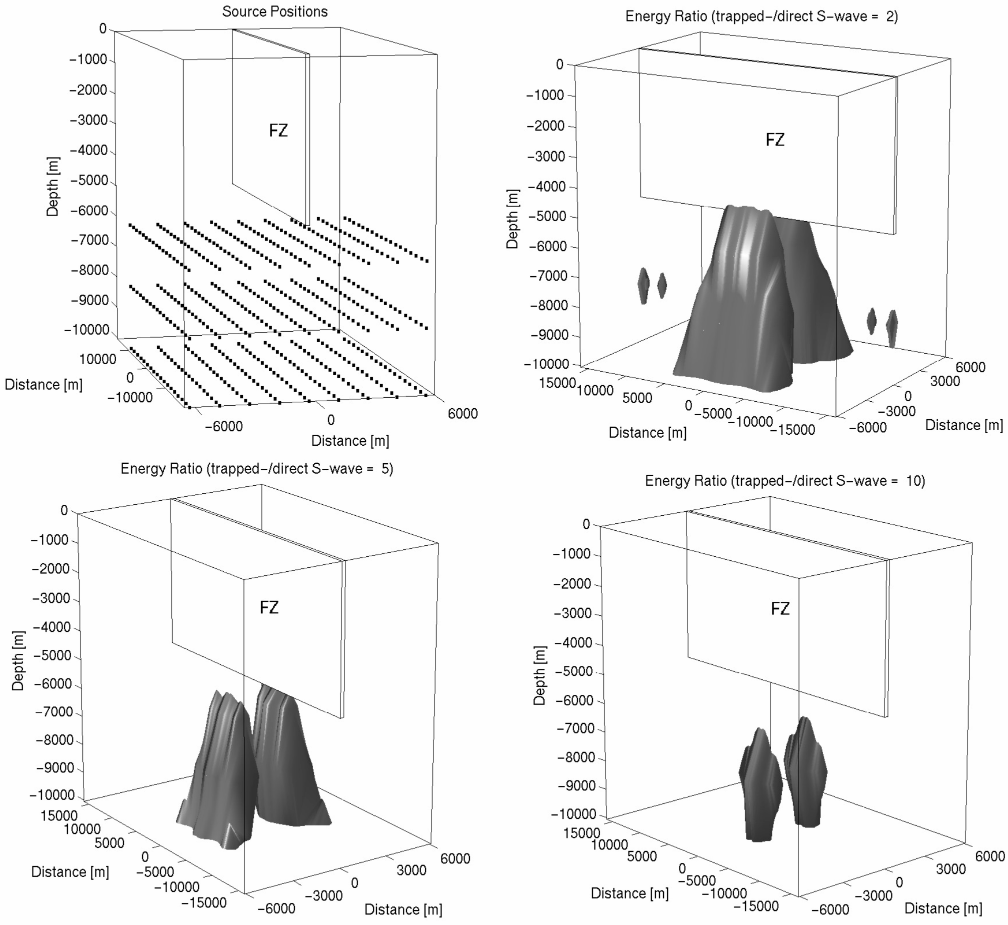

Figure 2.20: *Modelling of a shallow fault zone with sources well outside and below the fault (Fohrmann, Igel, Jahnke, Ben-Zion, 2004). Top left: grid of sources for which individual simulations were performed. For better visibility, only every 15th source in x-direction is shown. Top right: source volume whose corresponding energy ratio of trapped wave versus S-wave exceeds a factor of 2. Bottom left: source volume for an energy ratio of 5. Bottom right: source volume for an energy ratio of 10.*

It is important to note that the size and shape of the calculated source volumes depend on the selected source mechanism which is here a double couple with non-zero moment tensor components $M_{xy} = M_{yx} = M_0$, analogous to the calculations shown above. Actually, a variety of source orientations can be expected near a fault zone, resulting in larger source volumes as those calculated here.

Due to the large number of simulations which were necessary to sample the whole source volume the calculation had to be performed on a high-performance parallel-computer with distributed memory architecture. To take advantage of such systems the finite difference code previously used in Jahnke et al. (2002) was parallelized for this system by *myself*. The resulting code (*Fault3D*) resides at *www.spice.rtn.org*.

2.5.8 The Split-Fault models

A common structural feature often visible at the surface is an offset separating two fault segments. However, the extent to which fault offsets seen at the free surface persist at depth is not generally known. Increasing confining pressure and temperature with depth may tend to lessen structural complexity such as fault offsets. Imaging the continuity of fault surfaces at depth is important for seismic hazard estimates because the largest possible event magnitude is likely to correlate with the extent of the continuous fault structure.

Harris and Day (1993) and Li and Vidale (1996) examined, respectively, properties of dynamic rupture and FZ waves in models with surface structural offset that persist to depth. Here we analyze simulations of FZ guided waves in a split-fault consisting of two segments that are offset at the surface but connected at depth. The depth of the bifurcation point of the segments is 3990 m and the source depth is 2010 m below the bifurcation point. Additional model properties are described in Table 2.1.

Two simulations for this geometry were performed, with the source (1) placed directly below the bifurcation point, and (2) shifted laterally, parallel to the fault plane. The amplitudes at the receiver lines for both split-fault models are affected by varying geometrical spreading factors and also by the shape of the FZ. To be able to separate the influence of geometrical spreading from the structural effect of interest, a comparison with a basic fault with comparable source receiver setup was performed.

Split-fault with centered source

The model geometry of the split-fault with centered source is shown in Figure 2.21 (left), together with the geometry of the basic reference fault (center).

For both models, six receiver lines are placed across the fault at different distances from the end of the fault segments, for analyzing the influence of the segmentation on the trapped wave field near the fault offset (Figure 2.21, right).

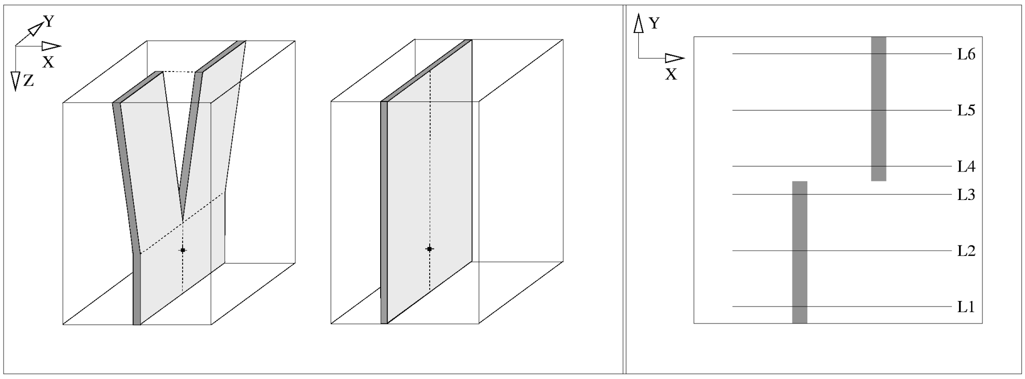

Figure 2.21: *Left: model with a fault zone split at the surface but connected at depth. The source location is indicated by a star. Center: reference model of a basic fault. Right: location of receiver lines L1-L6 at the surface, located on top of the fault zone which is indicated by gray shading.*

In Figure 2.22 (top) synthetic seismograms for the receiver lines L1-L3 are shown for the basic model and for the split-fault model, respectively. For reasons of symmetry, the receiver lines L4-L6 are not displayed.

The signals of the trapped waves for the basic fault model (Figure 2.22, top) are very similar for all receiver lines, indicating that moderate shifts of the receiver position along the fault do not significantly influence the trapped wave recordings. The main effects of the different distances from the source to each receiver line in the basic model are small changes to the arrival times. The effect of the receiver position on the FZ amplitudes is negligible.

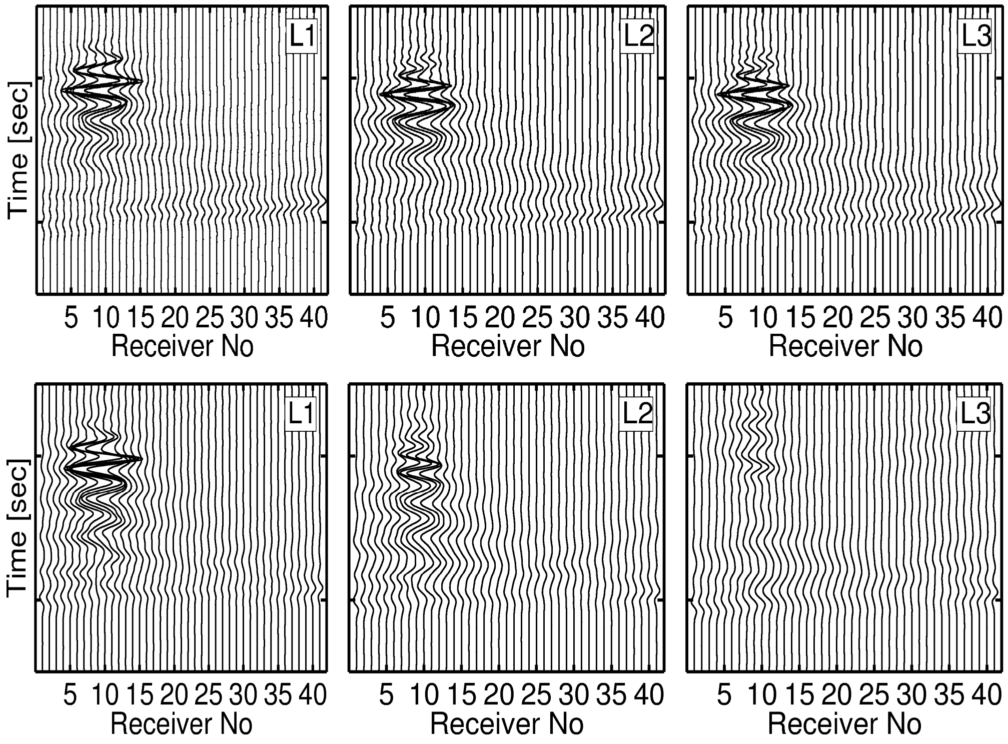

Figure 2.22: *Top: Horizontal components of velocity seismograms across profiles L1-3 on the fault for the basic fault structure shown in the previous Figure. Bottom: Horizontal components of velocity seismograms for the same profiles for the split fault model.*

This is different for the split-fault (Figure 2.22, bottom): as long as the receiver is located at some distance from the fault discontinuity the trapped wave arrivals resemble those generated by the simple fault. The closer the receiver line is situated to the discontinuity, the weaker the amplitudes of the recorded trapped wave signals are. This indicates that the source receiver geometry with respect to the location of a fault discontinuity is crucial for being able to resolve such structures. Moreover, the recordings of a single receiver line which is placed near a fault discontinuity would be misinterpreted by assuming a simple fault structure. Such differential effects may be used to better derive fault zone structure at depth.

Split-fault with shifted source

Compared to the previous setup, the source location in this model is shifted laterally 990 m along the fault in the y-direction away from the center of the split. The source is located below one branch of the fault and trapped wave energy that is transmitted into the second branch has to pass below the bifurcation point. The locations of the receiver profiles are identical to the previous model (Figure2.21, right). The model setup is shown in Figure 2.23 (left).

For each fault segment the synthetic seismograms of the receiver line with the strongest trapped wave amplitudes is shown (Figure 2.23, center and right), which is L2 and L4, respectively. Additionally, the maximum amplitude distribution of all receiver lines is shown on top of the seismograms.

The receivers crossing the branch which is located above the source show a maximum FZ wave amplitude of 4 times the S-wave amplitude. FZ waves also arrive on top of the other branch with a maximum amplitude of 2.5 times the S-wave amplitude. Even with a source shifted towards one branch, trapped waves can be seen on top of both segments of the fault.

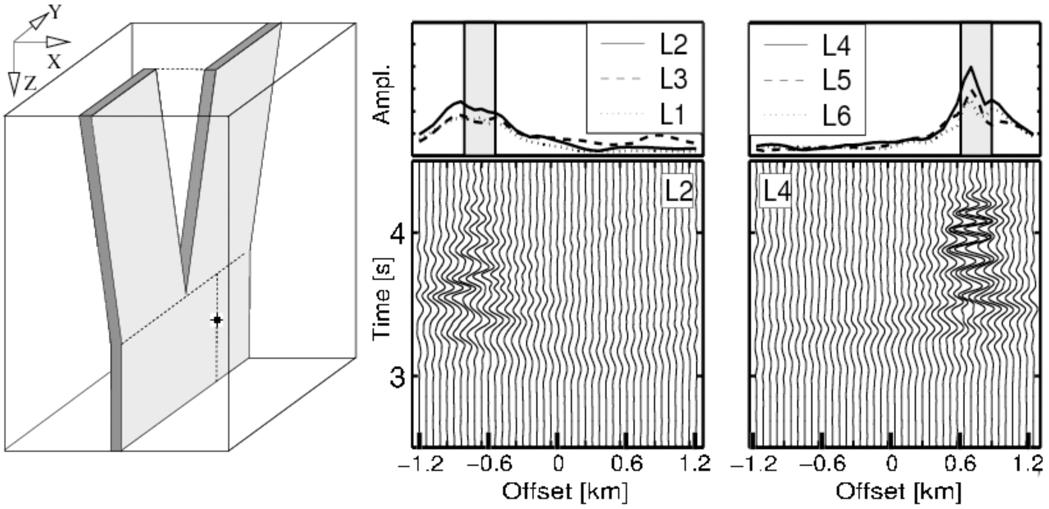

Figure 2.23: Left: Split-fault model with the source shifted laterally. Middle: Seismograms of receiver line L2 situated on top of the forepart of the fault (cf. Figure 2.21). Right: Seismograms for receiver line L4 situated on top of the rear part of the fault. The seismograms of the receiver line with the strongest FZ waves on each fault segment and the maximum amplitude distributions of all six receiver lines are shown. Even the stations on profile L1-3 of the fault show clear FZ wave arrivals.

2.6 Discussion

We now summarize and classify the results presented in the previous section in terms of weak, moderate and strong effects of 3D structural perturbations to a basic 2D FZ. Then we discuss further results of the shallow fault model, the split-fault model and the implications of the parameter-space study done in this work for imaging discontinuous FZ structures at depth.

2.6.1 Weak effects

In real faults one expects an increase of seismic velocities and density with depth. To analyze this, a linear gradient of seismic velocities and density was applied to models with a fault widening towards the surface and a horizontal low velocity layer (Figure 2.16 left, Model B). For both models the maximum FZ wave amplitude, the spectra and the traces envelopes resemble closely those of the basic FZ, the only difference being a phase shift of the FZ wavelets (Figure2.17). It thus seems difficult to derive information about a vertical gradient of seismic properties from the amplitude, spectrum or envelope information of FZ waves.

The model with small-scale 3D variations of the seismic properties within the FZ (Figure 2.14, left) shows that FZ waves are almost unaffected by those perturbations. Despite the strong variation of the seismic properties inside the fault, clear FZ waves develop and lead to considerable amplification. The FZ wave amplitudes, wave forms, spectra and envelopes are very similar to those in the homogeneous reference fault model with average seismic properties (Figure 2.14, middle and right). Therefore small scale inhomogeneities with scale lengths considerably less than the dominant wave length can not be resolved from seismograms. This result is in agreement with Igel et al. (1997) who suggested that trapped waves average out irregular FZ geometries with correlation length smaller than the FZ width.

2.6.2 Moderate effects

The influence of gradual variations of the FZ shape on the trapped waves is moderate. This result is in agreement with 2D modeling of faults widening towards the surface done by Li and Vidale (1996). For shape perturbations that are not too strong, the resulting FZ wave field is similar to the FZ wave field of an unperturbed fault.

Since such modifications can be done in many ways, we focus on models with reduced FZ width at a certain depth (Figure 2.10). The longer the guided waves travel in a FZ section with reduced width, the earlier these FZ waves arrive at the seismometer (Figure 2.11). Also the maximum FZ wave amplitude is reduced when the waves travel part of the way along a narrow FZ section, compared to the undisturbed FZ case. Given the large differences in the geometry of the considered models, the effect of gradual shape changes on the travel time is negligible and the effect on the FZ wave amplitude is moderate. Overall, gradual variations of the FZ shape have less influence on guided waves than the source location and a lateral discontinuity of the fault.

The effect of a FZ widening towards the surface and merging with a horizontal low-velocity layer on top of the fault (Figure 2.16 left, Model A) is also moderate. Such a FZ configuration leads to a Gaussian-shaped spatially-smeared region of enlarged FZ wave amplitudes. This effect can also be seen in Li and Vidale (1996) and Igel et al. (1997). Because of the wider distribution of FZ wave energy, the maximum amplitudes are comparatively low. Without taking this subsurface structure into account one would image a broader fault zone with a lower velocity contrast by analyzing FZ seismograms with 2D models.

In general, the 3D ingredients discussed in sections 4.1 and 4.2 produce minor and moderate forms of diffusion of the FZ waves, respectively. Strong effects, which may destroy or reduce significantly the guided waves energy, are 2D or quasi-2D perturbations that are summarized next.

2.6.3 Strong effects

The variation of source location with respect to FZ can drastically influence the resulting wave field. To quantify this, a basic fault with three different source locations was investigated (Figure 2.3). The employed source mechanism corresponds to localized strike-slip dislocation (double-couple). For this source the strongest FZ amplitudes occur for sources located at the FZ boundary (Figure 2.4).

In contrast, a hypocenter location near the FZ center leads to destructive interference of FZ waves and to small FZ wave amplitudes. Similar results were found by Li and Vidale (1996) with 2D modelling and Ben-Zion (1998) with 2D analytical calculations. If the source has an isotropic radiation pattern corresponding to an explosion, no such destructive interference occurs and strong FZ wave amplitudes develop also for a source in the center of the FZ (Li and Vidale, 1996).

Sources located outside the FZ with normal distances larger than the FZ width produce weak or no FZ waves. However, Ben-Zion (1998) showed that if the low velocity FZ layer has an adjacent transition zone with intermediate properties between those of the FZ layer and the host rock, considerable trapped waves energy can be generated by sources in the transition zone that are far from the FZ core. Igel et al. (2001) also showed that favourably oriented sources below and aside a shallow FZ layer can produce significant trapped waves in the shallow FZ layer.

Another FZ parameter that influences strongly the resulting FZ waves is a lateral discontinuity of the fault (Figure 2.6). A 2D modelling of such a structure is shown in Li and Vidale (1996). For the model with a lateral offset of 1/2 FZ width, the distribution of the FZ wave amplitudes mirrors the location and width of the upper part of the fault (Figure 2.7). Analyzing the seismograms without any knowledge of the underlying structure would lead to the correct fault width by assuming a simple, continuous fault. The slightly lower amplitudes of the FZ waves could lead to a slightly lower velocity contrast of the estimated simple fault structure.

This loss of energy which occurs at the fault disruption appears in the seismograms as spatial smeared out arrivals between S-wave and FZ-wave and can also be seen in the wave propagation snapshots in Figure 8 of Igel et al. (2001). For a lateral offset of 1 FZ width the FZ wave amplitudes are 4 times the S-wave amplitudes, that is 50% of the amplitude of the previous model. The zone of increased amplitudes is less distinct compared to the previous model. Thus the deviation of the FZ width from this parameter has a bigger uncertainty.

For the model with a shift of 3/2 FZ width the amplitudes are less than 2.5 times the S-wave amplitudes. Therefore, in this case the amplitude is not a good indicator for distinguishing between trapped and direct S-waves. Estimating the FZ width based on the zone with FZ waves would lead to a 3-fold overestimation of FZ width and an underestimation of the velocity contrast by assuming a simple fault structure.

2.6.4 The Shallow-Fault model

The assumption which has often been made in previous studies that sources which generate trapped waves must be located at or within a low-velocity fault zone layer which is continuous between source depth and surface may lead to false conclusions about the actual structure at depth. The shallow-fault modelling shows that even sources which are located well below and outside the fault zone can generate strong guided waves.

This result raises the question how shallow and deep faults can be distinguished by trapped wave analysis. A promising effect was found by Wu et al. (2008): in their numerical study they discovered a frequency dependence of the trapped wave signal as a function of depth where the trapping takes place. This effect is a candidate criterion for distinguishing shallow and deep fault zones. By taking this into account the accuracy of seismic hazard estimations could be significantly improved, for instance, for the estimation of the maximum possible rupture size of future earthquakes which is related to the maximum magnitude of earthquakes occurring at the fault. Moreover, the enlarged source volume in the vicinity of the fault which has to be taken into account for potential generation of trapped waves causes a higher probability of strong amplification effects on top of the fault.

2.6.5 The Split-fault model

The last model type investigated in this study was motivated by a central question concerning fault structures. Often two or more parallel fault segments that are separated by a gap perpendicular to the sections are visible at the surface and it is not clear whether these segments are connected at depth. The ability to image such structures would have important implications on maximum expected earthquake size and a variety of other issues of earthquake and fault dynamics. If FZ waves generated by a given source are visible on different fault segments, these segments are likely to be connected at depth.

The two split-fault simulations performed show that for such geometries trapped wave generation is a robust feature. For a source centered between the two segments clear trapped wave arrivals occur as long as the receivers are positioned at some distance to the fault disruption. Moreover, for sources shifted from underneath the bifurcation point towards one fault segment trapped waves occur not only in the fault segment above the source location but also, with weaker but still prominent amplitudes, on the other segment. It is possible that for larger lateral shifts, trapped waves will be observed only on top of one segment.

2.6.6 Comparison with other studies

As the results presented contain new geometries, source-receiver setups and source types it is important to compare the conclusions and implications with those of previous studies.

Ben-Zion (1998) analyzed the 2D scalar wave field for fault zones consisting of two vertical layers between two quarter spaces. The source was an SH line dislocation oriented parallel to the fault structure. The work focused on a parameter-space study aiming to clarify effects of, and trade-offs between, propagation distance along the fault, FZ width, source position within the FZ, velocity contrast across the fault, attenuation coefficient of FZ material, receiver depth and normal offsets of source and receivers from the FZ. All these variables were shown to have significant effects on FZ guided waves, and thus all are important variables in inversions of observed guided waves. The analytical solution of Ben-Zion (1998) can be computed quickly and a large number of models can be tested in a systematic examination of the parameter space spanned by the above sensitive parameters.

However, due to the restriction on the 2D scalar wave equation, the method is limited to uniform fault structures and either P or SH wave propagation. Igel et al. (2001) demonstrated that another short coming of the 2D analytical solution associated with the assumed line source can be corrected by applying a convolution filter, as was done earlier by Li and Vidale (1996). Such 2D-3D transformation filter may not work correctly for some complex structures and 3D elastic waves (see Igel et al. (1993) for examples).

Li and Vidale (1996) investigated 2D fault models with an acoustic FD method, solving the SH wave equation. Their work focused on effects of structural discontinuities, surface layers, and other heterogeneities in 2D. Those models that can be compared to the present study show the same principal characteristics, e.g. concerning effects of source radiation pattern, source location, surface layers, varying FZ width at depth and fault disruption. Additionally, they investigate fault kinks, varying FZ widths and fault zones buried at different depths.

Igel et. al (1997) performed SH and P-SV wave propagation in cylindrical coordinates for axi-symmetric models. The modelling focuses on tradeoff between propagation distance of the FZ waves and FZ width, the source location relative to the FZ, FZ widening towards the surface, low velocity surface layer, horizontal velocity gradient within the FZ, a FZ with vertical heterogeneities and small scale scatterer in the FZ.

In the present work we extend the parameter-space study of Igel et al. (1997) to true 3D cases and examine effects of source location with respect to the fault, FZ width, FZ velocity contrast, varying FZ width with depth, a FZ capped at the surface, discontinuous faults and shallow fault structures.
The following statements summarize our results and these of Igel et al. (1997, 2001):

1. FZ waves are highly sensitive to the source location.
2. A low velocity surface layer can distort and attenuate FZ waves.
3. Gradual variations of the FZ shape like a varying FZ width have minor influence on the trapped waves.
4. A lateral disruption of more than one FZ width can reduce considerably the efficiency of FZ wave propagation.
5. A shallow FZ is capable of guiding trapped waves.
6. Varying the source location within the FZ has a strong effect on the radiation pattern and thus the efficiency to generate trapped waves.
7. Faults with increasing width towards the surface showed a spatial smearing and decreasing of amplitudes.
8. Small-scale scatterers do not obstruct the trapping efficiency of faults.

2.7 Conclusions

Currently, the structure of fault zones at depth is a question of great interest. Seismic FZ waves may be one of the most diagnostic tools for imaging fault structures. Observed FZ guided waves can be well explained and interpreted with simplified 2D FZ structures (e.g. Li and Leary (1990), Li et al. (1994a), Michael and Ben-Zion, 1998, 2001; Peng et al., 2000). This is perhaps not surprising since an ideal seismic wave guide is 2D and thus FZ waves will not exist in structures that are too heterogeneous to be approximated, over a given spatial extent and for the relevant frequencies, as 2D.

To clarify how various realistic deviations from the 2D cases would alter the wave field, we have analyzed a set of FZ models starting from a basic FZ and varying different geometric and seismic properties separately to understand the influence of these variations on the FZ wave field. Some of these variations were combined in a study of a structure consisting of a fault that splits into two fault segments towards the surface.

In agreement to former studies based on 2D analytical and numerical calculations (Ben-Zion, 1998; Li and Vidale, 1996), we find that a source location inside a fault does not necessarily lead to strong FZ wave amplitudes. Depending on the location with respect to the FZ boundaries, the radiated wave field may destructively interfere leading to low FZ wave amplitudes.

Also other effects previously investigated with 2D methods (e.g. Li and Vidale, 1996; Igel et al., 1997) can be confirmed: FZ waves are highly sensitive to the source location with respect to the fault. A shift of the source location by less than the wave length may lead to strong variations of the FZ waves. Yet, from this we may not conclude that FZ guided waves can not be generated by sources outside the core of the FZs.

As shown by Ben-Zion (1998), sources in a transition zone bounding a FZ layer can produce considerable trapped wave energy. In addition, dislocation sources located outside and below a shallow vertical low-velocity layer by many FZ widths with appropriate orientation and location can lead to trapping of considerable seismic energy in the shallow structure (Igel et al, 2001). Moderate effects occur by variations of the internal shape of the fault. No significant influence on the FZ wave propagation is caused by small scale inhomogeneities inside the fault or a realistic vertical velocity gradient.

A 3D fault system that is continuous at depth and forks into two segments towards the surface is capable of guiding FZ waves in both segments as long as the source is below the bifurcation. Otherwise, if the fault has a disruption greater than the FZ width, trapped energy is not able to propagate across this gap and no large amplitudes caused by FZ waves occur. Thus the simultaneous detection of FZ waves on different fault segments indicate that these segments are connected at depth. This information is important to estimate the overall size of a connected fault plane and thus the maximum magnitude of an earthquake occurring on that fault plane (Li et al., 1994a,b).

The modelling of elastic 3D wave propagation in fault zones is an important tool for analysis of real data and can help to design new experiments. Further research is needed to investigate optimal source-receiver setups with which some of the 3D structures discussed here can be reliably imaged using FZ guided waves. Detailed knowledge of FZ structure at depth may lead to considerable progress for shaking hazard assessments, the estimation of likely earthquake magnitudes and the (future) dynamic behaviour of large fault systems.

Acknowledgments

We gratefully acknowledge the Enigma Project for High Performance Computing in Geophysics at the Institute of Theoretical Geophysics in Cambridge and the Leibniz Rechenzentrum in Munich for access to their supercomputers. YBZ acknowledges support from the Southern California Earthquake Center (based on NSF cooperative agreement EAR-8920136 and USGS cooperative agreement 14-08-0001-A0899).

Chapter 3:

Global axi-symmetric SH-wave propagation

Most of this chapter is published as *Global SH-wave propagation using a parallel axi-symmetric spherical finite-difference scheme: application to whole mantle scattering* (Jahnke, Thorne, Cochard and Igel, Geophys. J. Int., 2008). In addition, a discussion of other studies which used the SHaxi program is given at the end of this chapter.

3.1 Abstract

We extended a high-order finite-difference scheme for the elastic *SH* wave equation in axi-symmetric media for use on parallel computers with distributed memory architecture. Moreover we derive an analytical description of the implemented ring source and compare it quantitatively with a double couple source. The restriction to axi-symmetry and the use of high performance computers and PC networks allows computation of synthetic seismograms at dominant periods down to 2.5 seconds for global mantle models. We give a description of our algorithm (SHaxi) and its verification against an analytical solution. As an application, we compute synthetic seismograms for global mantle models with additional stochastic perturbations applied to the background *S*-wave velocity model. We investigate the influence of the perturbations on the *SH* wave field for a suite of models with varying perturbation amplitudes, correlation length scales, and spectral characteristics. The inclusion of stochastic perturbations in the models broadens the pulse width of teleseismic body wave arrivals and delays their peak arrival times. Coda wave energy is also generated which is observed as additional energy after prominent body wave arrivals. The SHaxi method has proven to be a valuable method for computing global synthetic seismograms at high frequencies and for studying the seismic waveform effects from models where rotational symmetry may be assumed.

3.2 Introduction

Despite the ongoing increase of computational performance, full 3D global seismic waveform modelling is still a challenge and far from being a routine tool for understanding the Earth's interior. Yet, for teleseismic distances, a substantial part of the seismic energy travels in the great circle plane between source and receiver and can be approximated assuming invariance in the out of plane direction. This motivates algorithms which take advantage of this invariance with a much higher efficiency compared to full 3D methods. A straight forward realization is to ignore the out of plane direction and compute the wave field along the two remaining dimensions. For example, Furumura *et al.* (1998) developed a pseudospectral scheme in cylindrical coordinates and invariance in the direction parallel to the axis of the cylinder for modelling *P-SV* wave propagation down to depths of 5000 km. This geometry corresponds to a physical 3D model with the seismic properties invariant along the direction not explicitly modelled. As a consequence, the seismic source is a line source having a substantially different geometrical spreading compared to more realistic point sources.

A different approach which circumvents the line source problem is the axi-symmetric approach. Here the third dimension is omitted as well, but the corresponding physical 3D model is achieved by virtually rotating the 2D domain around a symmetry axis. Seismic sources are placed at or nearby the symmetry axis and act as point sources maintaining the correct geometrical spreading. Since such a scheme can be seen as a mixture between a 2D method (in terms of storage needed for seismic model and wave field) and a 3D method (since point sources with correct 3D spreading are modelled) such methods are often referred to as 2.5D methods.

A variety of axi-symmetric approaches have been used in the last decades (e.g. Alterman and Karal, 1968). Axi-symmetric wave propagation for SH-waves in spherical coordinates with a FD technique was implemented by Igel & Weber (1995) to calculate seismograms for global Earth models and also by Chaljub & Tarantola (1997) to study frequency dependent effects of *S* and *SS* waves. Furumura and Takenaka (1996) applied a pseudospectral approach to regional applications for distances up to 50 km. Igel & Gudmundsson (1997) also used a FD method to study frequency dependent effects of *S* and *SS* waves. Igel & Weber (1996) developed a FD approach for *P-SV* wave propagation. Thomas *et al.* (2000) developed a multi-domain FD method for acoustic wave propagation and applied the technique to studying precursors to the core phase *PKPdf*. Recently, Toyokuni *et al.* (2005) developed a scheme based on the algorithm of Igel & Weber (1996) with extension to non-symmetric models for modelling a sphere consisting of two connected axi-symmetric half-spheres. Recently, Nissen-Meyer *et al.* (2007) presented a 2D spectral-element method for axi-symmetric geometries and arbitrary double-couple sources.

The main purpose of this paper is to (1) extend the axi-symmetric FD approach of Igel & Weber (1995) for modelling *SH*-wave propagation (SHaxi) for use on parallel computers with distributed memory architecture, (2) examine the properties of the implemented ring source and to show that it can be compared with a double-couple source, (3) as an application, to model the influence of whole mantle scattering on the seismic SH wave field. We furthermore present an application of the SHaxi method to modelling the *SH*- wavefield in models of whole mantle random *S*-wave velocity perturbations. In a companion paper (Thorne *et al.* 2007) we make an extensive comparison of SHaxi generated seismograms with results from recent data analyses of lower mantle structure. The SHaxi source code is available at: *www.spice-rtn.org*.

3.3 The axi-symmetric finite-difference scheme

3.3.1 Formulation of the wave equation

The general 3D velocity stress formulation of the elastic wave equation in spherical coordinates is given by Igel (1999). The coordinate system is shown in Figure 1. The relevant equations for pure SH wave generation are:

$$
\begin{aligned}
\rho\partial_t v_\varphi &= \partial_r \sigma_{r\varphi} + \frac{1}{r}\partial_\theta \sigma_{\theta\varphi} + \frac{1}{r\sin\theta}\partial_\varphi \sigma_{\varphi\varphi} + \frac{1}{r}(3\sigma_{r\varphi} + 2\sigma_{\theta\varphi}\cot\theta) + f_\varphi \\
\partial_t \varepsilon_{r\theta} &= \frac{1}{2}(\frac{1}{r}\partial_\theta v_r + \partial_r v_\theta - \frac{1}{r} v_\theta) \\
\partial_t \varepsilon_{\theta\varphi} &= \frac{1}{2}(\frac{1}{r\sin\theta}\partial_\varphi v_\theta + \frac{1}{r}\partial_\theta v_\varphi - \frac{\cot\theta}{r} v_\varphi) \\
\partial_t \varepsilon_{r\varphi} &= \frac{1}{2}(\frac{1}{r\sin\theta}\partial_\varphi v_r + \partial_r v_\varphi - \frac{1}{r} v_\varphi),
\end{aligned}
\tag{1}
$$

with: σ_{ij} : Stress tensor, v_φ: φ-component of velocity, f_φ: external force, ε_{ij} : Strain tensor, and ρ : density.

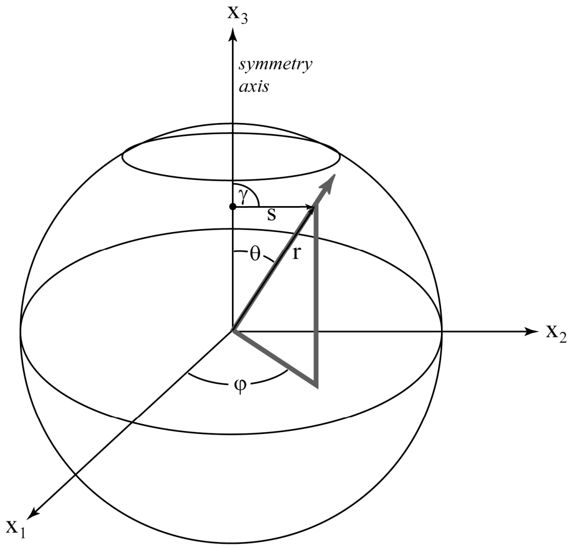

Figure 3.1: *Spherical coordinate system used in the formulation of the wave equation and the source description. All properties are invariant in the φ-direction. The distance from the Earth's center is denoted by r, and θ is the angular distance from the symmetry axis, γ is the take-off angle, and s is the source-receiver distance.*

In the axi-symmetric system, Eq. 1 can be further simplified by assuming the external source and model parameters are invariant in the φ-direction. The resultant equations are:

$$
\begin{aligned}
\rho\partial_t v_\varphi &= \partial_r \sigma_{r\varphi} + \frac{1}{r}\partial_\theta \sigma_{\theta\varphi} + \frac{1}{r}(3\sigma_{r\varphi} + 2\sigma_{\theta\varphi}\cot\theta) + f_\varphi \\
\partial_t \varepsilon_{\theta\varphi} &= \frac{1}{2}(\frac{1}{r}\partial_\theta v_\varphi - \frac{\cot\theta}{r} v_\varphi) \\
\partial_t \varepsilon_{r\varphi} &= \frac{1}{2}(\partial_r v_\varphi - \frac{1}{r} v_\varphi)
\end{aligned}
\qquad (2)
$$

Due to axi-symmetry, spatial properties vary solely in the r and θ-directions. Hence the computational costs of this formulation are comparable to 2D methods, while the correct 3D spreading of the wave field is still preserved, in contrast to purely 2D methods, provided the source is centered at the symmetry axis. Due to the *cot*(θ) term in Eq. 2, *SH* motion is undefined directly on the symmetry axis and the seismic source can not be placed there. We discuss the seismic source below.

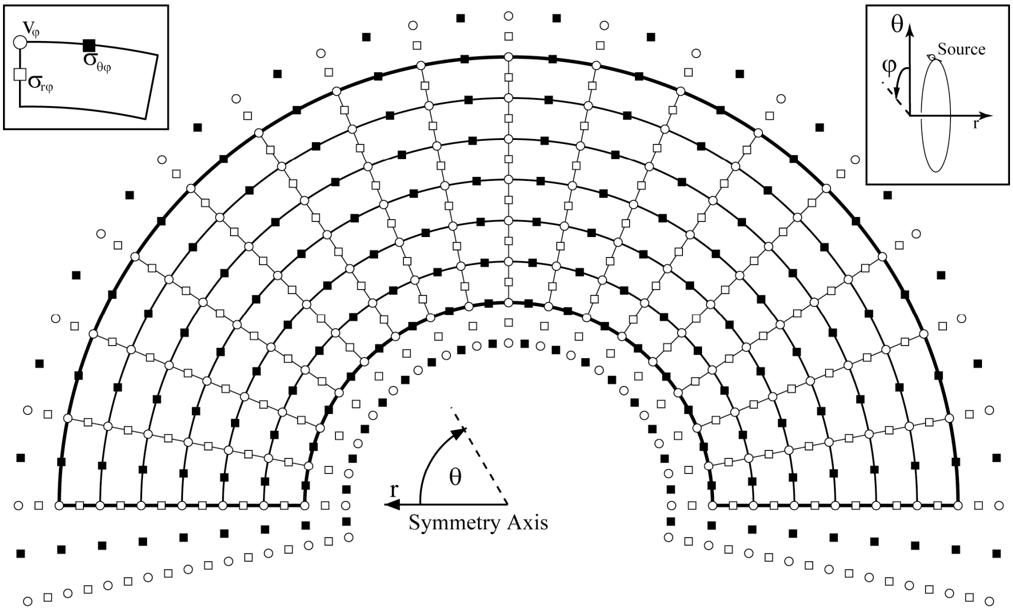

Figure 3.32: *The staggered grid scheme as used in the SHaxi algorithm. The origin of the coordinate system is placed at the Earth's center. The symmetry axis (θ=0°) is horizontally aligned as labelled at the origin. The model boundaries (surface, CMB and symmetry axis) are framed with thick lines. The additional points outside the model space are used for implementation of the boundary conditions. The symbols representing the wave field properties* v_ϕ, $\sigma_{r\varphi}$, *and* $\sigma_{\varphi\theta}$ *are labelled in the unit grid-cell shown in the top left corner of the figure.*

A staggered grid scheme was used for the discretization of the seismic parameters, so the stress components and the velocity are calculated at different locations. A schematic representation of the grid is shown in Figure 3.2. In addition to the grid points which define the model space, auxiliary points were added above the Earth's surface, below the core-mantle boundary (CMB) and beyond the symmetry axis ($\theta < 0°$ and $\theta > 180°$) for the calculation of the boundary conditions (discussed below).

3.3.2 Properties of the SH ring source

Due to axi-symmetry it is not possible to implement sources which generate the *SH* portion of an arbitrary oriented double couple. Moreover, exact point sources are not possible since *SH* motion is not defined directly at the axis but can be approximated when the wavelength of interest is made sufficiently larger than the grid size. We will discuss the properties of the implemented axi-symmetric *SH* source and show that its displacement far-field is proportional to that of an appropriately oriented double-couple source.

The SH ring source corresponds to the one used by Chaljub & Tarantola (1997) which found that the relative amplitude of the source depends on the take-off angle γ as $sin(\gamma)$. However, the complete source solution was not given although this is essential to perform a quantitative comparison of numerical and analytical solution. In order to derive the analytical solution of an SH ring source of infinitesimal size in a homogeneous isotropic elastic media, it is convenient to use Eq. (4.29) of Aki & Richards (2002), which gives the displacement field due to couples of forces, each of moment M_{pq}.

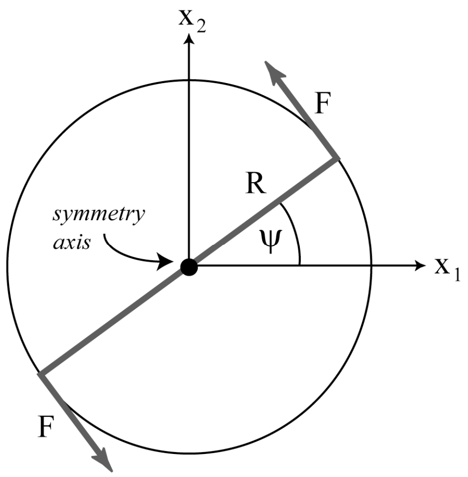

Figure 3.33: *Illustration of the ring source used in the SHaxi algorithm. The origin of the coordinate system corresponds to the symmetry axis. The ring source can be thought as a superposition of single forces F acting perpendicular to the radius vector* $R(\psi)$.

We start by noting that the ring source can be seen as the summation of individual couples of forces F over half the perimeter of a circle (see Figure 3.3), keeping in mind that the radius R ultimately tends to 0 and the forces tend to +∞, so as to have a finite moment (this is analogous to the discussion p. 76 of Aki & Richards (2002)). Projecting the forces on the axes x_1 and x_2, we can write that the moment due to this couple is:

$$dM(\psi) = 2F\cos(\psi)\cdot R\cos(\psi) - 2F\sin(\psi)\cdot R\sin(\psi) \tag{3}$$

with $F = |\vec{F}|$, and Ψ the orientation of the individual couple of forces F (see Figure 3.3).

Obviously, the total moment M_0 due to the ring force is $M_0 = 2\pi FR$, so the contributions from M_{21} and M_{12} are $(M_0/\pi)\cdot\cos^2(\Psi)$ and $-(M_0/\pi)\cdot\sin^2(\Psi)$, respectively. Inserting those expressions in Eq. (4.29) of Aki and Richards (2002), and further integrating from 0 to π, provides the full displacement field of an SH ring source of infinitesimal size:

$$v_\varphi^{Ring}(s,\gamma,t) = \sin(\gamma)\frac{-\beta M_0(t-s/\beta) + s\dot{M}_0(t-s/\beta)}{8\pi\rho\beta^3 s^2}, \tag{4}$$

with: v_φ^{Ring} : φ-component of displacement, ρ: density, β: S-wave velocity, $M_0(t)$, $\dot{M}_0(t)$: seismic moment and moment rate, t: S-wave travel time, s: source-receiver distance, and γ: take-off angle (see Figure 3.1).

This source will be compared with the far-field term of a strike-slip source (in the x_1/x_3 plane with slip along x_1) in the nodal plane for P radiation (φ=0). Using the equations analogous to Eq. 4.32 and 4.33 of Aki & Richards (2002) (with appropriate permutation of axis) we get:

$$v^{DC}(s,\gamma,t) = \sin(\gamma)\frac{\dot{M}_0(t-s/\beta)}{4\pi\rho\beta^3 s}. \tag{5}$$

We see that the far-field terms in Eq. 4 and Eq. 5 only differ by a factor 2. Hence, in the nodal plane for P radiation and for distances where the near and intermediate term can be neglected (i.e. more than a few dominant wavelengths, which is fulfilled for teleseismic investigations), the wave field of the SH ring source of infinitesimal size can be compared to that of the corresponding strike-slip source.

In contrast to the infinitesimal SH ring source described by Eq. 4, the source implemented in SHaxi is a finite ring. Yet, as we show in Section 3, the similarity between seismograms calculated for either source is close enough that the approximation of an infinitesimal ring source can be made.

3.3.3 Boundary conditions

At the symmetry axis, the free surface, and the CMB, adequate boundary conditions must be applied. For the horizontal surfaces (the CMB can be treated similarly to the free surface since *SH* waves reflect totally at both boundaries) the boundary condition is given by the zero-stress condition which requires $\sigma_{r\varphi} = 0$ for the surface (e.g., Levander 1988; Graves 1996). Due to the staggered grid scheme $\sigma_{r\varphi}$ is not defined exactly on the free surface but a half grid spacing below the surface (Figure 3.2). Therefore the zero-stress condition is realized by giving the auxiliary $\sigma_{r\varphi}$ grid points above the surface the inverse values of their counterparts below the surface at each time step (Figure 3.4). This results in a vanishing stress component at the surface in a first order sense. For the symmetry axis, the boundary conditions are derived from geometric constraints: all grid points beyond the axis are set to the values of their partners inside the model space, meaning that the fields are extended according to the axi-symmetry condition. Directly at the axis v_φ and $\sigma_{r\varphi}$ are set to zero since both values are undefined here according to Eq. 2.

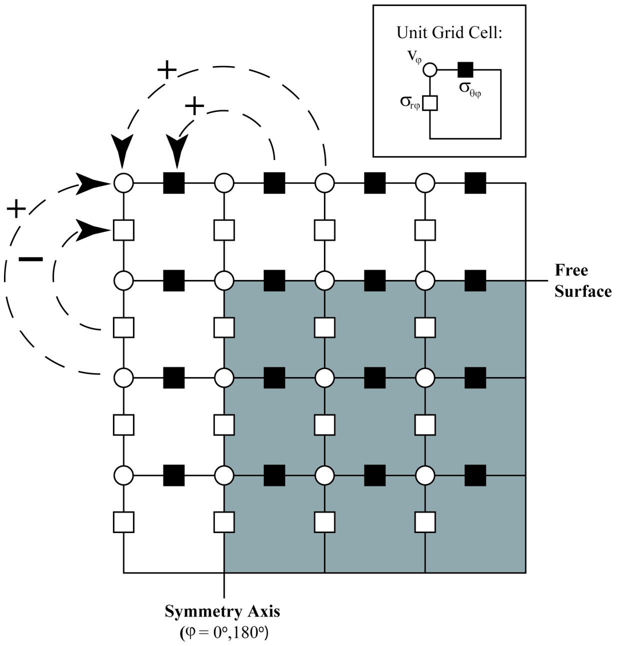

Figure 3.34: *Detail of the top-left corner of the SHaxi grid where the free surface and symmetry boundaries are encountered. The interior grid points (region underlain in grey) are part of the physical model space. To fulfil the boundary conditions, grid points outside of the physical model space (region not underlain in grey) must be added to the total grid. These outer points are updated at each time step by corresponding values of grid elements inside the physical model space, as indicated by the arrows and the plus (+) and minus (-) symbols.*

In general, the number of rows of auxiliary grid points which have to be added correspond to half the length of the FD operator used for the boundary condition. This enables the FD operator to operate across the boundary and calculate a derivative for grid points residing directly at the boundary.

For the simulations shown here a FD operator length of 2 at the model boundaries corresponding to one row of extra grid points is added. For the boundary at the symmetry axis this choice is crucial because convergence to the analytical solution is achieved *only* for the two-point FD operator. We do not yet understand why higher order operators fail here. For the grid points off of the boundaries a 4-point FD operator is used.

3.3.4 Parallelization

Actual high performance computers or workstation clusters usually consist of several units of processors (nodes) each having their own private memory. These nodes work independently and are interconnected for synchronization and data exchange.

In order to take advantage of such systems the model space is divided horizontally in several *domains*. Each domain can now be autonomously processed by a single node. Figure 3.5 shows such a *domain decomposition* for a total number of three domains. Similarly to the implementation of the boundary conditions described above, auxiliary grid points are added adjacent to the domain boundaries for the communication between the nodes.

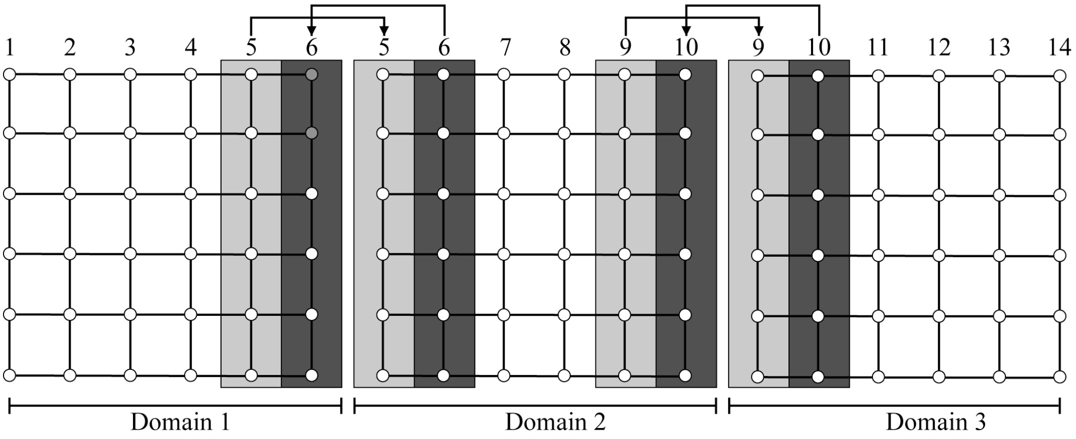

Figure 3.35: *Schematic illustration of the domain decomposition used for parallelization of the SHaxi algorithm. The model space is divided into multiple domains (here shown for three domains) which are each processed by an individual node. After each time step the grid points at the boundaries of the domain (grid points underlain in gray) are copied to the corresponding grid points of the adjacent domain. The lateral size of the gray regions correspond to half the FD operator length.*

This communication is implemented using the Message Passing Interface (MPI) library. The values of these auxiliary points are updated at each time step from their counterparts in the adjacent domain as indicated by the arrows in Figure 3.5 (points with identical column indices – underlain in gray). The number of columns of the auxiliary points must be equal to half of the FD operator length. We use a 4-point FD operator inside the model; therefore the auxiliary regions must be 2 points wide.

3.3.5 Computational costs

Compared to 3D modelling techniques the resources necessary for SHaxi simulations are comparatively low. Simulations with relatively long periods ~10-20 seconds can be done on a single PC within a couple of hours. For shorter periods the required memory and processing time increases strongly: The highest achievable dominant frequency f_{DOM} of the seismograms is inversely proportional to the grid spacing dx, whereas the time increment between two iterations is proportional to dx.

Thus the memory needed to store the (2D) grids is proportional to f_{DOM}^2 and the time needed to perform a simulation is proportional to f_{DOM}^3. A further performance increase can be achieved by limiting the model space in θ-direction by the maximum epicentral distance of interest. This reduces the number of grid points and consequently the needed memory and simulation time. The requirements on the system used for the simulations in this study give an idea about the achievable frequencies on supercomputers and PC clusters:

The 24-node, 2.4 GHz PC-cluster located at Arizona State University is capable of computing dominant periods down to 6 s for *S* waves at 80° distance (Table 3.1). For a simulation time of 2700 s the run time was about 2 ¼ days and each node needed 428 Mb of memory.

The 5 TFlop/s system of the Arctic Region Supercomputing Center “Iceberg" needed for the same run about 15.5 hours (Table 3.2). In general, on current supercomputer systems with peak performances well beyond 1 TFlop/s dominant periods below 1s can be achieved.

3.4 Comparison with the analytical solution

A first comparison of axi-symmetric FD methods was done by Igel *et al.* (2000). Good waveform fits of single seismograms were achieved for body waves, although the *SH* source was not examined in detail. In order to show that the SHaxi method provides the correct wave field we compare synthetic seismograms for two receiver setups with the analytical solution of a ring source (Eq. 4) in an infinite homogeneous media, with parameters shown in Table 3.3. The size of the numerical model was chosen so that reflected waves from the model boundaries were significantly delayed and therefore not interfering the time window of interest.

To quantify the difference between synthetic seismograms computed using SHaxi with the analytic solution, the energy misfit of the seismograms was computed. The energy misfit E of a time series x_i with respect to a reference series y_i is given by:

$$E = \frac{\sum (x_i - y_i)^2}{\sum y_i^2}, \tag{8}$$

(e.g., Igel *et al.* 2001). Good agreement between the seismograms and the analytic solution can be said to be attained if the energy misfit is below 1%. Two receiver configurations, shown in Figure 3.6a and 3.7a, were used for the following purposes: (1) a circular array consisting of 15 evenly spaced receivers placed on a half circle with the source in its center. This setup covers the whole range of possible take off angles and is optimally suited for investigating the angular source radiation; (2) a linear array with the receivers placed on a straight horizontal line originating from the source.

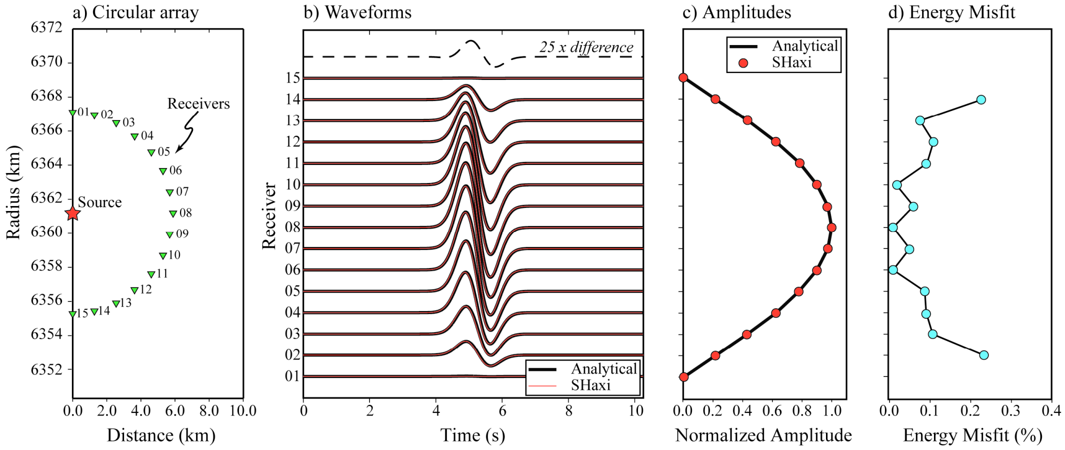

Figure 3.36: *a) Source-receiver setup of the circular array used to examine the angular variation of the radiation pattern. In this setup the entire range of take-off angle is covered. b) Numerical FD (red solid line) and analytical (black solid line) seismograms for the array. The dashed line on top shows the difference trace for receiver no. 8 scaled by a factor of 25. c) The maximum FD amplitudes of all traces (red filled circles) are plotted on top of the analytical curve (solid line). d) The energy misfit of the FD solution with respect to the analytical solutions. Receivers 01 and 15 are on the nodal SH plane and the energy misfit is undefined. The energy misfit across all receivers is less than 0.3%.*

Table 3.1. Example SHaxi parameters and performance – Linux Cluster.

Grid Size				Number of Time Steps	Memory Usage[c]	Dominant Period[d] (s)				Run Time[e]
npts[a] (θ)	dθ[b] (km)	Npts (r)	dr (km)			*S* (40°)	*S* (80°)	*SS* (120°)	*SS* (160°)	
5000/24	4.0/2.2	1000	2.9	16894	17	16	18	25	30	19 m
10000/24	2.0/1.1	1800	1.6	33785	52	10	12	17	19	2 h 9 m
15000/24	1.3/0.7	2900	1.0	50758	122	8	10	12	15	7 h 39 m
20000/24	1.0/0.5	3800	0.76	67649	210	6	8	10	11	17 h 33 m
30000/24	0.7/0.4	5200	0.55	101512	428	5	6	8	9	2 d 6 h 21 m

[a] Values are: Total number of grid points / Number of processors used.

[b] Values are: dθ (at Earth surface) / dθ (at CMB)

[c] Memory is reported as total memory (code+data+stack size) for one processor. Code size: ~800 kb.

[d] Dominant Period based on phase and epicentral distance listed for a source depth of 500 km.

[e] Total run time is based on 2700.0s of simulation time.

Table 3.2. Example SHaxi parameters and performance – "Iceberg" Supercomputer.

Grid Size[a]		Number of Nodes[b]	Simulation Time = 1800 s		Simulation Time = 2700 s	
Npts (θ)	npts (r)		Number of Time Steps	Run Time	Number of Time Steps	Run Time
5000	1000	4	11281	13 m	16921	21 m
10000	1800	4	22560	1 h 31 m	33840	2 h 16 m
10000	1800	8	22560	57 m	33840	1 h 24 m
15000	2900	8	33838	3 h 2 m	50758	4 h 24 m
15000	2900	12	33838	2 h 20 m	50758	3 h 32 m
20000	3800	12	45099	5 h 46 m	67649	8 h 14 m
20000	3800	16	45117	4 h 30 m	67676	6 h 23 m
30000	5200	16	67675	12 h 26 m	101512	17 h 38 m

[a] Corresponding grid spacing is listed in Table 1.

[b] Each node consists of an IBM p655+ node, with 8 processors per node, and 16 Gb shared memory. Processor speed is 1.5 GHz.

Table 3.3. Simulation parameters used in SHaxi verification.

Parameter	Linear Array	Circular Array
V_S	2000 m/s	2000 m/s
Density (ρ)	2000 kg/m^3	2000 kg/m^3
dr	77.5 m	38.7 m
rdθ	48.9 m	24.4 m
T_{dom}	1.0 s	0.6 s
λ_{dom}	2000 m	1200 m
Points per wavelength	20 (radial) 40 (lateral)	
Receiver spacing	976 m	13.5°
Source-receiver distance	varies	5859 m

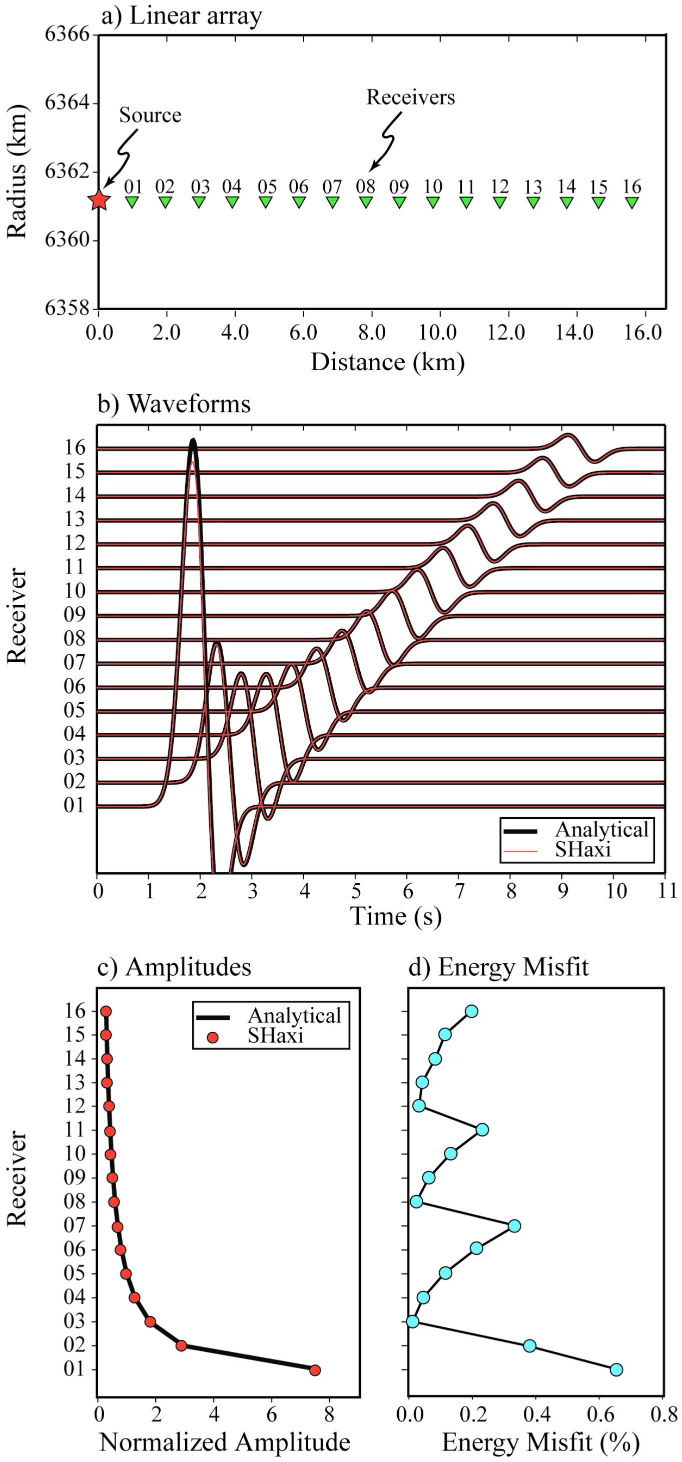

Figure 3.37: *a) Source-receiver setup of the linear array used to examine the geometrical spreading of the wave field. The receiver spacing corresponds to 0.6 dominant wavelengths (1.2 km) in the simulation. b) Numerical FD (red solid line) and analytical (black solid line) seismograms for the array. c) The maximum FD amplitudes of all traces (red filled circles) are plotted on top of the analytical curve (solid line). d) The energy misfit between the FD and analytical solutions. The misfit is below 0.8% for the entire section.*

With this linear array the propagation effects and the spreading for a constant take off angle and varying source receiver distance can be investigated. Table 3.3 lists the simulation parameters for the two setups. Figure 3.6 shows the results for the circular array. In Figure 3.6b the computed seismograms (red) together with the analytical traces (black) are displayed. To make the difference between both solutions apparent, the topmost trace shows the difference trace for receiver no. 8 scaled by a factor of 25. Figure 3.6c shows the radiation pattern for all computed traces (marked with red circles) together with the analytical curve $f(\gamma) = \sin(\gamma)$, with γ the take off angle, plotted with solid lines. The SHaxi radiation pattern is calculated from the maximum amplitudes of the individual seismogram traces.

Figure 3.6d shows the energy misfit between the SHaxi solution and Eq. 4. The energy misfit is well below 0.4% and depends on the take off angle. For steep angles the accuracy of the solution decreases. This behavior is caused by the boundary condition for the symmetry axis which works best for take off angles perpendicular to the axis.

In Figure 3.7b the numerical (red) and analytical (black) seismograms for the linear array are shown. In Fig. 7c the geometrical spreading of both solutions are shown similar to Fig. 6c. The analytical function is $f(r) \sim 1/r$ with r: source-receiver distance. The bottom right figure shows the energy misfit for the linear array. Except for receiver 1 the energy misfit is below 0.4%. The increased energy misfit for locations very close to the source is a numerical effect caused by the grid discretization. This effect occurs for source-receiver distances closer than one dominant wavelength which should be avoided to achieve an acceptable misfit.

In summary, the method is capable of computing the far field portion a strike-slip source in the nodal plane for *P* radiation. Thus, for teleseismic investigations where the wave field travels many dominant wavelengths to the receiver SHaxi provides correct seismograms. In the next Section we will show an SHaxi application which illustrates the potential of this method.

3.5 Application: scattering from the whole mantle

One field which illustrates the potential of the SHaxi method is the application to whole mantle scattering. The corresponding section from Jahnke et al. (2008) is not included in original form since this work is mainly a contribution of coauthor Mike Thorne. Instead, selected Figures from this section are presented below, together with a discussion which is original to this dissertation.

3.5.1 Influence of axi-symmetry on the scattered wavefield

A central problem for the interpretation of axi-symmetric scattering models is how parameters such as perturbation amplitude and correlation length of the axi-symmetric model can be transferred to corresponding 3D perturbations of the Earth's mantle which would cause the same effects in seismograms.

Unfortunately, no numerical comparison of 3D versus axi-symmetric scattering models has been performed yet. Such a study would require extremely high computational resources in order to generate synthetics for full 3D geometries at the dominant periods of interest and is beyond the scope of this study. Nevertheless, the insights would be highly valuable, e.g. for the calibration of other scattering simulation methods by comparison with the SHaxi method. A candidate method for such a study is the spectral-element method (Komatitsch & Tromp, 1999). Stochastical approaches like the multi-phonon method (Shearer & Earle, 2004) may provide a more realistically obtainable comparison. Alternatively, we discuss here the expected influence of axi-symmetry on the seismic wavefield from plausibility considerations and by comparison with comparable studies:

For models with no variations perpendicular to the great circle plane, axi-symmetric and 3D modelling provide the same results. However, for the Earth's mantle a locally varying, arbitrary oriented structure is plausible which is impossible to parameterize using an axi-symmetric system. Instead, axi-symmetric stochastical models are invariant in out-of-plane direction, resulting in model variations which are actually ring shaped with the center at the symmetry axis.
This geometry causes two significant competing effects on the coda of the seismograms: (1) scattered energy can not get lost by radiation off the great circle plane which leads to an enhanced contribution to the scattering amplitudes. In opposition to this effect, (2) in 3D random media the initial wavefront will encounter more possible scatterers than in 2D and thus contributions from off-plane scattering to the seismogram coda are missing in the axi-symmetric case, which causes a reduction of the scattering amplitudes. It is unclear which of these two effects is dominant and so far, no study has been made that has quantified the two effects for 2D v. 3D geometries on the shape and characteristics of the coda wavetrain.

For a precise understanding of these effects the aforementioned 3D calculations have to be performed. However, results from Frenje & Juhlin (2000) provide indications that the influence on the scattering coda is negligible. Frenje & Juhlin compared Cartesian 2D and 3D finite-difference simulations with single scattering theory. They found no significant differences between 2D and 3D simulations when measuring scattering attenuation, except that 2D simulations provide less stable results of the derived parameters.

This increased instability of 2D simulations is caused by the stronger influence of the specific model realization for a given set of model parameters: The off-plane model variations in the 3D case average out the effects of the specific model realization on the scattering coda, whose properties depend mainly on perturbation amplitude and correlation length. For 2D simulations this averaging process does not exist. However, stable model parameters can be derived by averaging the results of multiple realizations of a set of model parameters.

3.5.2 Simulations of whole mantle scattering

Modelling small scale scattering in the whole mantle is still a challenge if realistic wavelengths are concerned. Several studies show that prominent S wave scattering occurs throughout the whole mantle for correlation lengths of the seismic parameters down to roughly 8 km (Hedlin et al., 1997). In the lithosphere even shorter correlation lengths down to 5 km are expected (e.g., Saito *et al.* 2003).

Figure 3.8 shows one of the scattering models investigated in Jahnke et al. (2008). For the model generation a Gaussian autocorrelation function was used with a correlation length of 32 km. The applied velocity perturbation has a RMS value of 1% and maximum values of +/- 3%. More details about the model and the simulations discussed below are provided in the publication. The method used for the model generation is basically to first generate a matrix of random numbers and then to perform a 2D convolution of this matrix with the selected Gaussian autocorrelation function. This is an elegant method for Cartesian model discretizations.

However, for the spherical coordinate system used in SHaxi this method would generate artificial lateral anisotrophy, since the lateral grid spacing at the bottom of the model corresponds to approximately half the grid spacing at the surface. To avoid this, the model was first calculated on a highly refined Cartesian grid. In a second step, an interpolation to the coarser polar SHaxi grid was performed. This method is somewhat unsatisfactory, since the generation of the highly oversampled Cartesian grid efforts computational resources which easily exceed those of present workstations. Moreover, if the chosen oversampling is too low, artificial anisotropy may occur in the lowermost model region where the spherical grid is most dense. An interesting approach for an elegant, computational much cheaper way to generate stochastical models for arbitrary grids is found by Thorne et al. (2008, in preparation) using the Karhunen-Loève transform.

A snapshot of the wave field after 300 s for a similar model is shown in Figure 3.9, right. The model has the same correlation length but an increased velocity perturbation of 3% RMS. For comparison, the corresponding wave propagation snapshot for a pure PREM model is shown on the left. In both snapshots, the direct S wave and the surface reflection sS are clearly visible. For the PREM model additional weak wavefronts originating from conversions of the mantle discontinuities are visible. For the perturbed model the snapshot also shows a significant amount of scattered energy.

Another effect which is visible in the snapshot of the perturbed model is that the back-scattered wave field near the symmetry axis seems to be enhanced. The explanation for this effect is that the scatterers are also axi-symmetric and focus the back-reflected part of the wave field towards the symmetry axis which acts as a focal line. This is a general problem of axi-symmetric methods for setups were a significant amount of energy is reflected back towards the axis for receivers which are located closer to the axis than the back-reflecting structures. For such cases, the contribution of the back-reflected energy to the recorded seismogram would be over empathized compared to a back-reflecting structure with no focusing shape. However, for most setups of interest, this effect is no serious restriction.

Figure 3.10 shows a seismogram comparison for a pure PREM model and a scattering model with Gaussian autocorrelation function having an correlation length of 16 km and a velocity perturbation of 3% RMS. The epicentral distance is 75°. In order to show the frequency dependence of the scattering effects the seismograms are filtered to dominant periods between 4 s and 20 s. The strongest scattering effects occur for the shortest dominant period of 4 s.

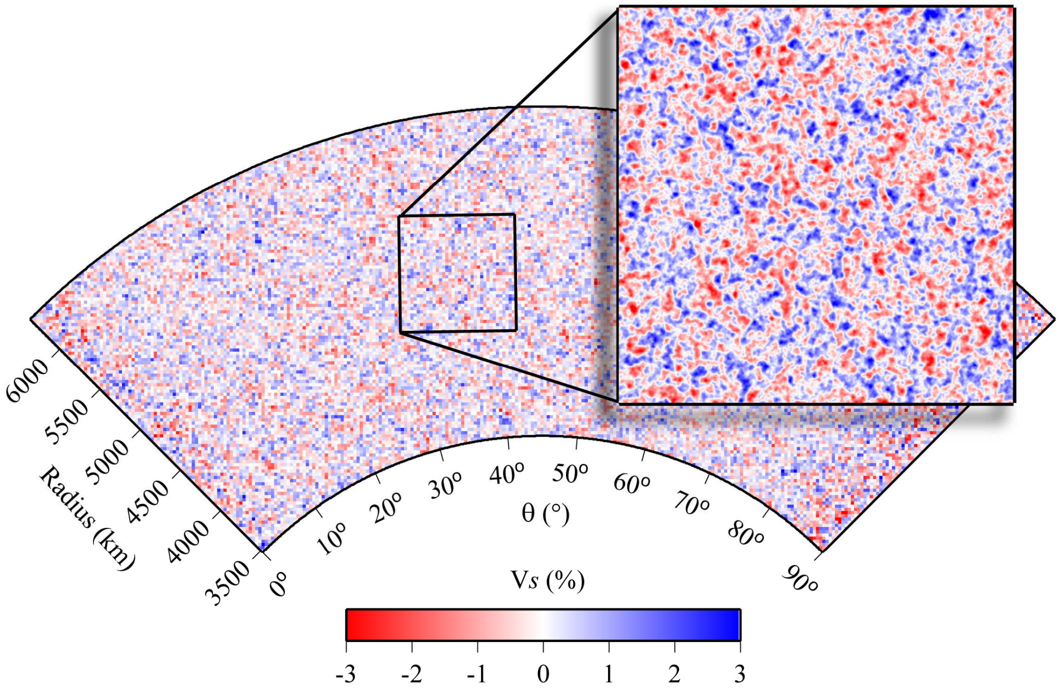

Figure 3.38: *Model of the mantle based on of PREM with additional random velocity variations. For the model generation a Gaussian autocorrelation function with correlation length of 32 km was used. A detailed description can be found in Jahnke et al. (2008).*

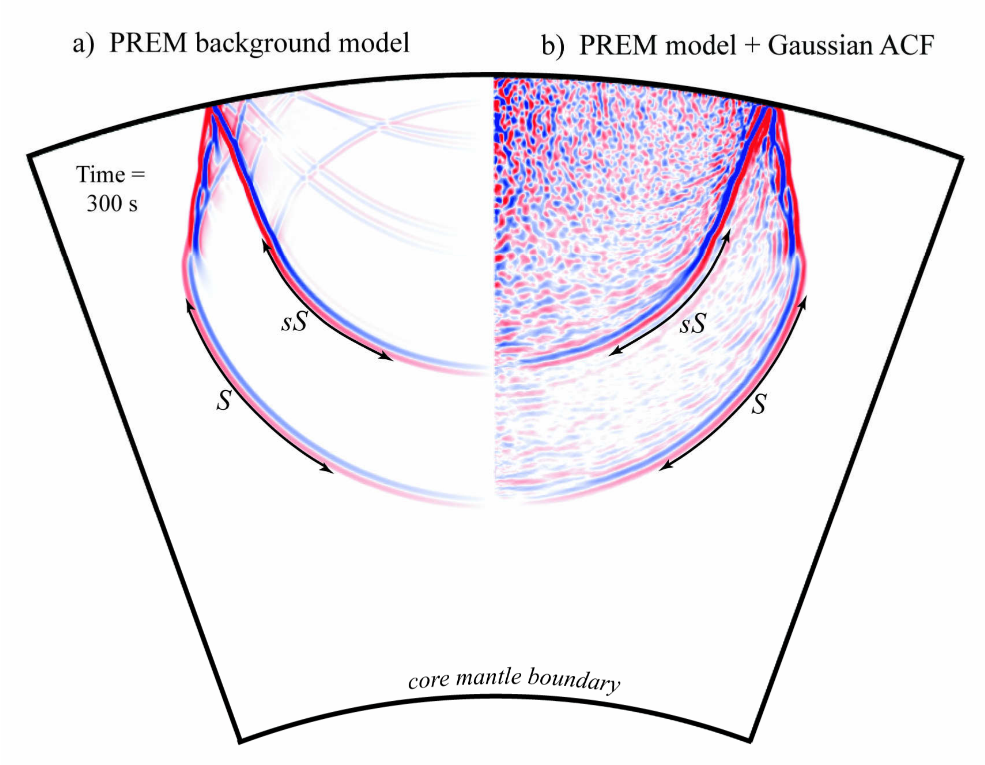
a) PREM background model
b) PREM model + Gaussian ACF
Time =
300 s
sS
S
sS
S
core mantle boundary

Figure 3.39: *SH wave propagation after 300 s for a source depth of 200 km. a: unperturbed PREM model, b: PREM model with additional random velocity perturbation generated with a Gaussian autocorrelation function with 32 km wavelength, similar to the model shown in Figure 3.8.*

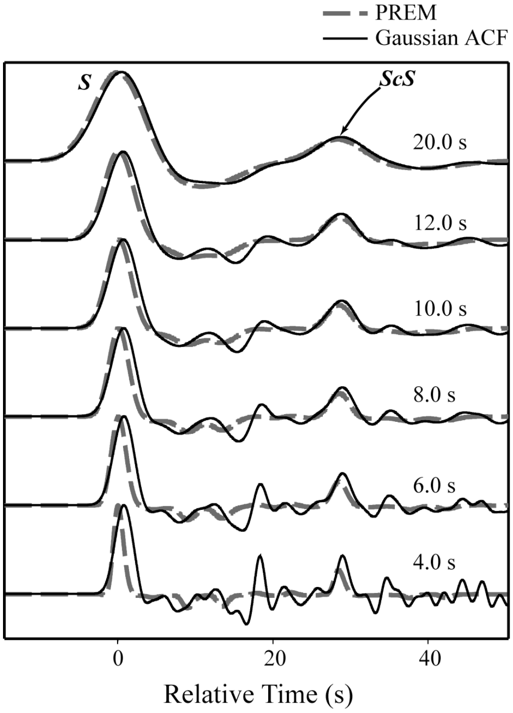

Figure ***3.310:*** *Seismograms filtered to dominant periods between 4 s and 20 s for (1) the unperturbed PREM model (dashed lines) in comparison with (2) a model with additional random perturbations with 16 km correlation length.*

3.6 Discussion and conclusions

In this paper, we presented a method to calculate high-frequency global *SH* seismograms for axi-symmetric geometries. Axi-symmetric methods fill the gap between 1D methods which are often too limited to explain teleseismic observations and full 3D methods, which require very high computational resources. On teleseismic scales the major portion of the wave field propagates in the great circle plane. As a consequence, out of plane variations of the seismic properties can often be ignored. Although the computational effort of SHaxi is equivalent to 2D methods the correct 3D geometrical spreading is preserved in contrast to traditional 2D methods. The applied ring-source in SHaxi is equivalent to a vertical strike-slip source for source-receiver distances larger than about five dominant wavelengths where the near and intermediate wave fields vanish. Although arbitrary sources cannot be modeled and comparisons with real seismograms can not be directly made, the method can be used to probe many teleseismic questions. The method is especially suited to investigating relative amplitudes and/or travel-times. Moreover when the take-off angle of the investigated phases is known, amplitude correction terms can be calculated. The reduction of computational effort has permitted exploration of teleseismic waveforms at frequencies where whole mantle scattering may come into play. For example, determination of the length scales and spatial location of small scale seismic heterogeneity may provide important geodynamic implications, such as the degree of convective mixing in the mantle or compositional heterogeneity (e.g., van der Hilst & Kárason 1999; Davies 2002). Fixing the spatial extent of small scale heterogeneity in the mantle may be challenging, however techniques focused on measuring differential attenuation may prove useful. A companion paper (Thorne *et al.* 2007) uses SHaxi to examine the high frequency wave form effects of recent data analyses for D" discontinuity structure beneath the Cocos Plate region. As investigations of whole mantle scattering become more and more prominent, numerical techniques such as SHaxi that are capable of synthesizing waveforms with the inclusion of scattering will become important, as they have for regional scale modelling.

Acknowledgements

G. Jahnke was supported by the German Research Foundation (DFG, Project Ig16/2). M. Thorne was partially supported by NSF grant EAR-0135119 and the International Quality Network: Georisk funded by the German Academic Exchange Service. We thank the Arctic Region Supercomputing Center of the University of Alaska Fairbanks and the Leibniz Rechenzentrum Munich for access to their computational facilities. We also acknowledge support from the European Human Resources Mobility Program (SPICE Project) for travel support and for hosting the SHaxi code (www.spice-rtn.org).

3.7 Studies using the SHaxi code

So far, three studies exist which use the SHaxi program for different purposes, ranging from the analysis of lower mantle anomalies and deduction of absolute temperatures, phenomenological studies on the effects of plume-mantle interaction on the seismic wavefield and analysis of the potentials and limitations of existing local D” models to explain teleseismic data. The following section gives an overview about these studies.

3.7.1 Phase transitions in D” region beneath the central Pacific

Lay at al. (2006) derived the structure of the D” region beneath the central Pacific Ocean from S-wave velocity variations in the lowermost mantle. Using SHaxi simulations they were able to take topography effects into account for the estimation of the seismic parameters in the investigated region.

They derived a geodynamic model and temperature gradients of the study region, as well as constraints about the *absolute* temperature in the lowermost mantle, indicating ~2500 K at 2700 km depth. In general, the absolute temperature at depth is a barely known parameter in the Earth’s interior and can be derived only at depths where phase transitions occur, such as the 410-km, 660-km discontinuity or the inner core boundary. Generally, in the lowermost mantle, uncertainties of the absolute temperature in the order of ±500 K exist. Lay et al. (2006) found a rapid S-velocity increase on top of a rapid decrease which they interpreted as a post-perovskite lens embedded in perovskite material, several hundred kilometres above the core mantle boundary.

To be able to derive the S-wave velocity contrasts they calculated relative amplitudes of ScS with respect to the direct S wave from data and synthetics, using a double-array stacking technique. The dataset consists of intermediate- and deep-focus Tonga-Fiji earthquakes recorded in California. By comparing 1D modelling results with SHaxi models including topography they found that plausible velocity contrasts tend to be 50 to 100% higher if lateral variations of the corresponding discontinuities are taken into account.

3.7.2 Upper mantle discontinuities beneath the Hawaiian hotspot

Schmerr et al. (2003) investigated the properties of the 410- and 660-km discontinuities beneath the Hawaiian hotspot using stacked seismic precursors of the SS phase. The precursors are generated by underside reflections at the discontinuities (S660S and S410S, respectively) which result from phase changes of the mantle mineral at the corresponding depths. In their study, they compare the precursors with the SS phase concerning relative travel time and amplitude, from which depth, topography and sharpness of the discontinuities can be derived. Previous studies found a thinning of the transition zone in the investigated region (e.g. Li et al., 2003). This thinning is generally explained by upwelling of hot material of the Hawaiian mantle plume which affects the depth of the mineral phase transitions of the 410- and 660-km discontinuities.

In order to investigate the effects of such topography on the S410S and S660S precursors, they performed modelling of a Gaussian shaped depression of the transition zone using the SHaxi code for dominant periods of ~10 sec. As a general feature, relatively strong defocusing of the S660S phase was found for reflection points near the edge of the model topography, whereas the defocusing was moderate for the S410S phase. This effect is expected to reduce the detectability of precursors of the SS phase if they are generated at a discontinuity with significant topography.

3.8 Lateral variations of the D” region beneath the Cocos Plate

In a study by Thorne, Lay, Garnero, Jahnke and Igel (2007) the structure of the lower mantle beneath the Cocos plate, west of Central America was investigated, using a data set of South American earthquakes recorded at networks in California. A focus of the study was set on verifying with SHaxi generated synthetics how well existing lower mantle models derived by different data analysis procedures are actually able to explain the observations.

For the selected data set, the ScS bounce points at the core-mantle boundary lie in the study area beneath the Cocos plate. For signal enhancement and stabilization a double-array stacking technique was applied to the data. The resulting beams were compared to SHaxi synthetics at a dominant period of 4 sec for three different model types from recent data analyses: (1) a plain D” reflector 264 km above the core-mantle boundary with an S-wave velocity increase of 0.9-2.6%, derived from local 1D models of Lay *et al.* (2004), (2) an undulating D” reflector with an increase in discontinuity height from 150 km to 300 km based on Thomas *et al.* (2004) and (3) cross sections through the 3D tomography model of Grand (2002).

In the covered distance range between 70° and 85° the time window of interest lies between the direct S arrival and the ScS arrival which reflects at the core-mantle boundary. For high velocity D” regions an additional phase SdS is expected in between the S and the ScS phase, actually consisting of a combination of the reflection on top of the D” layer which interferes with the refracted wave turning inside the D” layer.

The modelling results for all three model types differ significantly in waveform shape and travel times. Moreover, none of the investigated models was able to sufficiently explain the observed data. A proposed explanation for the failure of such methods is that the definition of local 1D models is largely biased by small scale structure of the order of the dominant wavelengths of the seismic wavefield. The cross section tomography model has the drawback that tomography models generally do not reproduce realistic velocity contrasts, which have significant effects on the waveform for the investigated dominant periods.

Chapter 4:

Global axi-symmetric P-SV wave propagation

4.1 Introduction

A code for P-SV wave propagation in spherical coordinates (PSVaxi) was developed for calculating the axi-symmetric P-SV part of the wave field in virtually the whole sphere, analogously to the SH case described in chapter 3. The algorithm is based on the work of Igel & Weber (1996) who implemented a high-order staggered-grid finite-difference scheme for P-SV wave propagation on a single uniform grid spanning the r-θ plane, comparable to the single grid used in the SHaxi program. In general, the usage of a single uniform grid and polar coordinates in a finite difference scheme limits the maximum achievable model depth, since the spacing of each grid cell in lateral direction is proportional to its distance from the Earth's center. This causes numerical instability if the variation of the lateral grid spacing becomes too large.

For the SHaxi algorithm this maximum depth restriction which comes along with the used single uniform grid does not affect the stability of the scheme: SH waves totally reflect at the CMB which is located approximately halfway from the Earth's center. Thus the CMB acts as a natural model boundary and it is sufficient to discretize solely the mantle region. This leads to a maximum lateral variation of the grid spacing of approximately 2 which is well inside the stable regime.

However, the P-SV wave field in the Earth's mantle is capable of generating P-waves also in the liquid outer core and, in addition to that, P-SV waves in the solid inner core which pass the Earth's center. Despite the long propagation distances of such phases, they are capable of generating prominent seismic signals at the surface and thus must be accurately modelled in order to obtain complete global seismograms. Such signals are, for example, the PKP and SKS phases which turn in the outer core region, or PKIKP which travels through the inner core.

The PSVaxi algorithm overcomes the aforementioned depth restriction by using an arbitrary number of grids (domains), each discretizing a certain depth range, instead of using one single grid for the whole model space: Whenever the decrease of the lateral grid spacing with depth accumulates a factor of ½ a new grid with doubled angular grid spacing is created spanning the subsequent depth interval. This procedure is iterated as many times as necessary to enlarge the model space practically down to the Earth's center. Actually, this *multi domain* technique leaves out a small region around the Earth's center and the lowermost grid points of the model have to be tapered in order to avoid artificial reflections from the bottom of the lowermost grid. It turns out that in practice, the small whole in the model space does not significantly bias the seismograms, due to wave front healing which occurs while the wave travels from the Earth's center to the surface.

4.2 Formulation of the P-SV wave equation

The elastic wave equation for axi-symmetric geometries can be derived from the general 3D velocity stress formulation of the elastic wave equation in spherical coordinates (e.g. Igel, 1999). The coordinate system used for the PSVaxi algorithm corresponds to the system used for the SHaxi algorithm (Figure 3.1). The relevant differential equations for pure P-SV wave generation and invariance in φ-direction are:

$$
\begin{aligned}
\rho\partial_t v_\mathrm{r} &= \partial_\mathrm{r}\sigma_\mathrm{rr} + \frac{1}{r}\partial_\theta\sigma_{\mathrm{r}\theta} + \frac{1}{r}(2\sigma_\mathrm{rr} - \sigma_{\theta\theta} + \sigma_{\mathrm{r}\theta}\cot\theta) + f_\mathrm{r} \\
\rho\partial_t v_\theta &= \partial_\mathrm{r}\sigma_{\mathrm{r}\theta} + \frac{1}{r}\partial_\theta\sigma_{\mathrm{r}\theta} + \frac{1}{r}[(\sigma_{\theta\theta} - \sigma_{\varphi\varphi})\cot\theta + 3\sigma_{\mathrm{r}\theta}] + f_\theta \\
\partial_t\varepsilon_\mathrm{rr} &= \partial_\mathrm{r} v_\mathrm{r} \\
\partial_t\varepsilon_{\theta\theta} &= \frac{1}{r}\partial_\theta v_\theta + \frac{1}{r}v_\mathrm{r} \\
\partial_t\varepsilon_{\varphi\varphi} &= \frac{1}{r}v_\mathrm{r} + \frac{\cot\theta}{r}v_\theta \\
\partial_t\varepsilon_{\mathrm{r}\theta} &= \frac{1}{2}\left(\frac{1}{r}\partial_\theta v_\mathrm{r} + \partial_\mathrm{r} v_\theta - \frac{1}{r}v_\theta\right),
\end{aligned}
\tag{9}
$$

with: σ_{ij}: stress tensor, v_r, v_θ: velocity, f_r, f_θ: external force, ε_{ij}: strain tensor, and ρ: density.

Analogous to the finite difference methods described in chapters 2 and 3 the axi-symmetric P-SV wave equation is implemented on staggered grids in order to improve the numerical accuracy of the scheme (Virieux, 1984, 1986). The transformation of the differential form of the wave equation of Eq. 9 to a finite difference formulation which takes into account the individual positions of the seismic properties on the staggered grids (Fig. 4.1) requires to introduce both, forward- and backward derivative- and interpolation operators. The corresponding finite difference form of Eq. 9 is:

$$
\begin{aligned}
\rho\partial_t v_\mathrm{r} &= \partial_\mathrm{r}^-\sigma_\mathrm{rr} + \frac{1}{r}\partial_\theta^+\sigma_{\mathrm{r}\theta} + \frac{1}{r}(2[\sigma_\mathrm{rr}]^{-z} - [\sigma_{\theta\theta}]^{-z} + [\sigma_{\mathrm{r}\theta}]^{-z}\cot\theta) + f_\mathrm{r} \\
\rho\partial_t v_\theta &= \partial_\mathrm{r}^+\sigma_{\mathrm{r}\theta} + \frac{1}{r}\partial_\theta^-\sigma_{\mathrm{r}\theta} + \frac{1}{r}(([\sigma_{\theta\theta}]^{-x} - [\sigma_{\varphi\varphi}]^{-x})\cot\theta + 3[\sigma_{\mathrm{r}\theta}]^{+z}) + f_\theta \\
\partial_t\varepsilon_\mathrm{rr} &= \partial_\mathrm{r}^+ v_\mathrm{r} \\
\partial_t\varepsilon_{\theta\theta} &= \frac{1}{r}\partial_\theta^+ v_\theta + \frac{1}{r}[v_\mathrm{r}]^{+z} \\
\partial_t\varepsilon_{\varphi\varphi} &= \frac{1}{r}[v_\mathrm{r}]^{+z} + \frac{\cot\theta}{r}[v_\theta]^{+x} \\
\partial_t\varepsilon_{\mathrm{r}\theta} &= \frac{1}{2}\left(\frac{1}{r}\partial_\theta^- v_\mathrm{r} + \partial_\mathrm{r}^- v_\theta - \frac{1}{r}[v_\theta]^{-z}\right),
\end{aligned}
\tag{10}
$$

with: $\partial_\theta^+, \partial_\theta^-, \partial_r^+$ and ∂_r^-: the forward (+) and backward (-) derivative operator in horizontal (θ) and vertical (r) direction, and $[]^{+x}, []^{-x}$, $[]^{+z}$ and $[]^{-z}$: the corresponding forward (+) and backward (-) interpolation operators in vertical (z) and horizontal (x) direction.

Before the individual terms in Eq. 10 can be calculated several wave field parameters have to be interpolated at the particular positions where they are needed.

In addition to these interpolations, the aforementioned multi domain discretization requires *additional* interpolations at the domain boundaries in order to implement the wavefield transition across adjacent domains. The next section describes how these additional interpolations are performed.

4.3 Staggered grid scheme

In Figure 4.1, a cutout of the velocity (u_θ ,u_r) and stress (σ_{ii}, $\sigma_{r\theta}$) grids which are used in Eq. 10 is shown for a small region close to the symmetry axis, at the boundary of two adjacent domains.

As can be seen in the Figure, it is possible to calculate vertical derivatives and interpolations for u_θ and σ_{ii} across the two domains using standard finite difference operators: Since the horizontal positions of the u_θ and σ_{ii} grids are identical, each column in the coarser grid has a counterpart column in the finer grid which is located at the same horizontal position.

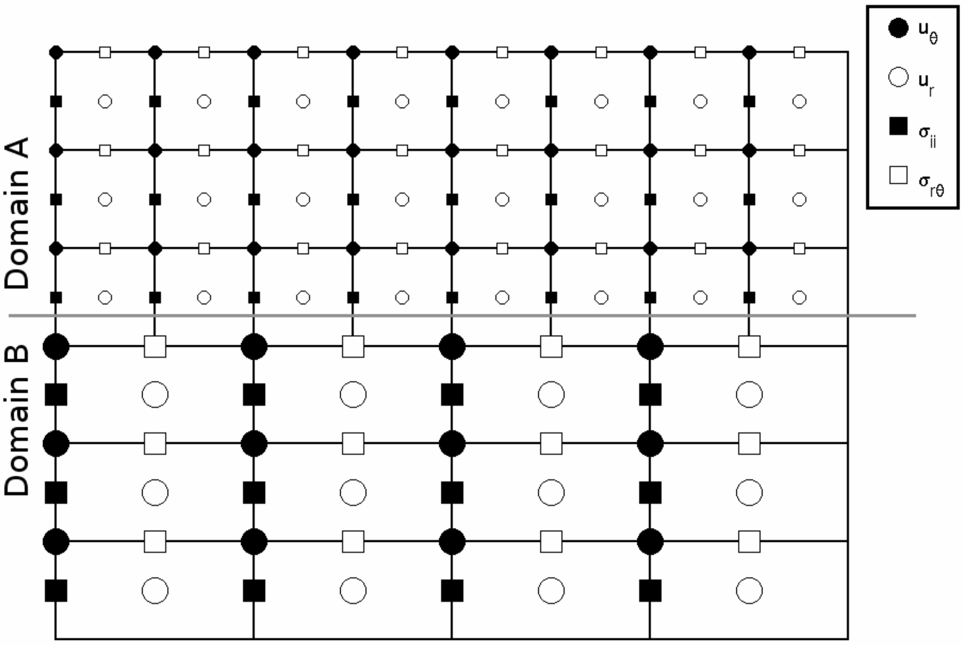

Figure 4.1: *Cutout of the staggered grids at the boundary of two domains for velocities (*u_θ ,u_r*) and stresses (*σ_{ii}, $\sigma_{r\theta}$*). Each rectangle denotes a unit grid cell with its relevant seismic properties marked by circles and squares.*

The corresponding interpolation in vertical direction of u_θ by the operator $[]^{-z}$ is illustrated in Figure 4.2 where black circles denote the location of the u_θ gridpoints and red circles correspond to the interpolated u_θ values. The interpolated grid is shifted vertically *upwards* by ½ grid spacing with respect to the originating u_θ grid, which reflects the behavior of the $[u_\theta]^{-z}$ interpolation. The horizontal row of interpolated values which is located in between the two domains is calculated by combining every second grid point of the finer domain with the appropriate grid point of the coarser domain, as indicated in the Figure. The vertical green lines in the Figure illustrate the interpolation of exemplary points which are located well inside the domains and at the boundary between the domains, respectively. Since σ_{ii} is defined on the same locations as u_θ the corresponding scheme is identical and not explicitly shown here.

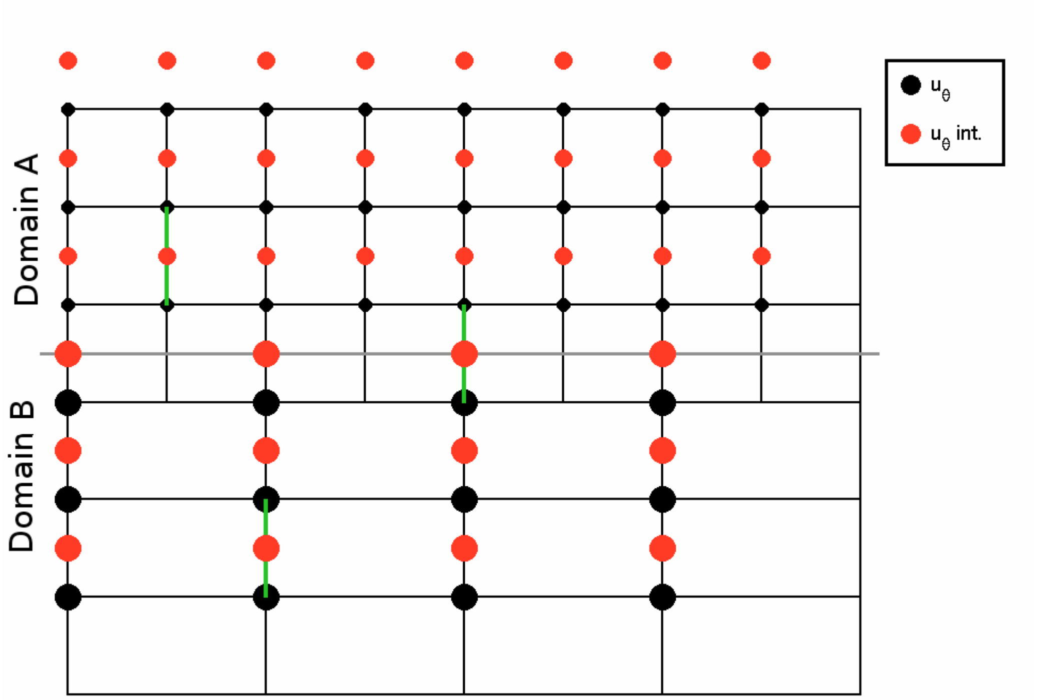

Figure 4.2: *Same cutout as shown in Figure 4.1, focussing on the u_θ discretization. In addition to the regular u_θ grid (black circles) an additional grid with interpolated u_θ values is defined (red circles). Well inside the domains the interpolation is performed using neighboring grid points as indicated by two vertical green lines. The uppermost interpolated row of domain B which lies at the boundary of the two domains incorporates values from domain A, as indicated by the green line.*

A close inspection of Figure 4.1 shows that for u_r and $\sigma_{r\theta}$ the abovementioned procedure can not be applied, since the horizontal positions of the gridpoints in domain A and B have an offset. Instead, before vertical derivatives of u_r across the domain boundary can be calculated, a horizontal interpolation of the uppermost row of the coarser grid has to be performed, as shown in Figure 4.3:

Here, the interpolated u_r grid is shifted vertically *downwards* by ½ grid spacing with respect to the originating u_r grid, which reflects the behavior of the $[u_r]^{+z}$ interpolation.

Inside the domains the vertical interpolation is again performed using neighboring grid points as indicated by the two *vertical* green lines drawn well inside the domains A and B.

For interpolation gridpoints *between* two domains the applied scheme is different: Since the horizontal positions of u_r in domain B show an offset with respect to the positions in domain A, an additional horizontal interpolation of the uppermost gridpoints of domain B has to be performed as indicated by the green *horizontal* lines and green circles.

For the gridpoint closest to the symmetry axis this interpolation has to be performed in a slightly different way than for the gridpoints located off the axis, which is illustrated by the green L-shaped and U-shaped schemes.

After this additional horizontal interpolation is performed, interpolated u_r values exist at the positions (green circles) where they are needed for the intended *vertical* interpolation across the domains. The interpolation of $\sigma_{r\theta}$ works identical to the one of u_r and is not explicitly discussed here.

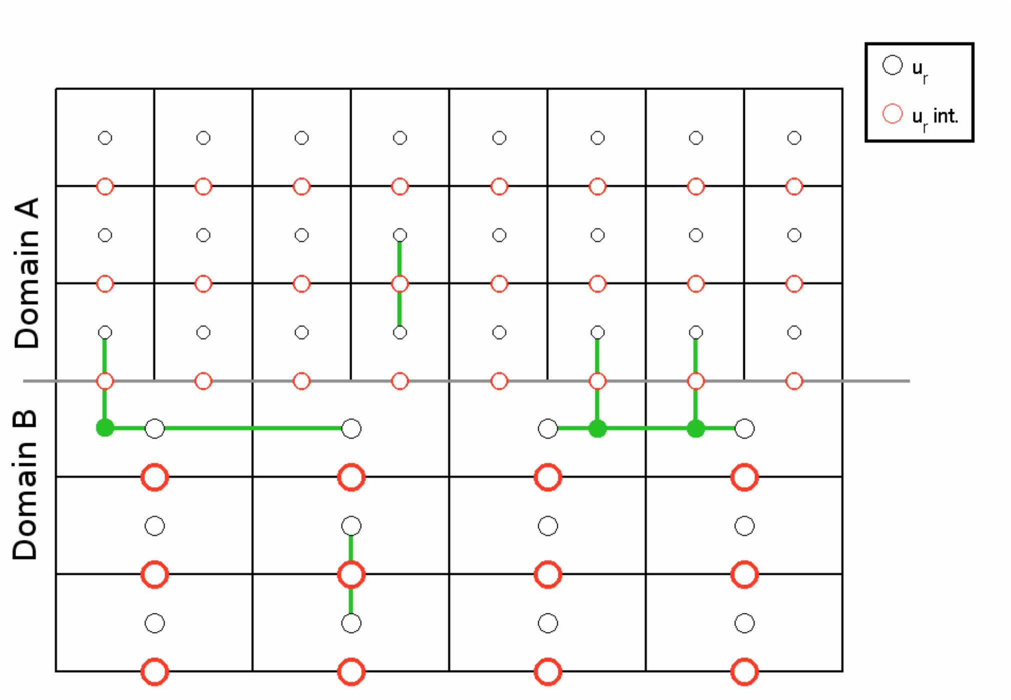

Figure 4.3: *Same cutout as in Figure 4.1, focussing on the u_r discretization. In addition to the regular u_r grid (black open circles) an additional interpolated u_r grid is defined (red open circles). The lowermost interpolated row of domain A incorporates additional interpolated values from domain B (green circles and horizontal lines).*

4.4 Multi domain decomposition

The decomposition of the model space into several uniform grids (domains) is exemplarily illustrated in Figure 4.4 for a total number of five domains. The uppermost domain spawns the depth interval from the surface to ½ the Earth's radius, the second domain from ½ to ¼ the Earth's radius, etc. Due to the spherical geometry, this causes the uppermost row of each grid to have two times the *lateral* grid spacing (*rdθ*), and the same *radial* grid spacing (*dr*) of to the lowermost row in the same grid. To compensate this, the *angular* grid spacing (*dθ*) of each underlying grid is now reduced by a factor of two with respect to the adjacent upper grid. This compensates for the decrease of the lateral grid size due to the shrinking radius. Since both the lateral and radial grid spacing increases by a factor of 2, the number of grid points in each domain corresponds to approximately ¼ of the adjacent upper grid.

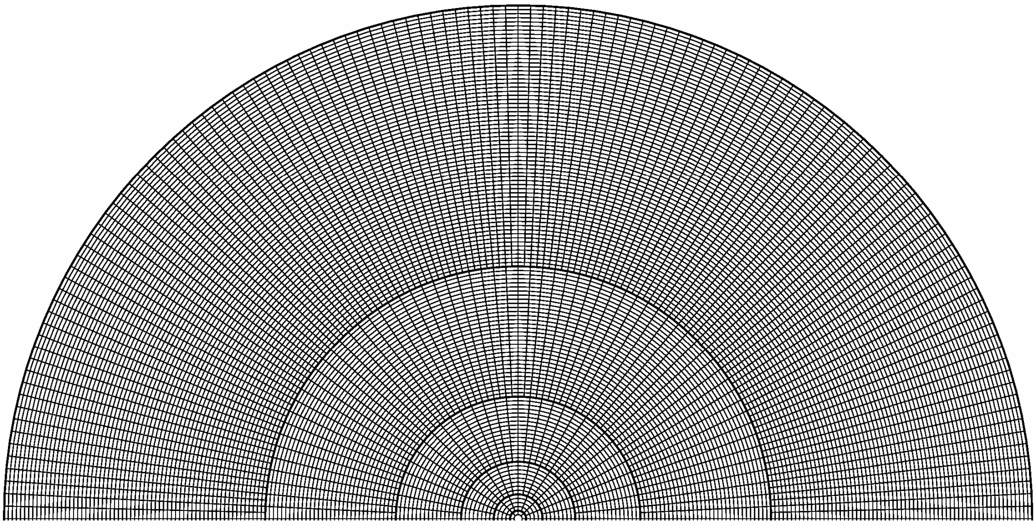

Figure 4.4: *Principle of multi domain decomposition of the model space, here shown for five domains which are outlined by thick lines. The symmetry axis is aligned horizontally and each of the small elements corresponds to an unit grid cell. For simplicity, the staggering of the seismic parameters is not shown here. A small region around the Earth's center can not be discretized by this scheme and has to be tapered to avoid artificial reflections.*

In principal, other multi domain schemes performing the necessary regridding at other depth intervals are also thinkable. As an advantage, the usage of a higher number of domains per depth interval would somewhat increase the accuracy and performance, since the overall variation of the lateral grid spacing of the individual domains would be decreased. However, for such schemes the necessary interpolation across the boundaries for the calculation of the vertical derivatives would be more complicated to implement, due to the practical consequences which an angular grid reducing factor other than 2 would have for the implementation. Moreover, since the expected performance increase will be marginal, the simpler approach was chosen for the domain decomposition.

4.5 Parallelization

For the use of the PSVaxi method on distributed memory computers a distribution of the model space among the individual nodes of such systems was implemented. A special subdividing scheme was developed to assure that approximately the same number of grid points is stored and processed by each node. This equal distribution is important in order to assure efficient load balancing so that both the memory and processor time of each computing node is fully utilized.

The scheme implemented in the PSVaxi algorithm demands that the total number of nodes must be equal to 2^n with n=1-6. Thus, simulations using 2,4,8,16,32 and 64 nodes can be performed, which enables to model dominant periods down to 1 s on actual high performance parallel computers.
As a first step, in order to divide the whole model space in two segments with approximately the same number of grid points it is helpful to derive an approximation for the ratio of grid points in the topmost domain to be sliced versus the sum of all grid points contained in all underlying domains. Assuming that a significant number of underlying domains exist, the total number of grid points in these domains can be approximated by:

$$\sum_{i=2}^{L} N_i = \frac{1}{4^1} N_1 + \frac{1}{4^2} N_1 + \ldots + \frac{1}{4^{L-1}} N_1$$

$$= \frac{\mathrm{N}_1}{4} \sum_{i=1}^{L-1} \frac{1}{4^i} \cong \frac{1}{3} N_1 \ , \qquad (6)$$

with $N_{i:}$: the number of grid points in domain i, and L: the total number of domains used for the model discretization.

Thus, the number of grid points of the topmost domain 1 corresponds to approximately 3 times the total number of grid points of all underlying domains (2-L). Although Eq. 6 is exact only for $L=\infty$ and grids of infinite size, the relation can be used also for finite L (e.g. $L=10$) for this subdivision scheme since it provides a satisfactory load balancing during a parallel calculation.

This scheme, which will be explained in detail below, is illustrated in Figure 4.5. The figure shows schematically how the model space is distributed to the individual nodes. On the left of Figure 4.5 the model space in horizontal (θ) and vertical (r) direction is displayed as a stack of coloured rectangles. Each rectangle denotes a domain which is created by the domain decomposition process already explained in section 4.1.4 and which basically consists of a uniform staggered grid storing the seismic parameters. The vertical size of each rectangle in the Figure is proportional to the number of grid points in vertical direction and also proportional to the depth extension covered by the corresponding domain. Since the vertical extension of each domain corresponds to ½ times the extension of the adjacent upper domain, the rectangles become thinner with increasing domain index. On the right of Figure 4.5, six grey columns are shown, each corresponding to one possible total number of nodes for a parallel run, ranging from 2 to 64.

For simplicity, the applied scheme will now be explained for parallelization on 2 and 4 nodes only, which affects solely the topmost domain. The same procedure can be applied iteratively to subsequent domains for higher grades of parallelization, as will be shown:

- Two nodes:
  This case is shown by the rightmost column on the right of Figure 4.5: For vertically splitting the model space in two segments of approximately equal size, the first node claims the upper 2/3 of domain *1*, whereas the second node is responsible for the remaining 1/3 of domain *1* and for all underlying domains *2-L* which contribute with approximately another 1/3 to the total number of grid points, as shown in Eq. 6.

- Four nodes:
  Each of the two segments we got for the case of two nodes explained above, can now be subdivided in two new segments of approximately equal size. To fulfil the requirement of equal size of the individual segments, the first domain has to be split into three segments which are processed by the nodes 1-3.[1] The underlying domains are processed by node 4, as illustrated in Figure 4.6.

- More than four nodes:
  For progressing to higher orders of parallelization, the segments which would cover domain 1 after applying a two-node parallelization are iteratively cut into halves as often as necessary. In addition, for a parallelization on 8 and 32 nodes it is necessary to apply the steps described for two and four nodes also to domain *2* and *3*, respectively, as is shown by the corresponding columns on the right of Figure 4.5.

In principal, this scheme can be expanded to unlimited numbers of nodes to be able to perform simulations on more than 64 nodes. Moreover, the limitation of the total number of nodes being powers of two is not mandatory. However, since the implemented scheme covers the dominant periods of interest of most teleseismic studies on body waves, and since job queues on present supercomputers in most cases demand a total number of nodes which is a power of two these limitations have practically no effect on the flexibility of the code.

---

[1] Actually, the implemented scheme differs slightly from this description: For a simpler implementation it is assured that the boundaries of domains and segments are never located at the same depth index. Instead, the topmost segment of the second domain is a little enlarged to incorporate also the lowermost few lines of gridpoints of the lowermost part of domain 1. This can be seen by closely inspecting the horizontal dashed lines in Figure 4.5 which mark the individual sections. As a consequence, the lowermost section of a domain becomes somewhat smaller, whereas the adjacent section below is a little larger compared to the other sections. In practice, this deviation from the described scheme causes no noticeable load imbalance during a simulation.

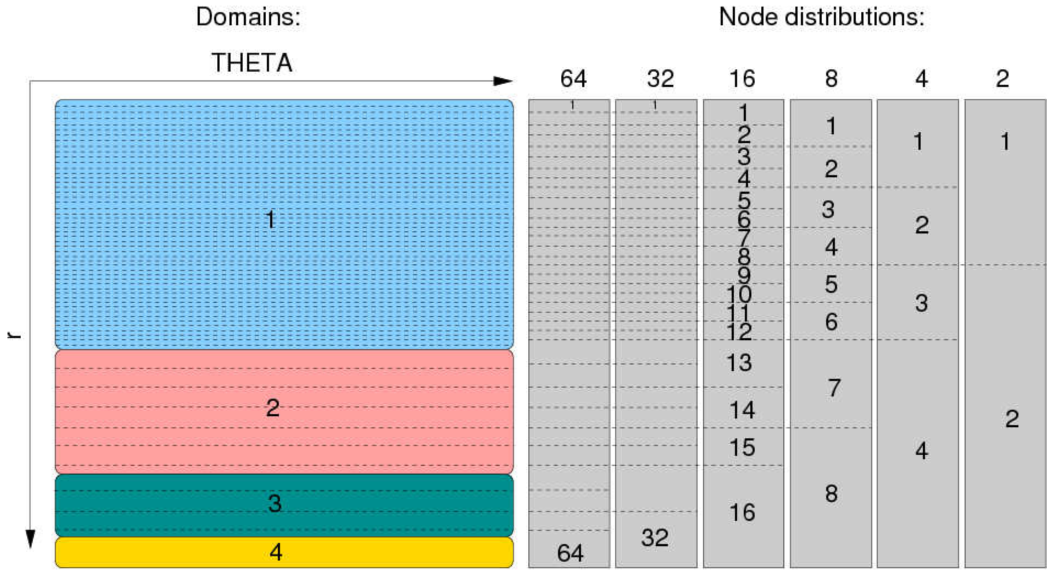

Figure 4.5: *Parallelization scheme for all six implemented total numbers of nodes. The coloured rectangles on the left correspond to the uppermost four domains. Additional domains below the 4th domain usually exist but are not affected by the parallelization scheme for up to 64 nodes, and are therefore omitted. Each of the grey columns on the right shows, for a given total number of nodes, how the depth range of the model space is mapped to the individual nodes.*

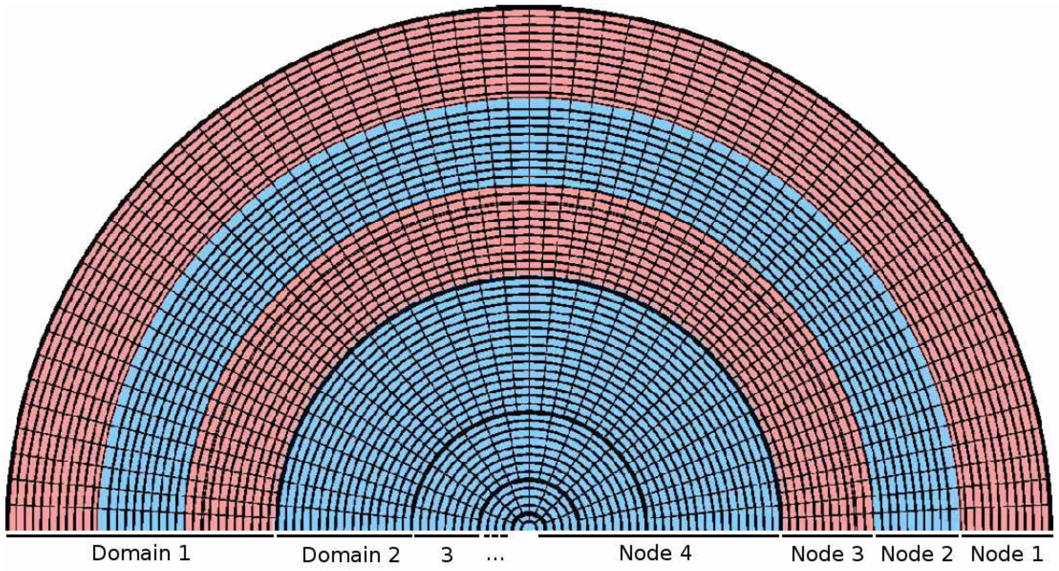

Figure 4.6: *Parallelization scheme for four nodes. The individual domains are outlined with thick black lines, whereas the model regions of the individual nodes are filled with alternating colours. For four nodes, the topmost domain is distributed among the nodes 2, 3 and 4 whereas all underlying domains are assigned to node 1.*

4.6 Outlook on verification

A complete verification of the PSVaxi method, analogous to the verification of the SHaxi method shown in chapter 3, is still missing. However, a comparison performed by Thorne et al. (2003) of individual PSVaxi traces with quasi-analytical seismograms calculated with the reflectivity method (Müller, 1985) for global epicentral distances show a good agreement at least for individual phases (Figure 4.10). Although this does not prove that the source is implemented correctly, it indicates that at least the wave propagation through the media is correctly implemented. As long as a proper verification is missing, the potential of the PSVaxi method is currently restricted to differential comparisons of seismograms, e.g. to investigate how model variations influence the wave field.

4.7 Applications

Although the PSVaxi code is not as advanced as the SHaxi and the Fault3D code, first applications were already performed which use PSVaxi modelling to derive the structure and the seismic properties of the lower mantle. While the first example shown below is rather a sample application, the following two studies on ultra-low velocity zones in the lower mantle (Thorne, Garnero, Jahnke, Treml and Igel, 2003), and on the influence of whole mantle scattering on the Pdiff coda (Thorne, Rost, Jahnke and Igel, 2007) actually expand the current knowledge on the relation between teleseismic signals and small-scale lower mantle structure.

4.7.1 D” layer with small scale topography

The simulation shown below illustrates the potential of the PSVaxi method for studying differential effects caused by model variations in the lower mantle. The motivation was to show how seismic phases passing through the lowermost mantle are affected by undulations of a D” Layer (e.g. Loper & Lay, 1995). In general, the simulation of such models is still a challenge, because the D” Layer is known to have small scale topography (e.g. Bataille & Lund, 1996) and therefore has a significant influence on the high frequency content of teleseismic registrations. To be able to model such effects, a high model resolution over a large extension is necessary to generate appropriate synthetics.

A comparison of two different models derived from the PREM model (Dziewonski and Anderson, 1981) with an additional D” layer is shown: (1) a flat D” layer 300 km on top of the CMB, and (2) a sinusoidal undulating D” layer with the same average thickness. The number of grid points in both simulations was ~11 Mio with a vertical grid spacing of 2 km and a horizontal spacing between 3.5 and 1.8 km. The receivers were placed with 10° spacing between 10° and 180°. The dominant frequency of the seismograms is ~9 s and the depth of the chosen isotropic source ($M_{rr} = M_{\varphi\varphi} = M_{\theta\theta} = M_0$) was set to 600 km. More model parameters are given in Table 4.1.

	Background-Model	D” Thickness	D” Velocity Contrast	D” Wave-length of Topography	D” Amplitude of Topography
Model 1	PREM	300 km	+10%	-	0 km
Model 2	PREM	300 km	+10%	11.6° (760 km)	100 km

Table 4.1: Parameters of the two implemented D” models.

Figure 4.7 shows the ray paths of selected prominent phases which occur in the epicentral distance range between 10° and 180°. Figure 4.8 shows the corresponding synthetic seismograms for both models. The traces of the undulating D” model (blue) are plotted on top of the traces of the flat D” model (red) so that variations between both wave fields appear in red in the seismograms. The prominent phases are labeled following the IASPEI naming convention (Storchak et al., 2003). These are the direct (P) and core diffracted (Pdiff) phase, its multiple (PP), mantle phases which reflect at the core-mantle boundary (PcP, PcS) and phases turning in the outer core (PKP, PKiKP). Additionally, each of the phases show a clear corresponding depth phase (pP, pPcP, etc.). For simplification, the different PKP branches (PKPab, PKPbc and PKPdf) are not explicitly labeled.

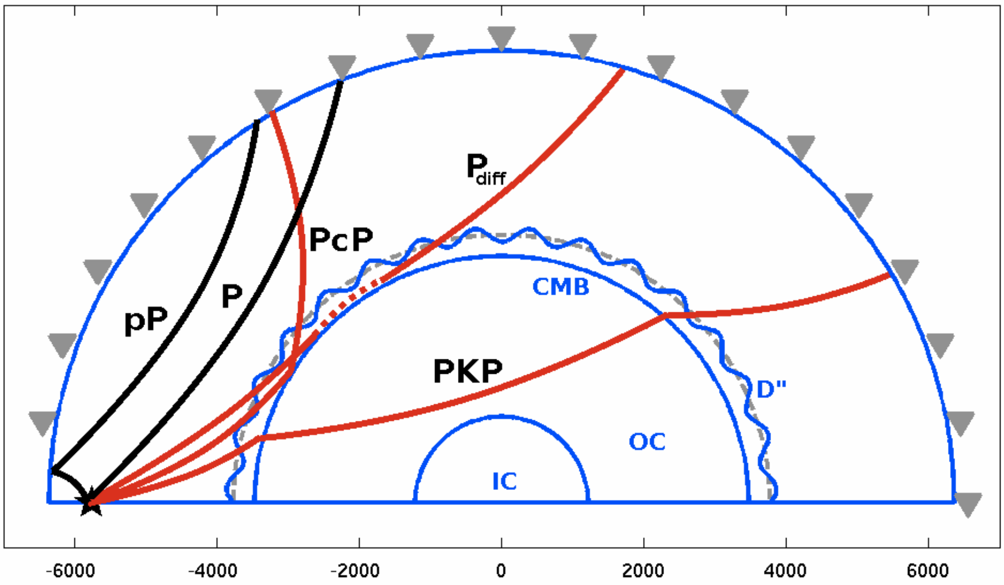

Figure 4.7: *Models with different D” layers together with prominent raypaths. The dashed grey line denotes the flat D” layer model (Model 1), and the overlain blue undulating line denotes the D” layer with sinusoidal topography (Model 2). The grey triangles mark the receiver positions with 10° spacing. The star indicates the source position at 600 km depth. Raypaths of phases which are affected by D” structure are drawn in red, unaffected phases are drawn in black.*

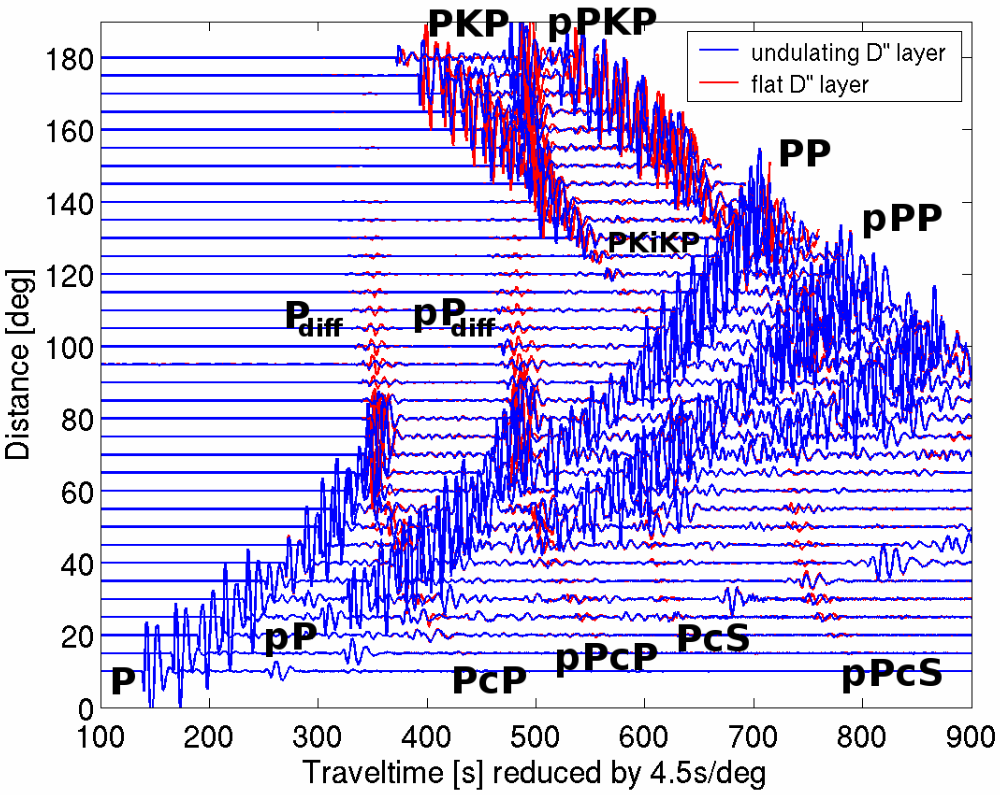

Figure 4.8: *Seismograms (z-component) with labelled phases for the two D” models: (1) flat D” layer model (red traces), and (2) undulating D” layer model (blue traces). Red seismogram segments denote Phases which are affected by the D” structure. For better visibility, the time axis is reduced by 4.5 s/deg.*

The strongest effect of the D” topography is visible for the Pdiff phase between 90° and 140° epicentral distance: due to its shallow incidence angle at the D” layer this phase has the highest sensitivity on the shape of D”. Similar effects are also visible for the core-mantle reflecting phases (PcP, PcS) and the phases entering the outer core (PKP, PKiKP), although their incidence angle at the D” layer is considerably steeper and the resulting path inside D” is shorter. The same pattern is visible for the corresponding depth phases, due to their similar paths in the lower mantel. This is shown in more detail for the Pdiff phase in Figure 4.9. In general, D” topography causes a decrease of the Pdiff amplitude, biases its arrival time and increases the waveform complexity.

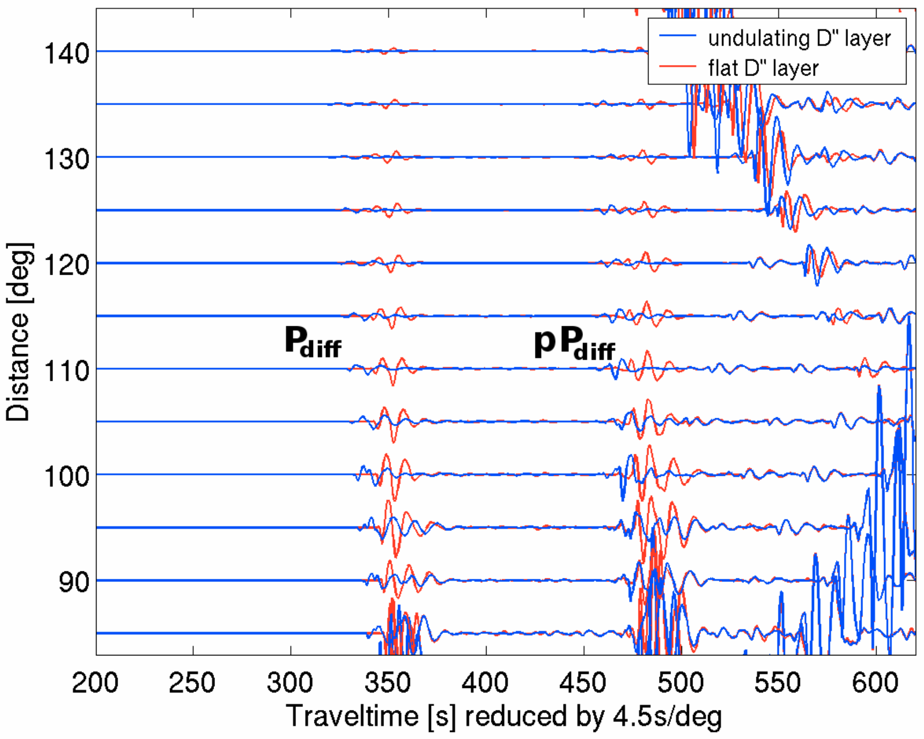

Figure 4.9: *Cutout of Figure 4.8 showing the Pdiff arrival and its corresponding depth phase pPdiff around 110° for both D" models. The variation in arrival time, amplitude and waveform complexity for both models is clearly visible.*

4.7.2 Ultra-low velocity zone with Topography in the D" region

A more detailed investigation of small scale features in the lowermost mantle was performed by Thorne, Garnero, Jahnke, Treml and Igel (2003), who used the PSVaxi code to study differential effects of lower-mantle topography and ultra-low velocity zones (ULVZs) on the teleseismic wave field. In this study, standard lower mantle phases were modelled such as Pdiff, SKS and PKiKP, as well as the SPdKS phase which is generated by an ULVZ lying on top of the core-mantle boundary. Dominant periods down to 5 sec were modelled on the Hitachi SR8000 parallel computer of the Leibniz Supercomputing Center in Munich. The synthetics were compared to a Tonga Islands earthquake recorded across Canada which shows candidate SPdKS arrivals.

Of special interest in this study were topography effects of the core-mantle boundary (CMB) and of Gaussian shaped ULVZs on the diffracted seismic phase SPdKS. The implemented ULVZs are placed inside a PREM background model, have a Gaussian shape and are located directly on top of the core-mantle boundary. Both, ULVZs with constant seismic properties and those with linear vertical gradients were investigated. Typical properties of the implemented ULVZs are: a maximum vertical extension of 20 km, 15% reduction of the S-velocity and 5% reduction of the P-velocity, respectively. The density is increased by 15% with respect to the background PREM model. The modelling showed that the Pdiff phase is strongly affected by ULVZs, especially in the epicentral distance range >110°. While the differences of constant versus gradient ULVZs models on the SPdKS phase are marginal.

In order to show that at least differential effects can be modelled with PSVaxi, a single-station seismogram comparison at 100° epicentral distance was performed using PSVaxi and reflectivity generated synthetics (Figure 4.10). The used model is based on PREM with an additional low-velocity layer of 20 km thickness on top of the CMB and the seismic properties given above. The source used for the reflectivity simulation is a double-couple which provides good S-radiation and negligible P-radiation towards the selected receiver.

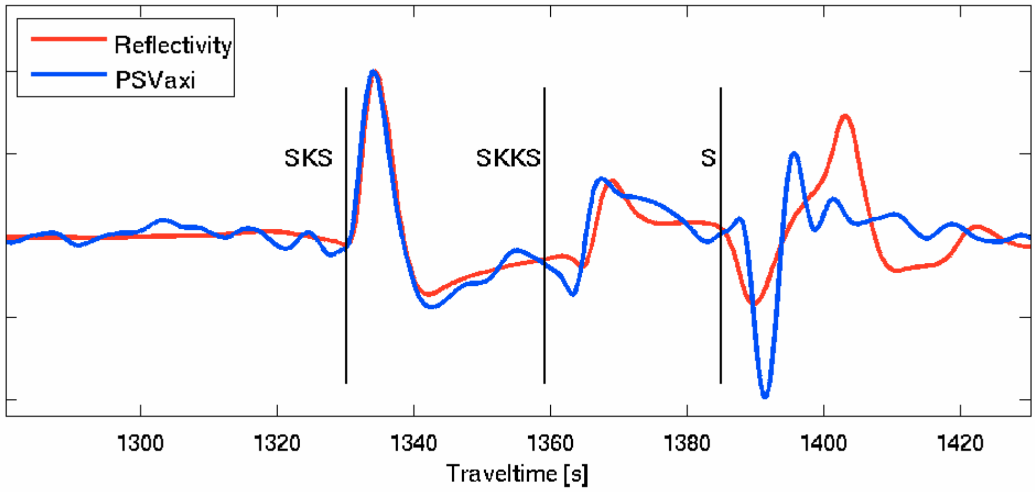

Figure 4.10: *Seismogram comparison of synthetics*[1] *(z-component) calculated with the reflectivity method (red) and PSVaxi (blue) for PREM with an additional low-velocity layer on top of the CMB. The source depth is 400 km and the epicentral distance is 100°. The match of the SKS phase is good, whereas the waveforms differ for the SKKS and S phase, as explained in the text.*

Since it is not possible to use double-couple sources in PSVaxi an axi-symmetric source had to be found which also provides good S-radiation and weak P-radiation, which is obtained by setting $\sigma_{rr}>0$. A drawback of this source is that it is physically unrealistic and that its radiation pattern is different from the pattern of double-couple sources. This biases the calculation of amplitude ratios of phases which have different take-off angles. Those ratios can not be directly compared to amplitude ratios of double-couple generated seismograms. Another reason for the mismatch of the SKKS- and Sdiff phase in Figure 4.10 is that the reflectivity run was performed with a limited slowness-range which embraces the SKS, SKKS and Sdiff phases but not energy travelling with significantly larger slowness values. This energy is a general part of the coda of each phase and is intrinsically contained in the PSVaxi trace but not in the reflectivity trace. However, for the study discussed here this is of minor importance since the influence of model variations on a selected lower mantle phase such as SKS is studied.

---

[1] Synthetics shown in the Figure are courtesy provided by Michael S. Thorne.

Based on this study, Thorne et al. (2008) recently performed a more detailed investigation of SPdKS arrivals using PSVaxi synthetics where a dataset of 37 deep focus Tonga-Fiji earthquakes are considered. The data reveals a surprisingly complex fine-scale low-velocity structure of the study region.

4.7.3 Pdiff coda from whole mantle scattering

In a recent study of Thorne, Rost, Jahnke and Igel (2007), scattering properties of the mantle were derived from the coda of the Pdiff phase for a set of earthquakes at 95° - 135° distance recorded at the Yellowknife (YKA) array in Canada.

In this study, waveform stacks of the data with synthetic PSVaxi generated seismograms with dominant periods down to 2-3 seconds are compared (Figure 4.11). The YKA data was stabilized using a binning technique of magnitude corrected traces. The whole section of individual stacks is normalized with respect to the PP phase.

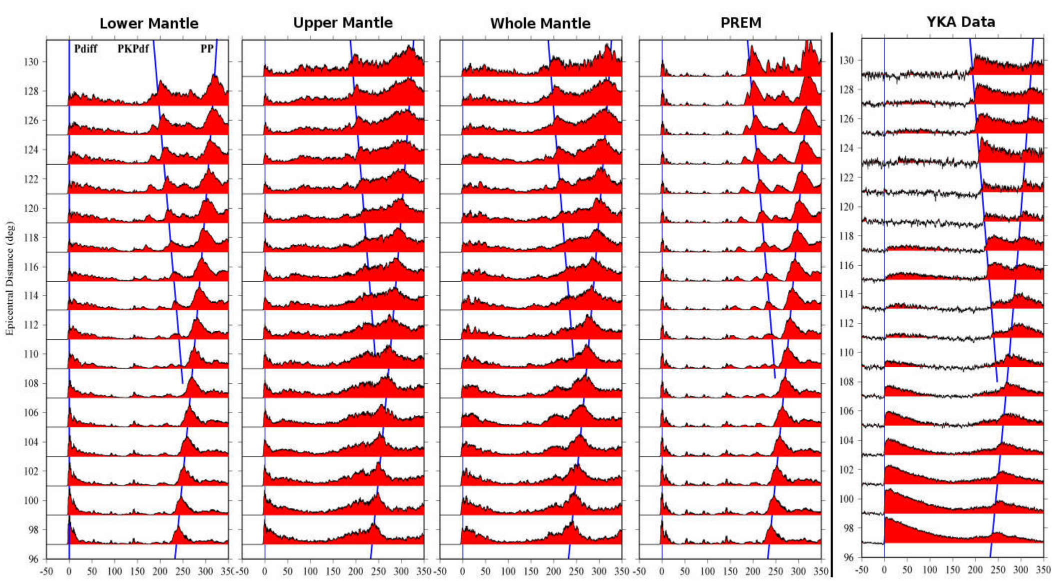

Figure 4.11: *Envelope stacks*[1] *for the models with five different scattering regimes compared with data. Corresponding models from left to right: (1) scattering in the lower mantle only, (2) scattering in the upper mantle only, (3) whole mantle scattering, (4) PREM (no scattering) and (5) data recorded at the Yellowknife array. The blue lines denote the arrival times of the phases Pdiff, PKPdf and PP, as labelled in the leftmost section.*

---

[1] Figure courtesy of Michael S. Thorne (Thorne et al., 2007).

Besides a pure PREM model, three general classes of models were taken into account: (1) perturbations in the upper mantle only, (2) perturbations in the lower mantle only and, (3) whole mantle perturbations.

In the selected distance range, the Pdiff phase is followed the PP- and the PKPdf phase, which arrive 200–300 seconds later, depending from the individual epicentral distance. Due to the lack of other phases, seismic energy which arrives in this time interval can be interpreted as Pdiff coda which is generated by scatterers in the mantle.

The two model classes with scattering only in the upper or lower section of the mantle were not able to explain the observed Pdiff coda in the data stacks. The best fit was obtained by a whole mantle scattering model with 20 km correlation length and 2% RMS amplitude of the perturbations, although the fit is not perfect.

The correlation length and amplitude differs from results of other studies which predict mantle scattering with scale lengths between 2-8 km and RMS perturbations between 0.5-4% (Earle & Shearer, 2001, Shearer & Earle, 2004, Hedlin et al., 1997). This difference is not surprising, since the dominant period of about 3 seconds which was achieved does not completely match the frequency content of the data.

Chapter 5:

General Discussion and Conclusion

5.1 Trapped wave modelling

The developed parallel Fault3D code allows to model the full 3D wavefield for arbitrary fault zone geometries and realistic frequencies. This makes it a valuable tool for further investigations of the 3D parameter space of possible fault zone geometries, as exemplarily shown in chapter 2 for selected irregular fault zone structures. In general, further insights in the relation between geometry and trapping efficiency for complex fault zone structure are necessary to improve the derivation of fault structure at depth from measured data.

5.1.1 Impact on recent studies

Since the work of this chapter has been published in Jahnke et al. (2002) and Igel et al. (2002) significant progress has been made in the field of trapped waves research, as can be seen by the numerous publications which have been released. This section gives an overview of the impact which these two publications already had on other trapped wave studies. A total number of about 20 publications were found referring to the aforementioned two papers, covering a broad range of topics such as fault zone investigations at various places in the world, analysis of the rupture propagation process, studies about trapped wave generation in subduction zones and crosswell seismic surveys of oil fields. Three findings from the two publications were taken into account in most of these studies:

1. Trapped waves can be generated in shallow faults by sources located well outside and below the low-velocity zone.
2. Trapped wave generation is robust against model variations such as vertical velocity gradients, gradual geometric variations and small-scale perturbations.
3. Different types of fault zone variations alter the trapped waves to a quite different degree, enabling reasonable model simplifications and focusing on resolvable model features.

5.1.2 Trapped waves in shallow faults

During the last few years, a growing number of fault zone systems revealed a shallow low-velocity structure. Several studies deal with these shallow fault zones, for which trapped waves were generated by sources located outside the fault:

Rovelli et al. (2002) investigated a fault which crosses the town Nocera Umbra in central Italy. They found trapped waves with strong amplitude amplifications, generated by a subcrustal earthquake occurring almost vertically, well below the fault.

Cultreira et al. (2003) analyzed a set of earthquakes in the same region, finding shallow structure and a remarkable stability of spectral ratios for various event azimuths. Their results have implications on the seismic hazard estimation for Nocera Umbra.

Ben-Zion et al. (2003) found shallow fault-zone structure in the Karadere-Duzce branch of the North Anatolian Fault, western Turkey, by analysis of trapped wave arrivals. They discuss the implications on seismic hazard estimation due to the so far underestimated volume of sources which is capable of generating strong amplitudes at the surface in the vicinity the fault.

Peng et al. (2003) analyzed a large data set of aftershocks of the the 1992 Landers, California, earthquake recorded by at a dense network across the affected fault system. They found strong indications for shallow fault structure and a large volume of sources below the structure being capable of coupling trapped waves into the fault system.

Lewis et al. (2005) investigated the shallow seismic trapping structure of branches of in the San Jacinto fault zone near Anza, California, with a large dataset of small earthquakes. They found a shallow trapping structure which extends to depths of 3-5 km, in contrast to other studies which predict a deeper extension down to 15-20 km.

Mizuno and Nishigami (2006) discuss the structure of the Nojima Fault, southwest Japan, derived from borehole seismic data containing trapped wave arrivals. Their results concerning shallow fault zone structure, fault width and velocity contrast differ significantly from previous studies based on surface observations only.

Fohrmann et al. (2003) extended the investigations from Jahnke et al. (2002) and Igel et al. (2002) on the capability of sources outside shallow faults to generate trapped waves. A central point of their study is the quantification of the size of the source volume outside the fault which is capable of generating trapped waves.

5.1.3 Influence of 2D and 3D model variations

Mamada et al. (2002; 2004) derived the uppermost structure of the Mozumi-Sukenobu fault, central Japan from fault zone waves generated by nearsurface explosions and recorded by an array in a research tunnel crossing the fault at 300 m depth. Their results indicate a discontinuous and kinked fault structure, comparable to the models in Jahnke et al. (2002), but aligned in horizontal dicrection. Moreover, they found trapped waves for shallow sources located at some distance to the fault analogous to the modelling of sources below shallow fault zone structures.

Kilb and Hardebeck (2006) performed a calculation of focal mechanisms for microearthquakes occurring at three Californian faults: the Calaveras fault, the Sargent fault and a segment of the San Andreas fault. They found that unmodeled 3D fault structure can bias the focal mechanism solutions calculated from first-motion polarity.

Haberland et al. (2003) studied the Arava Fault at the Dead Sea transform in the Middle East with seismic explosion data. They discuss the effect of possible 3D structure on their 2D inversion results. Moreover they observe effects which can be explained with the model of a low-velocity layer on top of a the fault which widens towards the surface.

5.1.4 Model generation

In the studies of Rovelli et al. (2002), Ben-Zion et al. (2003), Peng et al. (2003), Mamada et al. (2002; 2004), Lewis et al. (2005; 2007), Nielsen et al. (2005), Leary et al. (2005) modelling of wave propagation in fault zones was performed to constrain the results from data analysis. The applied simplifications in the models were based on the findings in Jahnke et al. (2002) about those kinds of variations of fault-zone structure which do not significantly influence the wave field at the surface.

5.1.5 Other studies

Finally, other studies refer to Jahnke et al. (2002) and Igel et al. (2002) for different purposes:
Hong and Kennett (2003) modeled heterogeneous low-velocity regions using a wavelet-based method with application to fault zone and slab regimes.
Rietbrock (2006) also studied slabs in connection with trapped waves and found a possible a waveguide on top of the slab of the Chile-Peru subduction zone.
Groby and Wirgin (2005) derived analytically the seismic response of a site comprising a soft viscoelastic layer on top of a homogeneous elastic half space. This model is capable of generating Love-type modes they describe as being comparable to trapped waves in vertical fault-zone structure.
Johnson & Nadeau (2005) calculated the dynamic solution for an asperity model of an earthquake with the boundary integral method and compared their synthetics with data recorded at a section of the San Andreas fault near Parkfield. The signature of trapped waves in the seismograms was discussed in order to separate propagation effects from the source effects which were primary investigated.
McGuire and Ben-Zion (2005) and also Lewis et al. (2007) investigated the Bear Valley section of the San Andreas fault with fault-zone head waves. They found that head waves are more sensitive to deep fault structure than trapped waves. This is important to resolve whether or not a fault extends throughout the seismogenic zone.
Karabulut and Bouchon (2007) observed spatial variability of strong ground motion near a segment of the North Anatolian fault recorded at a small array close to the fault.

5.1.6 Outlook on trapped wave modelling

In this thesis, just a few realisations of possible 3D variations of fault zone models could be investigated. However, for a comprehensive understanding of the general effects of 3D fault zone structure on the trapping efficiency a more detailed parameter search of likely 3D structures has to be performed. The steady increase of available computational resources of systems which are accessible for scientific research allows it to perform a large number of individual simulations, each covering one 3D model realization from the parameter space.

5.2 Global SH and P-SV wave propagation

The SHaxi and PSVaxi programs already proved to be efficient tools for modelling teleseismic data, as was shown in the applications discussed in this thesis. In comparison with other modelling methods, the benefit of axi-symmetric methods consists in the comparably high frequencies which can be modelled on a global scale with reasonable computational resources. For instance, dominant periods down to 1 sec can be achieved using a fraction of a current high performance parallel computer, as well as 5 sec on current medium sized PC clusters periods in the order of. This covers the periods of interests in most teleseismic studies and allows a direct data interpretation.
The constraint of SHaxi and PSVaxi to axi-symmetric models restricts possible data interpretation based on SHaxi or PSVaxi generated seismograms to effects which are caused by propagation effects in the great circle plane. For other questions different approaches such as full 3D methods or hybrid 2D-3D methods are appropriate, which require either significantly more computational resources or do often not provide the complete 3D wavefield, due to the 3D-2D transition.

So far, SHaxi and PSVaxi were used in studies where small scale lower mantle structure was derived using seismic signatures at comparatively short periods:
Lay at al. (2006) found a local phase transition in the lowermost mantle and derived absolute temperature and head flux from S-velocity contrasts. SHaxi synthetics enabled to estimate these values with increased precision, since topography effects on seismic signatures could be taken into account.

Thorne et al. (2007) compared lower mantle S-velocity models of a certain study area gained with different data analysis technique and revealed their limits by comparison of SHaxi generated synthetics with real data. Their study showed that small scale topography has to be explicitly modelled, e.g. by using axi-symmetric or full 3D modelling techniques, for obtaining realistic models.

Schmerr et al. (2003) used SHaxi to investigate mid mantle S-velocity structure, namely topography of the transition zone discontinuities beneath the Hawaiian hotspot, which is likely caused by upwelling of hot plume material from the lower mantle. Their study gives insights on the waveform characteristics which have to be expected when phases reflecting from undulating mid mantle discontinuities are considered.

Thorne et al. (2003 and 2008) investigated data and PSVaxi generated synthetics of models with Gaussian-shaped ultra-low velocity structure in the D” region, showing that such structures produce strong signatures in Pdiff waveforms. The discovery of such ultra-low velocity structures helps to improve the knowledge about geodynamic processes in the lower mantle right above the core-mantle boundary, which acts as a geodynamic motor due to the large heat flux across this boundary.

Thorne et al. (2007) presented a study about the general scattering properties of the mantle derived from the Pdiff coda using PSVaxi synthetics and data. PSVaxi generated synthetics showed systematic effects on the Pdiff coda as a function of epicentral distance, which depend on the depth where the scattering takes place. Their results indicate that only whole mantle scattering explains the observed characteristics of the Pdiff coda, although the used depth-independent scattering properties seem to be inappropriate to explain the data well. Their work is a promising step towards constraining the small scale scattering properties of the mantle and helps to improve our geodynamic knowledge as well as to understand general properties of the teleseismic P-coda.

The applications discussed above indicate that the codes developed in this thesis are valuable tools to understand how complex fine-scale seismic structure can be derived from seismograms. In general, to maximize the benefit of numerical codes for the scientific community the programs must be accessible for public use *in the long term*. The SPICE code library which hosts the codes among a pool of other verz useful codes was created to enable developers to ensure this long time accessibility. The Fault3D, SHaxi and PSVaxi code can be accessed there for public use.

Bibliography

Aki, K. & Richards, P. G., 2002. Quantitative seismology, 2nd Edition, *University Science Books.*

Alterman, Z. & Karal, F. C., 1968. Propagation of elastic waves in layered media by finite-difference methods, *Bull. Seism. Soc. Am.*, **58**, 367-398.

Baig, A.M. & Dahlen, F.A., 2004. Traveltime biases in random media and the *S*-wave discrepancy, *Geophys. J. Int.*, **158**, 922-938.

Bataille, K.& Lund, F., Strong scattering of short-period seismic waves by the core-mantle boundary and the P-diffracted wave, 1996. *Geophys. Res. Lett.*, **23**, 18, 2413-2416.

Ben-Zion, Y., 1989. The response of two joined quarter spaces to SH line sources located at the material discontinuity interface, *Geophys. J. Int.,* **98**, 213-222.

Ben-Zion, Y., 1990. The response of two half spaces to point dislocations at the material interface, *Geophys. J. Int.*, **101**, 507-528.

Ben-Zion, Y. & Aki, K., 1990. Seismic radiation from an SH line source in a laterally heterogeneous planar fault zone, *Bull. Seism. Soc. Am.*, **80**, 971-994.

Ben-Zion, Y. & Malin, P., 1991. San Andreas fault zone head waves near Parkfield, California, *Science*, **251**, 1592-1594.

Ben-Zion, Y., Katz, S. & Leary, P. C., 1992. Joint inversion of fault zone head waves and direct P arrivals for crustal structure near major faults, *J. Geophy. Res.*, **97**, 1943-1951.

Ben-Zion, Y., 1998. Properties of seismic fault zone waves and their utility for imaging low-velocity structures, *J. Geophy. Res.*, **103**, 12567-12585.

Ben-Zion, Y., 1999. Corrigendum: The Response of Two Half Spaces to Point Dislocations at the Material Interface by Ben-Zion (1990), *Geophys. J. Int.*, **137**, 580-582.

Ben-Zion, Y. & Sammis, C. G., 2001. Characterization of Fault Zones, Pure Appl. Geophys., **160**, 677-715.

Ben-Zion, Y., Peng, Z., Okaya, D., Seeber, L., Armbruster, J. G., Ozer, N., Michael, A. J., Baris, S. & Aktar, M., 2003. A shallow fault-zone structure illuminated by trapped waves in the Karadere-Duzce branch of the North Anatolian Fault, western Turkey, *Geophys. J. Int.*, **152**, 699-717.

Chaljub, E. & Tarantola, A., 1997. Sensitivity of *SS* precursors to topography on the upper-mantle 660-km discontinuity. *Geophys. Res. Lett.*, **24** (21), 2613-2616.

Cleary, J.R. & Haddon, R.A.W., 1972. Seismic wave scattering near core-mantle boundary – new interpretation of precursors to PKP, *Nature*, **240** (5383), 549.

Cormier, V. F. & Spudich, P., 1984. Amplification of ground motion and waveform complexities in fault zones: examples from the San Andreas and Calaveras faults, *Geophys. J. R. astr. Soc.*, **79**, 135-152.

Cormier, V. F. & Beroza, G. C., 1987. Calculation of strong ground motion due to an extended earthquake source in a laterally varying structure, *Bull. Seism. Soc. Am.*, **77**, 1-13.

Cormier, V.F., 2000. D" as a transition in the heterogeneity spectrum of the lowermost mantle. *J. Geophys. Res.*, **105**, 16193-16205.

Cultreira, G., Rovelli, A., Mele, G., Riccardo, A., Caserta, A. & Marra, F., 2003. Azimuth-dependent amplification of weak and strong ground motions within a fault zone (Nocera Umbra, central Italy), *J. Geophys. Res.*, **108** (B3), 2156.

Davies, G.F., 2002. Stirring geochemistry in mantle convection models with stiff plates and slabs. *Geochemica et Cosmochimica Acta*, **66** (17), 3125-3142.

Dziewonski, A. & Anderson, D. L, 1981. Preliminary reference Earth model, *Phys. Earth. Planet. Int.*, **25**, 297-356.

Earle, P.S. & Shearer, P.M., 2001. Distribution of fine-scale mantle heterogeneity from observations of Pdiff coda, *Bull. Seismol. Soc. Am.*, **91**, 1875-1881.

Fohrmann, M., Igel, H., Jahnke, G. & Ben-Zion, Y., 2004. Guided Waves from Sources Outside Faults: An Indication for Shallow Fault Zone Structure? *Pure Appl. Geophys.* **161** (2004) 1-13.

Frankel, A. & Clayton, R.W., 1984. A Finite Difference Simulation of Wave Propagation in Two-dimensional Random Media, *Bull. Seism. Soc. Am.*, **74** (6), 2167-2186.

Frankel, A. & Clayton, R.W., 1986. Finite Difference Simulations of Seismic Scattering: Implications for the Propagation of Short-Period Seismic Waves in the Crust and Models of Crustal Heterogeneity, *J. Geophys. Res.*, **91** (B6), 6465-6489.

Frankel, A., 1989. A Review of Numerical Experiments on Seismic Wave Scattering, *Pure and Applied Geophysics*, **131** (4), 639-685.

Fukao, Y., Hori, S. & Ukawa, M., 1983. A seismological constraint on the depth of basalt-eclogite transition in a subducting oceanic crust, *Nature*, **303**, 413-415.

Furumura T. & Takenaka, H., 1996. 2.5-D modeling of elastic waves using the pseudospectral method, *Geophys. J. Int.*, **124**, 820-832.

Furumura, T., Kennett, B.L.N., Furumura, M., 1998. Seismic wavefield calculation for laterally heterogeneous spherical earth models using the pseudospectral method, *Geophys. J. Int.,* **135**, 845-860.

Gallovič, F., Barsch, R., Alvarez, J. P. & Igel, H., 2007. Digital Library for Computational Seismology, *Eos Trans. AGU,* **88**(50), 559.

Grand, S. P., 2002. Mantle shear-wave tomography and the fate of subducted slabs, *Philos. Trans. R. Soc. Lond. Ser. A-Math. Phys. Eng. Sci.,* **360,** 2475–2491.

Graves, R.W., 1993. Modelling 3-D site response effects in the Marina district basin, San Francisco, Cal., *Bull. Seism. Soc. Am.*, **83**, 1042-1063.

Graves, R.W., 1996. Simulating seismic wave propagation in 3D elastic media using staggered-grid finite differences, *Bull. Seism. Soc. Am.*, **86** (4), 1091-1106.

Groby, J. P. & Wirgin, A., 2005. Two-dimensional ground motion at a soft viscoelastic layer/hard substratum site in response to SH cylindrical seismic waves radiated by deep and shallow line sources — I. Theory, *Geophys. J. Int.,* **163**, 165-191.

Haberland, C., Agnon, A., El-Kelani, R., Maercklin, N., Qabbani, I., Rümpker, G., Ryberg. T., Scherbaum, F. & Weber, M., 2003. Modeling of seismic guided waves at the Dead Sea Transform, *J. Geophys. Res.*, **108** (B7), 2342.

Harris, R. A. & Day, S. M., 1993. Dynamics of Fault Interaction: Parallel Strike-Slip Faults, *J. Geophy. Res.*, **98**, 4461-4472.

Hedlin, M. A. H, Shearer, P.M. & Earle, P.S., 1997. Seismic evidence for small-scale heterogeneity throughout Earth's mantle, *Nature*, **387**, 145.

Hong, T. K. & Kennett, B. L. N., 2003. Modelling of seismic waves in heterogeneous media using a wavelet-based method: application to fault and subduction zones, *Geophys. J. Int.*, **154**, 483-498.

Hough, S. E., Ben-Zion, Y. & Leary, P. C., 1994. Fault-zone waves observed at the Southern Joshua Tree earthquake rupture zone, *Bull. Seism. Soc. Am.*, **84**, 761-767.

Huang, B. S., T.-L. Teng, Y. T. Yeh, 1995. Numerical modeling of fault-zone trapped waves: acoustic case, *Bull. Seism. Soc. Am.*, **85**, 1711-1717.

Igel, H., Mora, P., Rodriguez, D. & Leary, P. C., 1991. Finite-difference simulation of fault zone trapped waves on the massively parallel Connection Machine (abstract), *EOS. Trans. Am. Geophys. Un.*, **72**, 307.

Igel, H., Debski, W., Djikpesse, H. & Tarantola, A., 1993. Gradient inversion of marine seismic reflection data: parameterization and geometrical spreading, *Society of Exploration Geophysicists, Meeting 1993, Technical Programme*, 657-660.

Igel, H., & Weber, M., 1995. SH-wave propagation in the whole mantle using high-order finite differences, *Geophys. Res. Lett.,* **22** (6), 731-734.

Igel, H., & Weber, M., 1996. P-SV wave propagation in the Earth's mantle using finite-differences: application to heterogeneous lowermost mantle structure, *Geophys. Res. Lett.*, **23**, 415-418.

Igel, H., & Gudmundsson, O. 1997., Frequency-dependent effects on travel times and waveforms of long-period S and SS waves, *Phys. Earth Planet. Inter.,* **104**, 229-246.

Igel, H., Ben-Zion & Y., Leary, P., 1997. Simulation of SH- and P-SV-wave propagation in fault zones, *Geophys. J. Int.*, **128**, 533-546.

Igel, H., 1999. Wave propagation in three-dimensional spherical sections by the Chebyshev spectral method, *Geophys. J. Int.,* **136**, 559-566.

Igel, H., Takeuchi, N., Geller, R. J., Megnin, C., Bunge, H. P., Clevede, E., Dalkolmo, J. & Romanowicz, B., 2000. The COSY Project: verification of global seismic modeling algorithms, *Phys. Earth Planet. Inter.,* **119**, 3-23.

Igel, H., Nissen-Meyer, T. & Jahnke, G., 2001. Wave propagation in 3-D spherical sections: effects of subduction zones, *Phys. Earth Planet. Inter.,* **132**, 219-234.

Igel, H., G. Jahnke & Y. Ben-Zion, 2002. Numerical simulation of fault zone trapped waves: accuracy and 3-D effects, *Pure Appl. Geophys*., **159**, 2067–2083.

Igel, H., 2004. New European training network to improve young scientists' capabilities in computational wave propagation, *Eos Trans. AGU*, **5**(28), 267.

Ikelle, L.T., Yung, S.K. & Daube, F., 1993. 2-D random media with ellipsoidal autocorrelation functions, *Geophysics*, **58** (9), 1359-1372.

Jahnke, G., Igel, H. & Ben-Zion, Y., 2002. Three-dimensional calculations of fault zone guided waves in various irregular structures, *Geophys. J. Int.,* 161**, 416-426.**

Jahnke, G., Thorne, M. S., Cochard, A. & Igel, H., 2008. Global SH-wave propagation using a parallel axi-symmetric spherical finite-difference scheme: application to whole mantle scattering, *Geophys. J. Int.,* **173**, 815-826.

Johnson, L. R. & Nadeau R. M., 2005. Asperity Model of an Earthquake: Dynamic Problem, *Bull. Seism. Soc. Am.*, **95** (1), 75-108.

Karabulut, H., Bouchon, M., 2007. Spatial variability and non-linearity of strong ground motion near a fault, *Geophys. J. Int.*, **170**, 262-274.

Kilb, D. & Hardebeck, J. L., 2006. Fault Parameter Constraints Using Relocated Earthquakes: A Validation of First-Motion Focal-Mechanism Data, *Bull. Seism. Soc. Am.*, **96** (3), 1140-1158, doi: 10.1785/0120040239.

Klimeš, L., 2002a. Correlation Functions of random media, *Pure and Applied Geophysics,* **159**, 1811-1831.

Klimeš, L., 2002b. Estimating the correlation function of a self-affine random medium, *Pure and Applied Geophysics*, **159**, 1833-1853.

Lay, T., Garnero, E. J. & Russell, S. A., 2004. Lateral variation of the D" discontinuity beneath the Cocos Plate, *Geophys. Res. Lett.,* **31,** doi:10.1029/2004GL020300.

Lay, T., Hernlund, J., Garnero, E. J. & Thorne, M. S., 2006. A Post-Perovskite Lens and D" Heat Flux Beneath the Central Pacific, *Science,* **314** No. 5803, 1272-1276.

Leary, P. C., Li, Y.-G. & Aki, K., 1987. Observations and modeling of fault zone fracture anisotropy, I, P, SV, SH travel times, *Geophys. J. R. astr. Soc.*, **91**, 461-484.

Leary, P. C., H. Igel & Y. Ben-Zion, 1991. Observation and modeling of fault zone trapped waves in aid of precise precursory microearthquake location and evaluation, Earthquake Prediction: State of the Art, *Proceedings International Conference, Strasbourg, France*, 15-18 October 1991, pp. 321-328.

Leary, P., Igel, H., Mora, P. & Rodrigues, D., 1993. Finite-difference simulation of trapped wave propagation in fracture low-velocity layers, *Can. J. Expl. Geop.*, **29**, 31-40.

Leary, P. C., Ayres, W., Yang, W. J. & Chang, X. F., 2005. Crosswell seismic waveguide phenomenology of reservoir sands & shales at offsets >600 m, Liaohe Oil Field, NE China, *Geophys. J. Int.,* **163**, 285-307.

Lee, W., & Sato, H., 2003. Estimation of S-wave scattering coefficient in the mantle from envelope characteristics before and after the ScS arrival, *Geophys. Res. Lett.,* **30** (24), 2248.

Levander, A. R., 1988. Fourth-order finite-difference P-SV seismograms. *Geophysics*, **53** (11), 1425-1436.

Lewis, M. A., Peng, Z., Ben-Zion, Y. & Vernon, F. L., 2005. Shallow seismic trapping structure in the San Jacinto fault zone near Anza, California. *Geophys. J. Int.,* **162**, 867-881.

Lewis, M. A., Ben-Zion, Y. & McGuire, J. J., 2007. Imaging the deep structure of the San Andreas Fault south of Hollister with joint analysis of fault zone head and direct P arrivals. *Geophys. J. Int.*, **169**, 1028-1042.

Li, Y. G. & Leary, P. C., 1990. Fault zone seismic trapped waves, *Bull. Seism. Soc. Am.*, **80**, 1245-1271.

Li, Y. G., Aki, K., Adams, D. & Hasemi, A., 1994a. Seismic guided waves trapped in the fault zone of the Landers, California, earthquake of 1992, *J. Geophy. Res.*, **99**, 11705-11722.

Li, Y. G., Vidale, J. E., Aki, K., Marone, C. J. & Lee, W. H. K., 1994b. Fine structure of the Landers fault zone: segmentation and the rupture process, *Science*, **265**, 367-370.

Li, Y. G. & J. E. Vidale, 1996. Low-Velocity Fault-Zone Guided Waves: Numerical Investigations of Trapping Efficiency, *Bull. Seism. Soc. Am.*, **86**, 371-378.

Li, Y. G., Vidale, J. E., Aki, K., Xu, F. & Burdette, T., 1998. Evidence of shallow fault zone strengthening after the 1992 M7.5 Landers, California earthquake, *Science*, **279**, 217-219.

Li, X., Kind, R., Yuan, X., Sobolev, S.V., Hanka, W., Ramesh, D. S., Gu, Y. & Dziewonski, A.M., 2003. Seismic observation of narrow plumes in the oceanic upper mantle, *Geophys. Res. Lett.*, 30 (6), 1334.

Loper, D. E. & Lay, T., 1995. The core-mantle boundary region, *J. Geophys. Res.*, **100**, B4, 6397-6420.

Makinde, W., Favretto-Cristini, N., & de Bazelaire, E., 2005. Numerical modeling of interface scattering of seismic wavefield from a random rough interface in an acoustic medium: comparison between 2D and 3D cases, *Geophysical Prospecting*, **53**, 373-397.

Mamada, Y., Kuwahra, Y., Ito & H., Takenaka, H., 2002. 3-D finite-difference simulation of seismic fault zone waves - Application to the fault zone structure of the Mozumi-Sukenobu fault, central Japan, *Earth, Planets Space*, **54**, 1055-1058.

Mamada, Y., Kuwahara, Y., Ito, H. & Takenaka, H., 2004. Discontinuity of the Mozumi-Sukenobu fault low-velocity zone, central Japan, inferred from 3-D finite-difference simulation of fault zone waves excited by explosive sources. *Tectonophysics*, **378,** 209-222.

Margerin, L., & Nolet, G., 2003. Multiple scattering of high-frequency seismic waves in the deep Earth: Modeling and numerical examples, *J. Geophys. Res.,* **108** (B5), doi:10.1029/2002JB001974.

Martin, S. & Rietbrock, A., 2006. Guided waves at subduction zones: dependencies on slab geometry, receiver locations and earthquake sources, *Geophys. J. Int.,* **167**, 693-704.

McGuire, J. & Ben-Zion, Y., 2005. High-resolution imaging of the Bear Valley section of the San Andreas fault at seismogenic depths with fault-zone head waves and relocated seismicity, *Geophys. J. Int.,* **163**, 152-164.

Michael, A. J. & Y. Ben-Zion, 1998. Inverting fault zone trapped waves with a genetic algorithm, *EOS. Trans. Am. Geophys. Un.*, **79**, F584.

Mizuno, T. & Nishigami, K, 2006. Deep structure of the Nojima Fault, southwest Japan, estimated from borehole observations of fault-zone trapped waves, *Tectonophysics*, **417** (3-4): 231-247.

Müller, G., 1985. The reflectivity method: A tutorial, *J. Geophys.*, **58**, 153-174.

Nielsen, L., Thybo, H. & Jørgensen, M. I., 2005. Integrated seismic interpretation of the Carlsberg Fault zone, Copenhagen, Denmark. *Geophys. J. Int.*, **162**, 461–478.

Nissen-Meyer, T., Fournier, A., & Dahlen, F. A., 2007. A 2-D spectral-element method for computing spherical-earth seismograms - I. Moment-tensor source, *Geophys. J. Int.*, **168** (3), 1067-1093.

Peng, Z., Ben-Zion, Y. & Michael, A. J., 2000. Inversion of Seismic Fault Zone Waves in the Rupture Zone of the 1992 Landers Earthquake for High Resolution Velocity Structure at Depth, *EOS. Trans. Am. Geophys. Un.*, **81**, F1146.

Peng, Z., Ben-Zion, Y., Michael, A. J. & Zhu, L., 2003. Quantitative analysis of seismic fault zone waves in the rupture zone of the 1992 Landers, California, earthquake: evidence for a shallow trapping structure. *Geophys. J. Int.*, **155**, 1021-1041.

Rovelli, A., Caserta, A., Marra, F. & Ruggiero, V., 2002. Can Seismic Waves Be Trapped inside an Inactive Fault Zone? The Case Study of Nocera Umbra, Central Italy, *Bull. Seism. Soc. Am.*, **92** (6), 2217-2232.

Saito, T., Sato, H., Fehler, M. & Ohtake, M. 2003. Simulating the envelope of scalar waves in 2D random media having power-law spectra of velocity fluctuation, *Bull. Seism. Soc. Am.*, **93** (1), 240-252.

Sato, H., & Fehler, M. C., 1998. Seismic Wave Propagation and Scattering in the Heterogeneous Earth, *Springer-Verlag*, New York, 308 pages.

Schmerr, N., Garnero, E., Igel, H., Treml, M. & Jahnke, G., 2003. Probing the nature of the 410- and 660-km discontinuities beneath hotspots using the SS-precursors. *Eos Trans. AGU,* **84**(46), Fall Meet. Suppl., Abstract S21E-0356.

Shearer, P.M. & Earle, P.S., 2004. The global short-period wavefield modeled with a Monte Carlo seismic phonon method. *Geophys. J. Int.*, **158**, 1103-1117.

Storchak, D.A., J. Schweitzer & P. Bormann (2003). The IASPEI Standard Seismic Phase List, *Seismol. Res. Lett.* **74** (6), 761-772.

Thomas, C., Igel, H., Weber, M. & Scherbaum, F., 2000. Acoustic simulation of P-wave propagation in a heterogeneous spherical Earth: Numerical method and application to precursor energy to PKPdf, *Geophys. J. Int.* **141**, 307-320.

Thomas, C., Garnero, E. J. & Lay, T., 2004. High-resolution imaging of lowermost mantle structure under the Cocos plate, *J. Geophys. Res.-Solid Earth,* **109,** doi:10.1029/2004JB003013.

Thorne, M. S., Garnero, E., Jahnke, G., Treml, M. & Igel, H., 2003. Investigating the Core-Mantle Boundary and ULVZ Topography with Synthetic FD Seismograms for 3-D Axi-Symmetric Geometries: Predictions and Data, *Eos Trans. AGU*, **84**(46), Fall Meet. Suppl., Abstract U51B-0003.

Thorne, M. S., Rost, S., Jahnke, G. & Igel, H., 2007. Analysis of Pdiff coda using the axi-symmetric finite difference method, *Eos Trans. AGU*, **88**(52), Fall Meet. Suppl., Abstract S51D-06.

Thorne, M. S., Lay, T., Garnero, E.J., Jahnke, G., & Igel, H., 2007. Seismic imaging of the laterally varying D" region beneath the Cocos Plate, *Geophys. J. Int.*, **170**(7), 635-648.

Thorne, M. S., Meyers, S. C., Harris, D. B. & Rodgers, 2008. A. J. Finite difference simulation of seismic scattering in random media generated with the Karhunen-Loève Transform, *Bull. Seism. Soc. Am.*, in prep.

Thorne, M. S., Garnero, E. J., McNamara, A., K., Jahnke, G., & Igel, H. Broadband SPdKS waveforms reveal ridge-like ULVZ structure in the lowermost mantle beneath the central Pacific, submitted to *Eos Trans. AGU*, 2008.

Toyokuni, G., Takenaka, H., Wang, Y., & Kennett, B. L. N., 2005. Quasi-spherical approach for seismic wave modeling in a 2-D slice of a global earth model with lateral heterogeneity, *Geophys. Res. Lett.,* **32**.

van der Hilst, R. D. & Kárason, H., 1999. Compositional Heterogeneity in the Bottom 1000 Kilometers of Earth's Mantle: Toward a Hybrid Convection Model, *Science*, **283**, 1885-1888.

Virieux, J., 1984. SH-wave propagation in heterogeneous media: Velocity-stress finite-difference method, *Geophys.,* **49**, 1933-1942.

Virieux, J., 1986. P-SV wave propagation in heterogeneous media: velocity-stress finite-difference method, *Geophys*., **51**, 889-901.

Wagner, G. S., 1996. Numerical Simulations of Wave Propagation in Heterogeneous Wave Guides with Implications for Regional Wave Propagation and the Nature of Lithospheric Heterogeneity, *Bull. Seism. Soc. Am.*, **86** (4), 1200-1206.

Wu, R.-S., 1982. Attenuation of Short-period Seismic Waves due to Scattering, *Geophys. Res. Lett.*, **9**, 9-12.

Wu, J., Hole, J. A., Snoke, J. A. & M. G. Imhof, 2008. Depth extent of the fault-zone seismic waveguide: effects of increasing velocity with depth, *Geophys. J. Int.*, **173** (2) , 611–622.

Yomogida, K., & Benites, R., 1996. Coda Q as a Combination of Scattering and Intrinsic Attenuation: Numerical Simulations with the Boundary Integral Method, *Pure and Applied Geophysics,* **148**, 255-268.

Appendix

A.1 Source code overview

The three parallel finite difference codes developed in this thesis *Fault3D*, *SHaxi* and *PSVaxi* are included on the supplementary CD ROM discussed below and are also publicly available at the home page of the *Seismic wave Propagation and Imaging in Complex media: a European network* Research Training Network (SPICE, *www.spice-rtn.org*, Igel, 2004). The SPICE software library provides open-source codes in computational seismology, training material on the numerical methods employed, benchmark solutions for forward and inverse problems, and publications of the SPICE team (Gallovič, 2007). After the 4-year SPICE project officially has ended in January 2008 the software library is now maintained by the Geophysics section of the LMU Munich.

Essential requirements for compilation and usage of all provided codes are (1) a *Fortran90* compiler and (2) an implementation of the *Message Passing Interface* (MPI) Library, such as the free MPICH distribution. The codes are tested on Unix systems only. Adaption to other operating systems should require minor modifications of the source codes. A detailed documentation is part of each package.
In the following, a short description of the content of the CD and the properties of the developed codes is given, in order to show the potential application areas.

A.2 Supplementary CD ROM

The supplementary CD contains three folders and one text document:

- Fault3D: Sources, setups and tools of the *Fault3D* program for full 3D seismic modelling of local geometries

- SHaxi: Sources, setups and tools of the *SHaxi* program for modelling global SH-wave propagation in the mantle

- PSVaxi: Sources, setups and tools of the PSVaxi program for modelling global P-SV wave propagation through the whole Earth

- Thesis.pdf: This thesis in Portable Document Format (PDF)

A.2.1 Fault3D

The Fault3D code was primary developed for modelling full 3D wave propagation including trapped waves in a various different fault zone structures with a low velocity channels. It is principally capable for modelling local 3D wave propagation in arbitrary structures and model sizes in the order of tenths of kilometers and frequencies around 10 Hz, depending on the computational resources.

A special focus during the code development was set on the implementation of a simple procedure for the model definition, especially for models which are invariant in one horizontal direction such as linear fault zone structures. Such models represent most of the investigated models in chapter 2. In addition, arbitrary 3D models can be set up, such as the split-fault model (Section 2.5.8) or the model with small scale inhomogeneities (Section 2.5.4), although this efforts to separately create a 3D dataset of the seismic parameters first, which is read by the Fault3D code at the beginning of a simulation.

The Fault3D code is expected to be useful for local studies on 3D structures and 3D wave field effects which need to add specific functionality to an existing verified MPI-parallelized code with a straightforward and compact source.

A.2.1.1 Fault3D directory structure

The Fault3D folder on the CD contains the following files and folders:

`Docs/`	`Documentation and user guide`
`Source/`	`Fortran90 sources of the Fault3D program`
`MODELS/`	`Input model files`
`RECEIVERS/`	`Input receiver files`
`Tools/`	`Tools and scripts for data processing`
`Par_hom2d`	`Example parameter file for “2D” model`
`Par_hom3d`	`Example parameter file for 3D model`
`Out_hom2d`	`Redirected stdout messages of hom_2d run`
`Out_hom3d`	`Redirected stdout messages of hom_3d run`
`DATA_hom2d/`	`Output folder of hom_2d run`
`DATA_hom3d/`	`Output folder of hom_2d run`

A.2.1.2 Table of Contents of the Fault3D User Guide

Introduction 3

1 How to perform a Fault3D Run 3

    1.1 Adjustment and recompilation of the Fault3D 3
    1.1.1 Changing the grid size 4
    1.1.2 Setting the number of nodes 4
    1.1.3 Compiling the code 5
    1.2 Customize a model setup 5
    1.2.1 The Parameter file 5
    1.2.2 The dom file 9
    1.2.3 The cdom file 10
    1.2.4 The cdom2vec command 11
    1.2.5 The propfile 11
    1.2.6 The receiver file 12
    1.3 Full 3D models 12

2 The output files 12

3 Changing hard wired limitations 13

4 Starting the program 13

    4.1 Interactive use 13
    4.2 Batch queues 14

5 Tools directory 15

    5.1 cdom2vec.x 15
    5.2 create3d_fz.m 15
    5.3 mpisnaps.m 15

6 References 15

A.2.2 SHaxi

The SHaxi code is developed for calculating global elastic SH body wave seismograms with realistic periods down to a few seconds. Due to the restriction to axi-symmetric models the needed resources are comparatively low, but topography or scattering effects of the great circle path between source and receiver can not be modeled. Calculations with periods in the order of 10-20 seconds can be performed on medium sized PC clusters, whereas periods below 5 seconds currently require a high performance parallel supercomputing system. The code can be run using an arbitrary number of nodes, each processing a vertical slice of the mantle which ranges from the surface down to the CMB. Further optimization of the needed resources in terms of memory and processing time can be performed by a lateral and radial reduction of the model size with respect to the maximum distance and depth of interest. Such reduced models require an additional tapering at the lower and far distance model boundaries to avoid artificial reflections. Several existing global models can be read by SHaxi and it is relatively simple to read own models. The implemented ring-source is well understood and an explicit formula for the radiated wave field is given.

A.2.2.1 Shaxi directory structure

The SHaxi directory on the CD consists of these files and folders:

`Docs/`	`Documentation and users guide`
`Source/`	`Fortran90 sources of the SHaxi program`
`RECEIVERS/`	`Input receiver files`
`Tools/`	`Tools and scripts for data processing`
`OUTPUT/`	`Output folder for example setup`
`Par_Debug`	`Parameter file of an example setup`
`Par_Files/`	`Collection of parameter files`

A.2.2.2 Table of Contents of the SHaxi User Guide

1 Introduction 4
2 Getting Started 5
    2.1 Where to download SHaxi 5
    2.2 Supported systems 5
    2.3 Software requirements 6
    2.4 Unpacking the source 6
    2.5 Compiling 6
    2.5.1 Adjusting the Makefile 7
    2.5.2 Compiling the code 7
    2.5.3 Interactive testing 8
    2.5.4 Batch jobs / NQS 8

3 Input Files 9
    3.1 The Parameter file 9
    3.2 Receiver files 13
4 The Grid 14
    4.1 Geometry of the SHaxi grid 14
    4.2 Changing the grid size 15
    4.3 Tables 17
5 Output Files 19
    5.1 Info file 19
    5.2 Par-out file 19
    5.3 Stdout files 20
    5.4 Seismogram files 20
    5.4.1 ASCII seismograms 20
    5.4.2 SAC seismograms 21
    5.5 Snapshot Files 22
    5.6 netCDF Model Files 23
6. Benchmarks 25
7. Models 27
    7.1 Models included in SHaxi release 27
    7.1.1 Homogeneous Earth Model 27
    7.1.2 PREM 1-D reference model 28
    7.1.3 Crustal thickening 28
    7.1.4 Basic Slab Structure 29
    7.1.5 Basic Rift Structure 30
    7.1.6 Cross section through tomography model TXBW 31
    7.2 Constructing User Defined Models 33
    7.2.1 Model Parameters 34
    7.2.3 Specifying the velocity anomaly 38
    7.2.4 Incorporating the model into SHaxi 39
    7.2.5 Adding the user module to the makefile 40
    7.2.6 Visualizing SHaxi models 41
8. Additional Tools 44
    8.1 Processing Seismograms 44
    8.2 Producing snapshots of wave propagation 44
9. File Structure 46
10 References 47
    10.1 SHaxi References 47
    10.2 General References 47
    10.3 Contact 48

A.2.3 PSVaxi

The PSVaxi code performs the calculation of high frequency global elastic P-SV seismograms including the complete set of teleseismic P-SV phases. Full earth models including the mantle and the outer and inner core, as well as models with limited distance range and depth extension can be defined for optionally minimizing the needed memory and processing time for a given setup.

The computational resources of PSVaxi are slightly higher than those of SHaxi due to the higher number of elastic parameters to be calculated and the larger model region to be stored in the PSV case but are of the same order. Dominant periods of 2-3 seconds were achieved using part the the 5TFlop/s “Iceberg” system (see chapter 4). For instance, the current 62 TFlop/s SGI Altix system of the Leibniz Rechenzentrum Munich has already enough performance to easily calculate complete global PSVaxi seismograms with a dominant period of 1 second.

The code can be run on up to 64 nodes where the total number of nodes must be a power of two (e.g. 2,4,8,…). This restriction can be bypassed for testing purposes, e.g. for testing a long period version of a simulation setup on a local network which consists of less machines than the total number of nodes of the planned simulation (e.g. a local network consisting of 4 PCs versus a planned simulation using 64 nodes): In this case the MPI environment can be configured so that multiple virtual nodes are defined on each single physical machine (for this example, 16 virtual nodes per PC) which communicate via the MPI library the same way as physically independent nodes would do. Of course the virtual nodes share the actual memory and processor time, and the requirements of the simulation to be tested must be downsized adequately.

A.2.3.1 PSVaxi directory structure

The PSVaxi directory on the CD contains the following files and folders:

`Docs/`	`Documentation and users guide`
`Source/`	`Fortran90 sources of the SHaxi program`
`RECEIVERS/`	`Input receiver files`
`OUTPUT/`	`Output folder for example setup`
`Runs/`	`Collection of parameter files`
`Par_Test`	`Parameter file of an example setup`

A.2.3.2 Table of Contents of the PSVaxi User Guide

Introduction 3
2 Getting Started 4
    2.2 Installation 4
    2.2.1 Unpacking the source 4
    2.2.2 File structure 5
    2.2.3 Configuring the Makefile 5
    2.2.4 Compiling 6
    2.3 Starting PSVaxi 6
    2.3.1 Serial environment 6
    2.3.2 Parallel MPI environment 7
3 Input files 7
    3.1 Parameter file 7
    3.1.1 Example file 8
    3.1.2 Description of the example file 9
    3.2 Receiver file 14
4 Output files 14
    4.1 List of output files 15
    4.2 Explanation of the output files 15
    4.3 Snapshot files 17
5 Tools 18
    5.1 showseis.m 18
    5.2 showbin.m 18
6 References 18

Curriculum Vitae

Persönliche Daten

Name	Gunnar Jahnke
Geburtsdatum	14. Mai 1971
Geburtsort	Flensburg
Familienstand	ledig

Schulbildung

1977 - 1981	Grundschule Witzenhausen-Gertenbach
1981 - 1987	Gesamtschule Witzenhausen
1987 - 1990	Grotefend Gymnasium Hann Münden
Mai 1990	Abitur

Zivildienst

1990 – 1991	Hann Münden

Studium und Beruf

1991 – 1998	Physikstudium an der Georg August Universität Göttingen
April 1994	Vordiplom im Fach Physik
2000-2001	Diplomarbeit zum Thema "Analyse schwacher teleseismischer Einsätze an kleinen Arrays: Möglichkeiten und Grenzen" am Institut für Geophysik, Göttingen, bei Prof. Dr. Michael Weber
Juni 1998	Diplom im Fach Physik
1999 – 2003	Doktorand am Department für Geo- und Umweltwissenschaften der Ludwig-Maximilian-Universität München bei Prof. Dr. Heiner Igel
seit Juni 2003	Wissenschaftlicher Angestellter im Bereich Seismologie der Bundesanstalt für Geowissenschaften und Rohstoffe, Hannover